CORROSION BEHAVIOR AND RESIDUAL STRESS OF MICROARC OXIDATION COATED AZ31 MAGNESIUM ALLOY FOR BIOMEDICAL APPLICATIONS

By

Yanhong Gu

RECOMMENDED: _____

_____

_____

_____

Advisory Committee Chair

_____

Chair, Department of Mechanical Engineering

APPROVED: _____

Dean, College of Engineering and Mines

_____

Dean of the Graduate School

_____

Date

CORROSION BEHAVIOR AND RESIDUAL STRESS OF MICROARC OXIDATION COATED AZ31 MAGNESIUM ALLOY FOR BIOMEDICAL APPLICATIONS

A

DISSERTATION

Presented to the Faculty

of the University of Alaska Fairbanks

in Partial Fulfillment of the Requirements

for the Degree of

DOCTORATE OF PHILOSOPHY

By

Yanhong Gu, Ph.D.

Fairbanks, Alaska

August 2012

Abstract

Mg alloys are potentially new biomaterials for bone repair or replacement. Appropriate coating is, however, needed to make the Mg alloy more resistant to corrosion. In this research, protective microarc oxidation (MAO) coatings were produced on AZ31 Mg alloys in sodium phosphate electrolyte. The coatings were produced under varying pulse frequency, applied voltage, oxidation time and electrolyte concentrations. This research analyzed the effects of the above four MAO process control parameters on the residual stresses and the corrosion behavior. Optimization of the MAO control parameters would allow production of AZ31 Mg alloy with high corrosion resistance.

It is well accepted that residual stress and corrosion behavior are two significant factors in the development of AZ31Mg alloys. The residual stresses in the MAO coatings were evaluated by the X-ray diffraction (XRD)-$\sin^2\psi$ method. A predictive model of the residual stresses is proposed and a principal components analysis (PCA) was conducted to determine the contribution of the MAO control parameter on the residual stresses.

Long-term corrosion behavior of MAO-coated Mg alloys was evaluated by the potentiodynamic polarization and electrochemical impedance spectroscopy (EIS) tests. The porosity of the samples after various immersion durations was evaluated by the potentiodynamic polarization method. The pre- and post- corrosion microstructures and the phase composition of MAO-coated samples were studied. Post-corrosion phase identification showed that hydroxyapatite (HA) was formed on the surface of the samples. The ratio of Ca/P in HA was determined by the X-Ray Fluorescence

(XRF) technique.

The degradation of the MAO-coated AZ31 alloys is reduced due to the MAO coating and the formation of a corrosion product layer. A predictive model of the corrosion current density is proposed and a PCA was conducted to determine the contributions of the individual MAO control parameter on the corrosion rate. The corrosion process and mechanism of MAO-coated AZ31 alloys in SBF were modeled based on the electrochemical corrosion results and the pre- and post-corrosion surface analysis.

It is believed that under optimized control parameters, the MAO-coated AZ31 Mg alloy is superior implant material for biomedical applications.

Table of Contents

List of Figures

Page

List of Tables

Page

List of Equations

Page

List of Appendices

Page

Acknowledgements

I would like to express my deepest gratitude to my Graduate Advisory Committee Chair, Dr. Sukumar Bandopadhyay, for his excellent guidance, advice, caring, and financial support. I appreciate his patience in reviewing and editing my thesis. I also thank my co-advisor Dr. Cheng-fu Chen, Dr. Ken Severin and Dr. Sunwoo Kim for serving on the committee. I am also grateful to Dr. Jing Zhang for guiding the early part of the research and providing me with the background in biomaterial and corrosion science.

I acknowledge the Graduate School for the financial support for this project.

I would like to thank Dr. Ken Severin, Dr. Tom Trainor for allowing me to use the scanning electron microscope, X-ray fluorescence and the X-ray diffractometer. I also acknowledge Eric Johansen for the use of the machine shop equipment. I also thank Water and Environmental Research Center for supplying the deionized water.

I would like to thank Prof. Ning Chengyun (South China University of Technology) and his students Wenming Xiong and Yuanjun Guo for supplying the samples for this research.

Thanks to my all good friends, Lily Yongjun Zhang, Michael Golub, Liangbiao Chen, Zhipeng Dai and Daisy Huang, for their help and suggestions.

Finally I would like to thank my husband, Ling Wu, for his support and encouragements.

Chapter 1: Introduction

1.1 Scientific Rationale

Metallic materials such as stainless steels, cobalt-based alloys and titanium alloys are commonly used to assist in repairing or replacing damaged bone tissues. These materials are more suitable for load-bearing applications as compared to the ceramics or polymeric materials. This is due to their high mechanical strength and fracture toughness [1, 2]. A limitation of the metallic biomaterials currently in use is the possible release of toxic metal ions through the corrosion or wear processes [3-7] leading to inflammation and tissue losses [3, 5-14]. Major drawback of the metallic biomaterials such as Ti alloy, Co-Cr alloy and stainless steel lies in the mismatch of mechanical properties between these implant materials and natural bone, especially in the elastic modulus (Table 1.1), results in implants following stress shielding of the bone. The effects of stress shielding lead to reduced stimulation of new bone growth [15]. The metallic biomaterials currently in use are essentially neutral in vivo, and can remain as permanent fixtures. In the case of plates, screws and pins used to secure serious fractures (Figure 1.1), however, they must be removed in another surgical procedure after the damaged tissue heals [16] . Repeated surgeries adversely increase both the health costs and the morbidity rate of a patient.

Degradable implants are designed to corrode away while or after they complete their tasks in the body. This degradation makes the second surgery unnecessary. Avoidance of a second surgery is not only preferable and reduces cost, but also lowers the risk of complications which are generally associated with a surgery. Degradable implants could also be designed to have a degradation rate that is compatible to the healing rate.

Mg and Mg alloys can be gradually dissolved and then excreted by the human body, and thus may be used as temporary implants. The density, elastic modulus and the compressive yield strength of magnesium are relatively closer to those of the natural bone than is the case for other commonly used metallic implants (Table 1.1). Moreover, magnesium is essential to human metabolism and exists naturally in the bone tissue [17-22]. It is the fourth most abundant cation in the human body, with approximately one-half of the total physiological magnesium stored in the bone tissue [19].

Since Mg and Mg alloys are biodegradable and biocompatible, they become attractive materials for temporary implants. Mg and Mg alloys could therefore, replace existing implant materials, facilitate healing, and reduce the health costs.[1, 23-26]

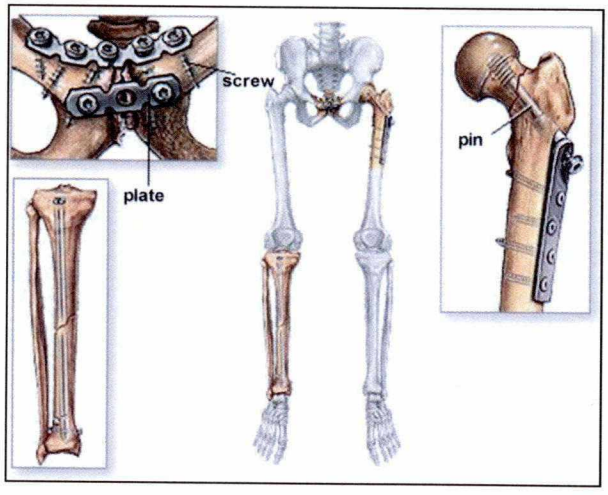

Figure 1.1 Example of plates, screws and pins as "permanent" fixtures

Table 1.1 Summary of the physical and mechanical properties of various implant materials in comparison to natural bone.

Properties	Natural bone	Mg alloy	Ti alloy	Co–Cr alloy	Stainless steel	Synthetic hydroxyapatite
Density (g/cm^3)	1.8–2.1	1.74–2.0	4.4–4.5	8.3–9.2	7.9–8.1	3.1
Elastic modulus (GPa)	3–20	41–45	110–117	230	189–205	73–117
Compressive yield strength (MPa)	130–180	65–100	758–1117	450–1000	170–310	600
Fracture toughness ($MPa\text{-}m^{1/2}$)	3–6	15–40	55–115	N/A	50–200	0.7

1.2 Review of Literature

1.2.1 Common Biomedical Magnesium Alloys

In the past, various types of magnesium alloys as well as pure magnesium have been proposed for biomedical applications. Many in-vitro studies have been performed to understand their degradation rate and corrosion mechanism. The compositions and the phase constituents of several representative alloys are summarized in Table 1.2. Among them, the AZ91D and AZ31 are typical examples of Mg–Al–Zn alloys. It has been stated that, when compared with pure magnesium, the introduction of Al can not only modify the mechanical properties, but also enhance the corrosion resistance [27]. It has been also demonstrated [28] that, in the Mg–Zn–Al system, the corrosion resistance of the alloys in the simulated body fluids (SBF) drops with increased Al content. A high Al concentration increases the content of $Mg_{17}Al_{12}$ phase. $Mg_{17}Al_{12}$ generally precipitates at the grain boundaries, which in turn enhances the tendency for pitting corrosion. The typical concentration of Al in human blood serum is ~2.1–4.8μg / L [27]. Higher Al concentration is harmful to neurons and the osteoblasts [29].

Hence, the amount of Al released from Mg alloys must be carefully controlled. In comparison with other magnesium alloys, the AZ31 magnesium alloy, with low Al content, is considered to be most suitable as a biodegradable material.

Table 1.2 Common biomedical magnesium alloys.

Family	Representative alloys	Alloying elements (wt.%)			Main phases
Pure Mg	Mg [30]				Mg;
Mg-Al-Zn	AZ31 [30, 31]	3Al	1Zn		Mg; $Mg_{17}Al_{12}$
	AZ91 [30, 32]	9Al	1Zn		
Mg-Ca	Mg-xCa[30, 33, 34] (x = 1,2,3,4,5,…)	xCa			Mg; Mg_2Ca
Mg-Zn-Ca	Mg-1Zn-1Ca [35]	1Zn	1Ca		Mg; Mg_2Ca; $Ca_2Mg_6Zn_3$
Mg-Zn-Mn-Ca	Mg-2.0Zn-1.2Mn-1Ca [36]	2 Zn	1.2Mn	1Ca	Mg; Mg_2Ca; $Ca_2Mg_6Zn_3$; $Ca_2Mg_5Zn_{13}$
Mg-Si-Ca		1Si	1Ca		Mg; Mg_2Si; SiMgCa
Mg-Zn	Mg-xZn[29, 30, 32, 37] (x = 1,3 10)	xZn			Mg; MgZn; Mg_2Zn_3; Mg_7Zn_3
Mg-Zn-Mn	Mg-1Mn-1Zn[38]	1Mn	1Zn		Mg; MgZn; Mg_2Zn_3; Mg_7Zn_3
Mg-Mn	Mg-1Mn [30]	1Mn			Mg; Mn
RE containing magnesium alloy	LAE442[31, 39]	4Li	4Al	2RE	Mg; $Al_{11}RE_3$
	WE43 [39]	4Y	3RE		Mg; $Mg_{12}YNd$; $Mg_{14}YNd_2$
	ZE41[30, 32]	4Zn	1RE		Mg; MgZn(RE)
	AE44 [30]	4Al	4RE		Mg; $Mg_{17}Al_{12}$; $Al_{11}RE_3$; $Al_{12}RE$
	Mg-xGd [40] (x = 5, 10, 15, . . .)	xGd			Mg; Mg_5Cd
	WZ21 [41]	2Y	1Zn		Mg; $MgYZn_3$; Mg_7Zn_3; Mg_3YZn_6
	Mg-8Y [42]	8Y			Mg; $Mg_{24}Y_5$; Mg_2Y

1.2.2 Approaches to Improve Mg Degradation

The degradable properties of Mg and its alloys are, however, a double-edged sword. Mg is a highly reactive metal, and corrosion rates when immersed in physiological solutions are high. The lifespan of Mg alloys in human body usually is 12-18 weeks [1]. This constraint adversely restricts any practical application of the Mg alloys as a suitable implant material [43]. In order for the use of this material to be feasible for orthopedic applications, the corrosion mechanisms must be reduced and controlled. In response to this, various possibilities exist to develop magnesium alloy by using alloying elements and protective coatings that would reduce corrosion rates. The processes, of course must lead to a non-toxic, and biologically compatible material.

As alloying of Mg is challenging due to low solubility of many elements in Mg, the development of coatings on Mg alloys are of high significance, and could be an attractive approach to improve the corrosion resistance. Coatings can protect a substrate by providing a barrier between the metal and the corrosion inhibiting chemicals. In order for a coating to provide adequate corrosion protection, it must be uniform and well adhered. One of the challenges with magnesium is its chemical reactivity. When it is in contact with air or water, an oxide or hydroxide layer is formed on the surface which can have a detrimental effect on the coating adhesion and uniformity.

Challenges for surface modification of Mg alloys to reduce the degradation and to increase the biological performance are complicated. The implant in a human body is expected to degrade in a relatively short time-frame, as compared to other non-medical applications. In those cases, defect-free and robust coatings for a long-term

corrosion protection are not of any concern. In an effort to improve the corrosion resistance of the magnesium alloys, various conventional preparation methods such as anodic oxidation [44, 45], polymer coating [46], chemical conversion coatings[47], plasma iodization [48], and magnetron sputtering processes [49] have been proposed. None of these methods produce satisfactory coatings, and only provides a low corrosion resistance.

Microarc oxidation (MAO) technique, also known as the plasma electrolytic oxidation (PEO) method, is a kind of anodizing treatment. Since 1990's a significant amount of research has been conducted on MAO since it could enhance the corrosion and the wear resistance by forming a remarkably thick, dense and hard film on the surface of the mg alloys [50, 51]. The MAO is an ecofriendly method and can be processed easily to make high-quality oxide coatings on the surfaces of light metals such as Ti, Al, Mg and their alloys [52]. Therefore, it has become a viable alternative for the pre-existing anodizing process. In addition to those superior physical and chemical properties of Mg alloys, MAO process can uniformly form an oxide film which strongly adheres to a substrate with complex geometries [53, 54]. MAO coatings also offer several additional advantages over other coatings. For example, MAO coatings provide high hardness and can be used at high temperatures. These coatings are, however, porous, and require proper selection of the electrolytic solutions and appropriate voltage to develop good coatings. Based on the literature reviewed, it seems, the MAO technique is a reasonably promising and effective method for surface treatment of magnesium alloys.

Although the MAO process is very effective for surface modification, residual stress

develops due to the temperature and microstructural changes during the coating process. The residual stresses have a significant influence on the coating quality, such as the corrosion resistance and fatigue properties [55]. Therefore, understanding and control of the residual stress in the MAO coating process is a key to improve the mechanical properties of the Mg alloys.

1.2.3 Corrosive Environment of the Body Fluids

From a chemical point of view, the corrosive environment of the body fluid consists of a 0.9% NaCl solution with small amounts of other inorganic salts, such as Ca^{2+}, PO_4^{3-} and HCO^{3-} [56]. The chemical environment of blood fluid is highly corrosive for many metals and alloys, especially due to the presence of high concentration of chloride ions. Other ions present may also strongly contribute to the corrosion process, either as accelerators or inhibitors.

In some earlier studies, Mg corrosion experiments were carried out in simple NaCl solutions for biomedical applications (Table 1.3). To characterize mimic the body environment adequately, a simulated body fluid (SBF) was employed in the current study to understand the corrosion behavior of pure magnesium and magnesium alloys. Simulated body fluid is very useful in predicting in vivo bone bioactivity as observed by other researchers [57-59].

Table 1.3 Collection of various published data concerning electrochemical characterization of MAO-coated Mg and Mg alloys.

Material	Electrolyte	Immersion time	Electrochemical tests	Ref.
pure Mg	SBF	48h	Tafel	[60]
pure Mg, AZ31, AZ61 and AZ91D	Modified SBF	24 days	EIS	[28]
AZ91	SBF	35h	Tafel and EIS	[61]
AZ91,AZ91Ca, AZ61Ca	Modified SBF		Tafel and EIS	[62]
AZ91D	Modified SBF	5 days	EIS	[63]
Mg–Mn–Zn alloy	SBF	12days	Tafel	[38]
AZ31	SBF	72h	Tafel and EIS	[58]
AZ31	SBF	7 days	Tafel and EIS	[64]
AZ31	0.1M NaCl solution	72h	Tafel	[65]
MAO pure Mg	SBF	40min	Tafel	[66]
MAO AZ91	SBF	5 min	Tafel	[67]
MAO AZ91	SBF	312 h	Tafel	[68]
MAO AZ91D	3.5% NaCl solution	288 h	EIS	[69]
MAO AZ91	5 % NaCl solution	120 h	Tafel and EIS	[70]
MAO AM50	0.1M NaCl solution	50 h	Tafel and EIS	[71]
MAO AZ31	3.5% NaCl solution	30 min	Tafel and EIS	[72]
MAO AZ31	0.1M NaCl solution	1000 h	EIS	[73]

1.2.4 Problem Statements

From the preceding discussions, it may be clear that there is a need to examine the corrosion behavior of the MAO-coated AZ31 alloy in SBF, as well as the residual stress developed in the coatings on Mg alloy due to the MAO process. The processing conditions of MAO, such as the pulse frequencies, applied voltages, oxidation time, and the electrolyte concentrations, are some of the major factors which determine the quality of the coatings in terms of corrosion resistance and residual stress. As of this date, the researchers have only focused on the influence of one of the control parameters on residual stress and the corrosion behavior of the MAO-coated Mg alloys. In addition, the corrosion behavior of MAO-coated Mg alloys when immersed

for a shorter duration in the SBF has been investigated [74, 75]. The long-term corrosion behavior and prediction of the degradation mechanism of the MAO-coated Mg implants in the human body are extremely important. A systematic study of the effect of MAO control parameters on the residual stress in MAO-coated AZ31 Mg alloy, and the long-term corrosion behavior of MAO-coated AZ31 Mg alloy in the SBF is lacking.

1.3 Scope of the Research

The major focus of this research is to determine the residual stress of MAO-coated AZ31 Mg alloy and the corrosion behavior of MAO-coated AZ31 magnesium alloy in the SBF. One of the goals is to understand the effects of the MAO process on the residual stresses. A second goal is to optimize the control parameters that would produce a coating with higher resistance to corrosion. Biocompatibility is influenced by surface chemistry and topography of the implant material. While surface chemistry has played a dominant role and attracted much attention in the past decades, the surface topography has received very little attention. A clear understanding of the surface chemistry and topography (thickness of the coating and smoothness) could allow the design and synthesis of Mg alloys with high resistance to corrosion. The scope of this research is schematically shown in Figure 1.2. The research results would be valuable for the development of implants for biomedical applications.

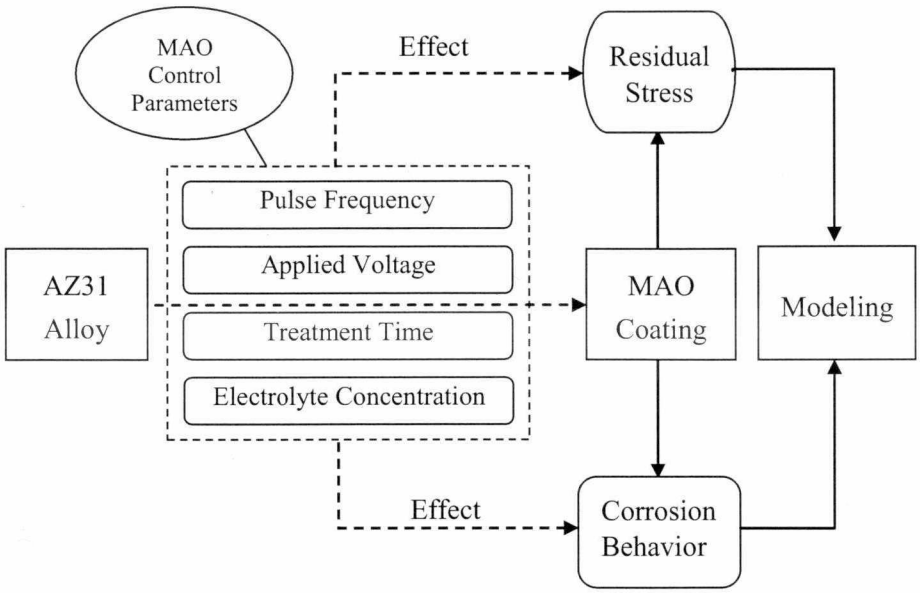

Figure 1.2 Schematic diagram of the scope of the study

The various tasks of this research include the following:

1) Preparation of MAO coatings under various control parameters.
2) Determination of the phases and element concentrations of the MAO coating that are formed at various conditions. Examination of the surface and cross-section morphologies as well as the porosity of the MAO coatings.
3) Evaluation and simulation of residual stresses in the MAO-coated samples.
4) Evaluation of the corrosion rate and the electrochemical impedance, as well as the characteristics of the MAO coatings.
5) Selection of the optimum parameter for the MAO process.
6) Predictive model for the corrosion rate of the MAO-coated AZ31 alloy in the SBF.
7) Understanding of the corrosion mechanism to suggest an appropriate model for the corrosion phenomena.

Chapter 2: Preparation and Characterization of MAO Coatings

2.1 Principle of MAO Deposition Process

Microarc oxidation (MAO) is an electrochemical surface treatment process for generating oxide coatings on metals such as aluminum, magnesium and titanium. It has been an effective surface treatment technology for over a decade. Similar to anodizing but employing higher potentials, the resulting plasma in the MAO is able to modify the structure of the oxide layer. The coating is a chemical conversion of the substrate metal into its oxides, and grows both inwards and outwards from the original metal surface. Since it is a conversion coating, rather than a deposited coating, it has excellent adhesion to the substrate metal.

According to Belevantsev [76], there are three stages in the MAO process: (1) anodizing; (2) sparking; and (3) MAO. Stages (1) and (2) take from several seconds to minutes, depending on the alloy composition and the reactivity of the electrolyte used. The last stage, the MAO, is responsible for the growth of the ceramic coating and thus plays the major role in the oxidation process.

The MAO coating system is shown in Figure 2.1. The power supply is an adjustable pulse AC, voltage ranges from 100 to 800 V, is applied to the bath. An electrolyte prepared from Na_3PO_4 solution in distilled water is kept at room temperature during the entire treatment process. The MAO is performed in a stainless steel bath equipped with a water-cooling system. It uses a metallic member immersed in the electrolyte as the anode; the bath container serves as the cathode.

When metals or alloys are immersed in an electrolyte, the metal surfaces interact with

the electrolyte solution. As a result, the metal surface immediately generates a very thin insulating layer of the oxide film, and then a complete layer of insulating film is formed. When the voltage applied to the metal exceeds a critical value, a large amount of surface sparks is generated. The arc discharge strengthens and activates the reaction occurring at the anode. The oxide film breakdown always occurs in a relatively weak state, resulting in the formation of many surface discharge channels (pores). The plasma discharge in the channel can reach a high temperature and pressure in a relatively very short time, less than 10 seconds. Therefore, the alloying elements diffuse into the channel by melting and oxidation, resulting in the formation of a new oxide film. The diffusion transfers to other parts of the relatively weak section of the metal, and ultimately a uniform oxide film is formed on the metal.

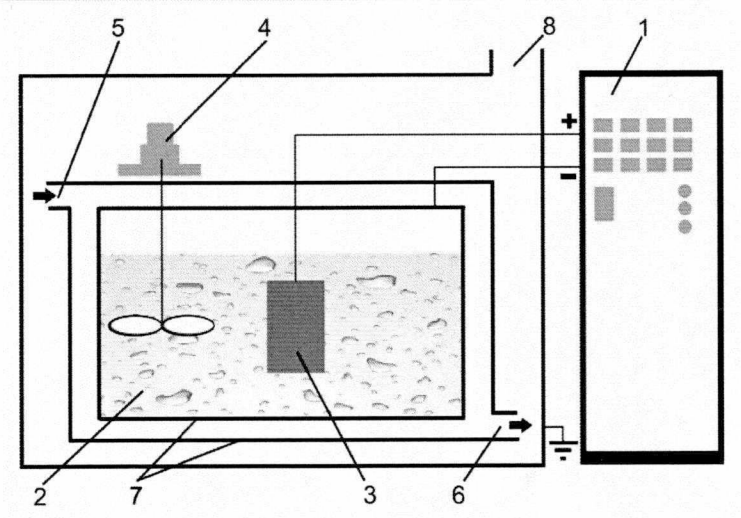

Figure 2.1 Schematic diagram of MAO system. 1. Power supply and control system; 2. Electrolyte; 3. Sample; 4. Stirrer; 5. Cooling water inlet; 6. Cooling water outlet; 7. Stainless-steel bath; 8. Exhaust fan.

2.2 MAO Coating Preparation

The material used in this research is AZ31 magnesium alloy. The chemical composition of the alloy is listed in Table 2.1. Samples with dimension of 20mm × 10mm × 1 mm were used as the substrates. Prior to the MAO treatment, the samples were polished with various grades SiC abrasive papers. After polishing, the samples were degreased ultrasonically in a metal cleaning agent for 2 min, rinsed in deionized water for 1 min, dehydrated in ethyl alcohol for 2 min. and then immediately dried in warm air.

Table 2.1 Chemical composition of AZ31 magnesium alloy.

Elements	Al	Zn	Mn	Si	Cu	Mg
Content (wt.%)	2.5~3.5	0.7~1.3	0.2~1.0	0.05	0.01	Balance

The MAO coating was processed in the MAO-20 equipment (Chengdu PULSETECH Electrical Co., China, shown in Figure 2.2), which has an adjustable DC pulse source up to 50 kW, a stainless steel container with a sample holder, a stirring and a cooling system. The substrates are used as anodes, while the walls of the stainless steel container serve as the cathodes in the electrolytic bath. Aqueous solution of sodium phosphate with various concentrations was used as the electrolyte. A pulsed current was then applied at various frequencies with the same duty cycle. Four groups of MAO coatings were produced on the AZ31 alloy under various processing conditions, shown in Table 2.2. The variation of current with oxidation time during the MAO process was recorded for Group 4 samples.

Figure 2.2 (a) MAO equipment; (b) Power system

Table 2.2 MAO process parameters of four groups of samples.

	Sample designation	Pulse frequency (Hz)	Applied voltage (V)	Oxidation time (min)	Electrolyte concentration (g/L)
Group 1	300Hz	300	325	5	30
	500Hz	500	325	5	30
	1000Hz	1000	325	5	30
	3000Hz	3000	325	5	30
Group 2	250V	3000	250	5	30
	300V	3000	300	5	30
	325V	3000	325	5	30
	350V	3000	350	5	30
Group 3	1min	3000	325	1	30
	3min	3000	325	3	30
	5min	3000	325	5	30
	8min	3000	325	8	30
Group 4	20g/L	3000	325	5	20
	30g/L	3000	325	5	30
	40g/L	3000	325	5	40

2.3 MAO Current density–time Curves

The variation of current density with the MAO time at various electrolyte concentrations is shown in Figure 2.3. It can be observed that the current density

decreases sharply and then gradually becomes stable. The MAO process can be divided into three distinct stages. In the first stage, as the rate of applied voltage changes rapidly, micro gas bubbles are produced on the surface of the samples. After 2–3 seconds, strong white sparks accumulate and the intensity of the gas bubbles increases. A large amount of heat due to chemical reaction escapes outwards and the current density decreases rapidly. The large drop of the current density is attributed to the rapid formation of the MAO coating which increases the resistance, thus hinders the flow of the electrons. In the second stage, the white sparks becomes sparse and the local coarse arcs are occasionally produced. In the third stage, only the fine micro arcs occur on the surface of the samples, therefore the reaction is steady without obvious changes in the current density. The current density increases with increasing electrolyte concentrations.

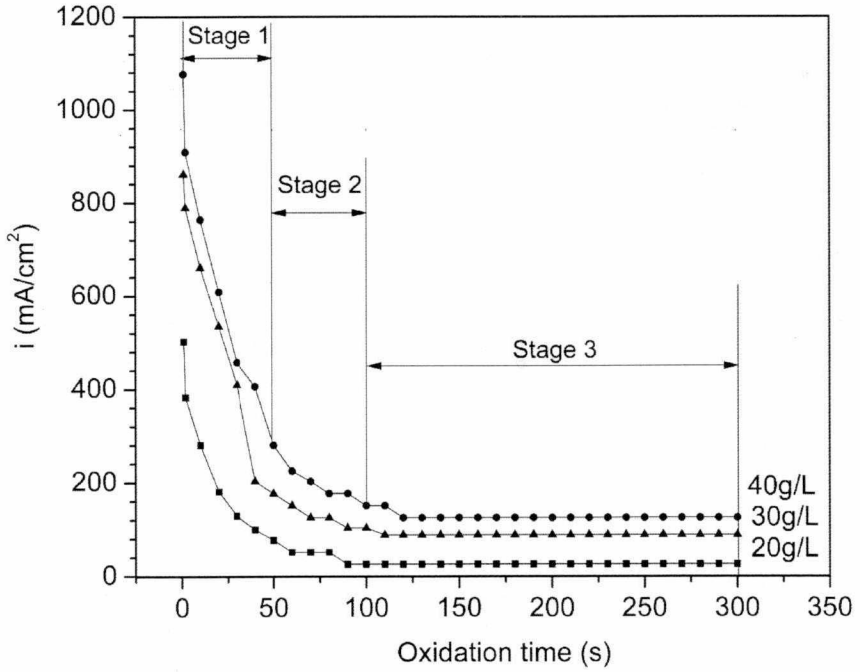

Figure 2.3 Variation of current density with oxidation time for MAO coatings produced at various electrolyte concentrations.

2.4 Characteristics of MAO Coatings

The surface characteristics of the MAO coating including the composition and the topography exert considerable influence on the biocompatibility.

Netherlands Quanta200 scanning electron microscope (SEM) was used to examine the surface and the cross-sectional morphologies of the MAO coatings. All the samples detected by the SEM were sputtered with a thin gold layer in order to prevent surface charging effects. X-ray diffraction (XRD) analysis was carried out using an X'Pert PRO. The samples were scanned using CuKα radiation under 45 kV voltage and 40 mA current at normal θ-2θ geometry with a range of 20° to 80° 2θ, and a step size of 0.025° with a glancing angle of 2.5°. PanAlytical Axios dispersive X-ray fluorescence (XRF) was employed for quantification element of the MAO coatings. The porosity of the MAO coating was calculated by the potentiodynamic polarization method.

2.4.1 Coating Morphology

Microstructures were used to determine the mechanical and the physical properties of MAO coatings. The effects of pulse frequency, applied voltage, electrolyte concentration and oxidation time on the morphologies are discussed in the following sections.

2.4.1.1 Effect of Pulse Frequency

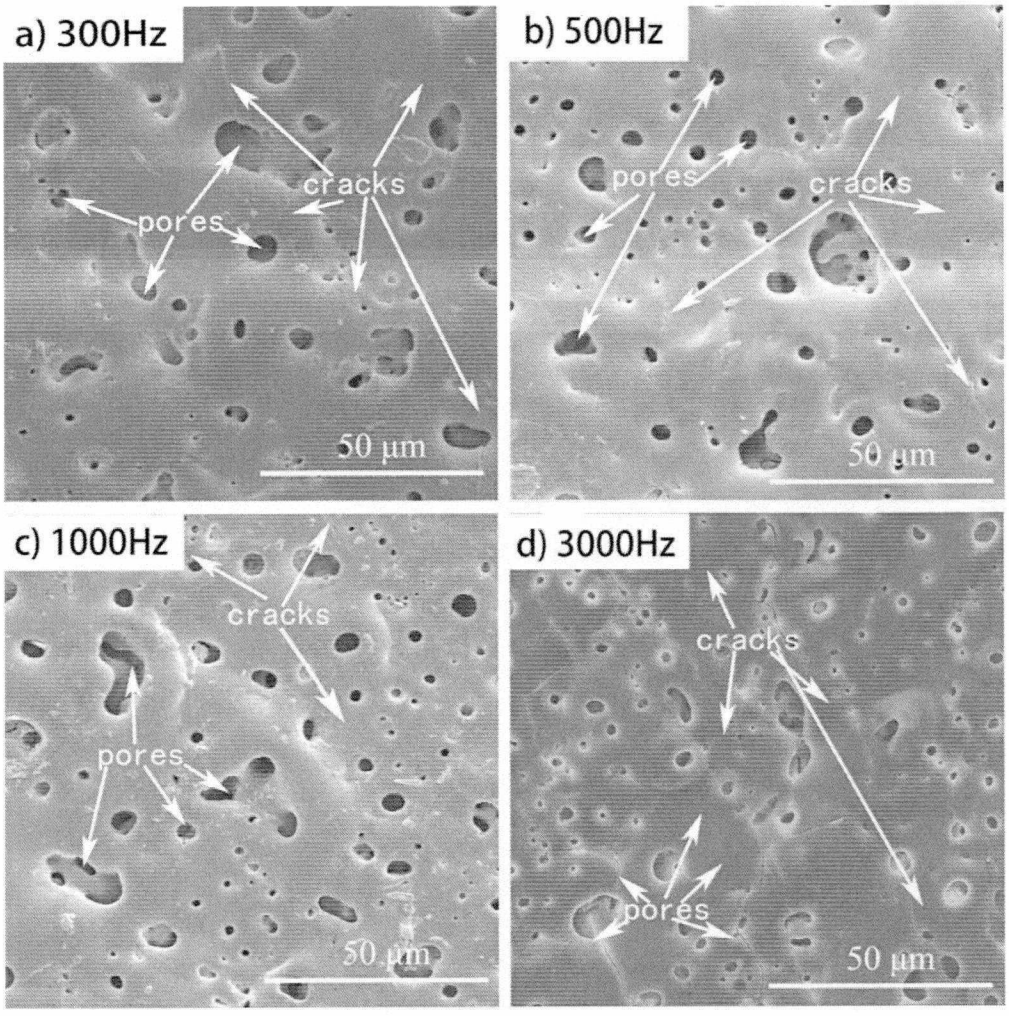

Figure 2.4 Surface morphology of MAO coatings produced at various pulse frequencies: (a) 300 Hz, (b) 500 Hz, (c) 1000 Hz and (d) 3000 Hz.

The effect of various pulse frequencies for MAO coating process on the surface morphology can be explained by the SEM images (Figure 2.4a ~ d). Micro pores and cracks can be observed on the coating surface for all the four frequencies tested, exhibiting different porosity at each individual frequency. During the MAO process, the pores and the cracks served as the microarc discharging channels through which

the oxide leaves the surface, and then experiences intensive oxygen evolution, which in part contributes to the development of the porous structure in the ceramic coatings. The number of pores on the surfaces of the coated specimen at 300 Hz, 500 Hz, and 1000 Hz is similar (Figure 2.4a ~ c), while for the 3000 Hz sample, the number of pores appears to be larger. The average pore size and the average crack size decreases with the increase in the pulse frequency. The samples produced at the 3000 Hz exhibit a more uniform surface morphology. The porosity values (in Section 2.3.2) verify the presence of a uniform surface morphology.

The differences in the extents of the micro cracks and the micro pores in the four coatings are attributed to the intensity of energy used in the MAO process [77]. Although all the four pulse frequencies were operated at the same pulse-time ratio, the 3000-Hz case only has a discrete pulse-on-time of 0.1 ms, as opposed to 0.3 ms (1000 Hz), 0.6 ms (500 Hz), or 1 ms (300 Hz). This indicates that the pulse frequency at 3000 Hz delivers the least intensity of energy and thus results in a coating with relatively smaller size micro pores and micro cracks. At 300 Hz, larger pores are produced (Figure 2.4a) due to the relatively prolonged pulse-on-time (1 ms). The pulse-on-time in this case is much longer than the lifetime (0.17 ms) of the spark [78]. In addition, at 300 Hz, the continuous discharge during the pulse-on-time leads to higher temperature in the coating layer. The stronger quenching effects induce micro cracks in the coatings [77].

2.4.1.2 Effect of Applied Voltage

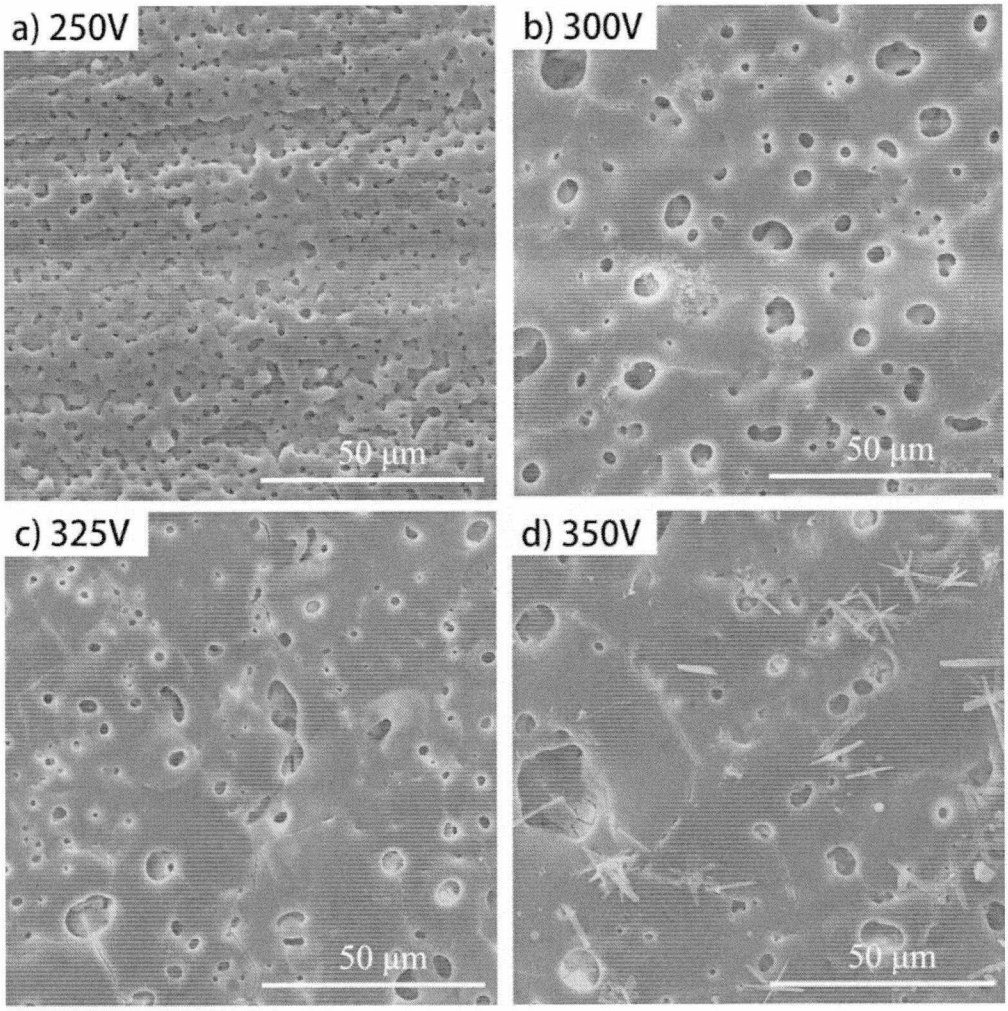

Figure 2.5 Surface morphology of MAO coatings produced at various applied voltages: (a) 250 V, (b) 300 V, (c) 325 V and (d) 350 V.

The SEM images shown In Figure 2.5 revealed typical porous surface morphologies for the coatings produced at various voltages. As can be seen in Figure 2.5a, at low voltage 250 V the oxidation coatings showed dense, crater-like microstructures with some round-shape shrinkage pores in the crater-centers. A well developed melt network was also produced at 250 V.

At medium voltage 300 V (Figure 2.5b), an increased size of pores can be observed. The large round or elliptical shaped pores imply the merging of the smaller pores. Additionally, many small cracks are evident in the coating.

At a voltage of 325 V (Figure 2.5c), the number of micropores appears to increase with a decrease in size of the pores. Elliptical shaped pores and small cracks are also apparent in the coating.

A loose grained, porous surface morphology with $MgAl_2O_4$ spinel crystals can be observed for the coatings produced at high voltage of 350 V. The size of the pores and the cracks are significantly larger than those produced at 300 V and 325 V. This suggests that the smaller pores are connected and as a result larger cracks are formed.

The sample produced at 325 V is more uniform, which can be confirmed by the porosity values presented in Section 2.4.2. The dense level of the MAO coatings depends on the porosity.

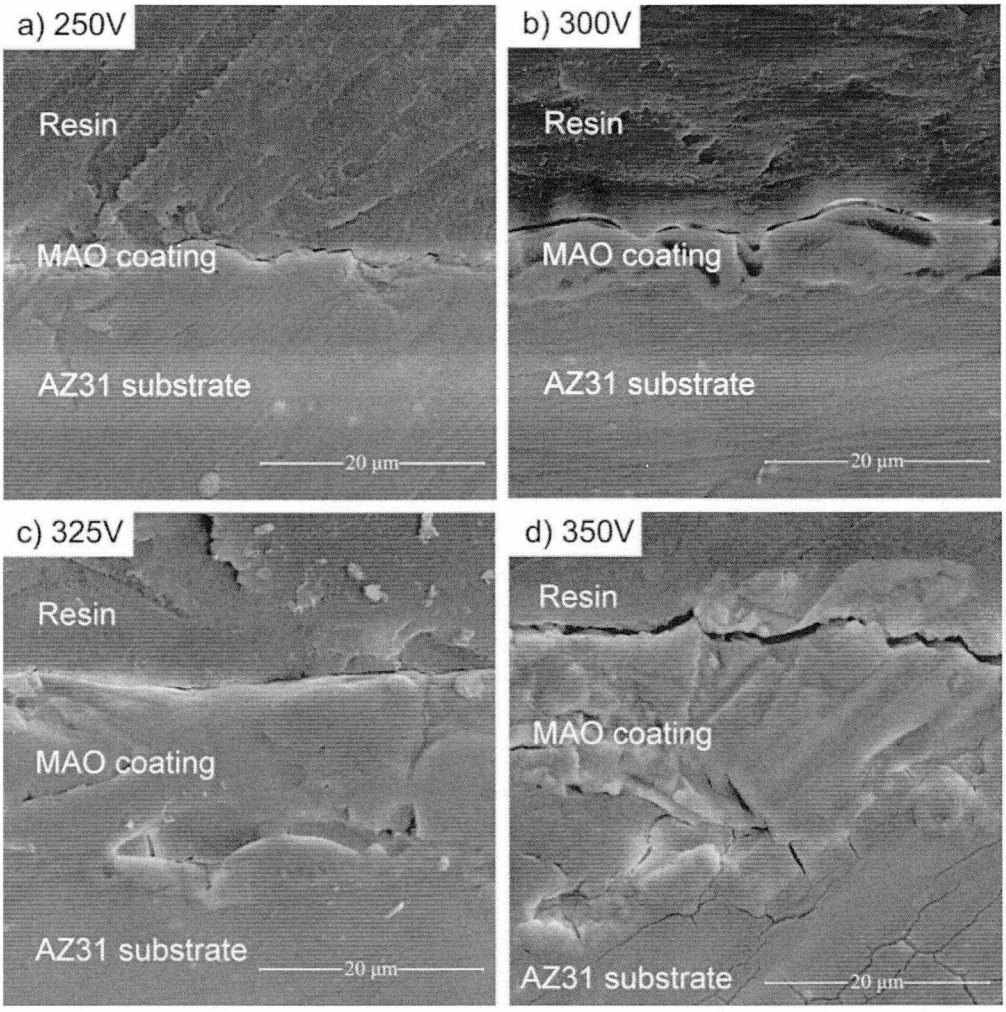

Figure 2.6 Cross-sectional morphology of MAO coatings produced at various applied voltages: (a) 250 V, (b) 300 V, (c) 325 V and (d) 350 V.

The cross-sectional images of the MAO coatings produced at various voltages are shown in Figure 2.6. The micro pores and the micro cracks can be observed in the MAO coating. These pores and the cracks do not penetrate the entire layer. The pores in the coating layer result from the gas bubbles moving out of the micro-arc discharge channels, while the cracks are formed by the thermal stress due to the rapid solidification of the molten oxide in a relatively cold electrolyte [51].

The smallest thickness that is seen in Figure 2.6a is at the lowest voltage (250 V), which has resulted in an undefined boundary between the substrate and the MAO coating. It can be noted that the thickness of the coating increases with increasing applied voltages (in the range of 5 μm to 20 μm from 250 V to 350 V). The sample coated at 325 V shows a relative uniform structure, compared to the other conditions (Figure 2.6c). For samples produced at 350 V, however, the coating is not that compact and tends to delaminate and crack inside the coating.

2.4.1.3 Effect of Oxidation Time

The surface morphologies of the MAO coatings produced at various oxidation times are shown in Figure 2.7. Typical porous microstructures can be observed on all the coatings. The influence of oxidation time on the surface morphology is negligible. The average number of micropores seems to be the smallest for the MAO coating produced at 5 min. The samples produced at 8 min have the largest micropores. From surface morphology, it is difficult to determine the density of the coating sample. Porosity values are needed to estimate the sample compactness.

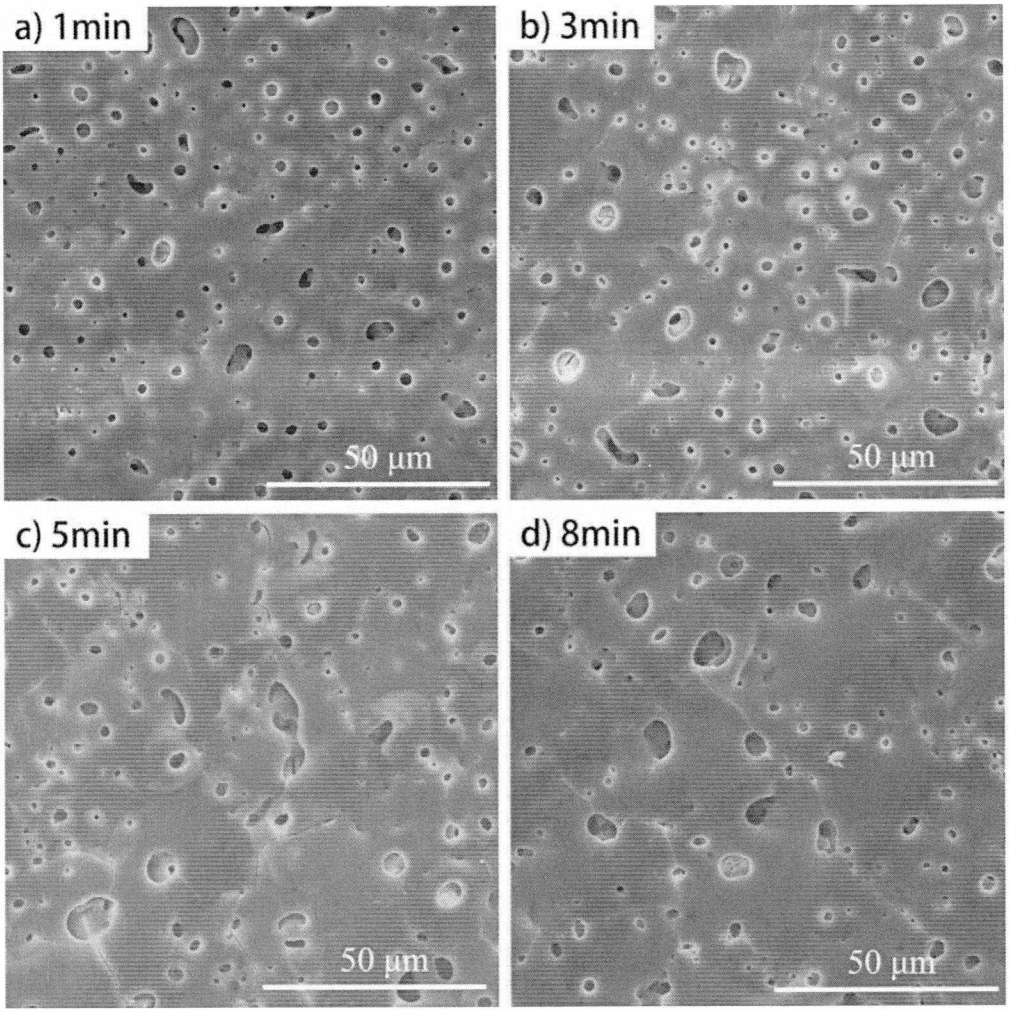

Figure 2.7 Surface morphology of MAO coatings produced at various oxidation times: (a) 1 min, (b) 3 min, (c) 5 min and (d) 8 min.

The cross-sectional morphologies of the MAO coatings produced at various oxidation times are illustrated in Figure 2.8. It can be seen that the thickness increased with increasing oxidation time until 5min. When the oxidation time reaches 8 min, the thickness seemed to be decreasing and the coating also becomes rough. Some parts of the coating are disintegrated. More voids are formed locally and a large amount of melting accumulated. This is due to the high temperature and the pressure at higher oxidation time. The smallest coating thickness owing to the shortest oxidation time of

1 min is shown in Figure 2.8a. The sample coated for 5 min (Figure 2.8d) shows the thickest layer with a relatively smooth and uniform microstructure with fewer micropores, compared to the other oxidation times.

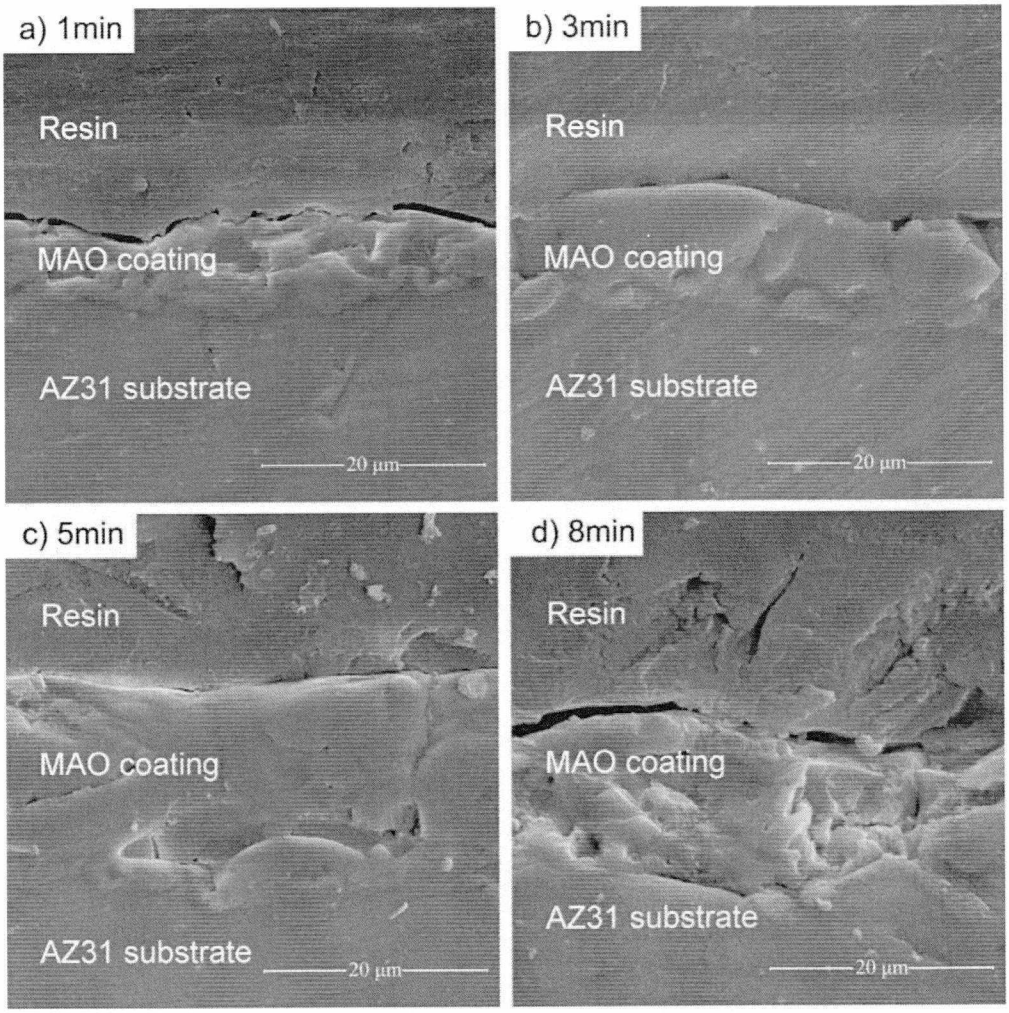

Figure 2.8 Cross-sectional morphology of MAO coatings produced at various oxidation times: (a) 1 min, (b) 3 min, (c) 5 min and (d) 8 min.

2.4.1.4 Effect of Electrolyte Concentration

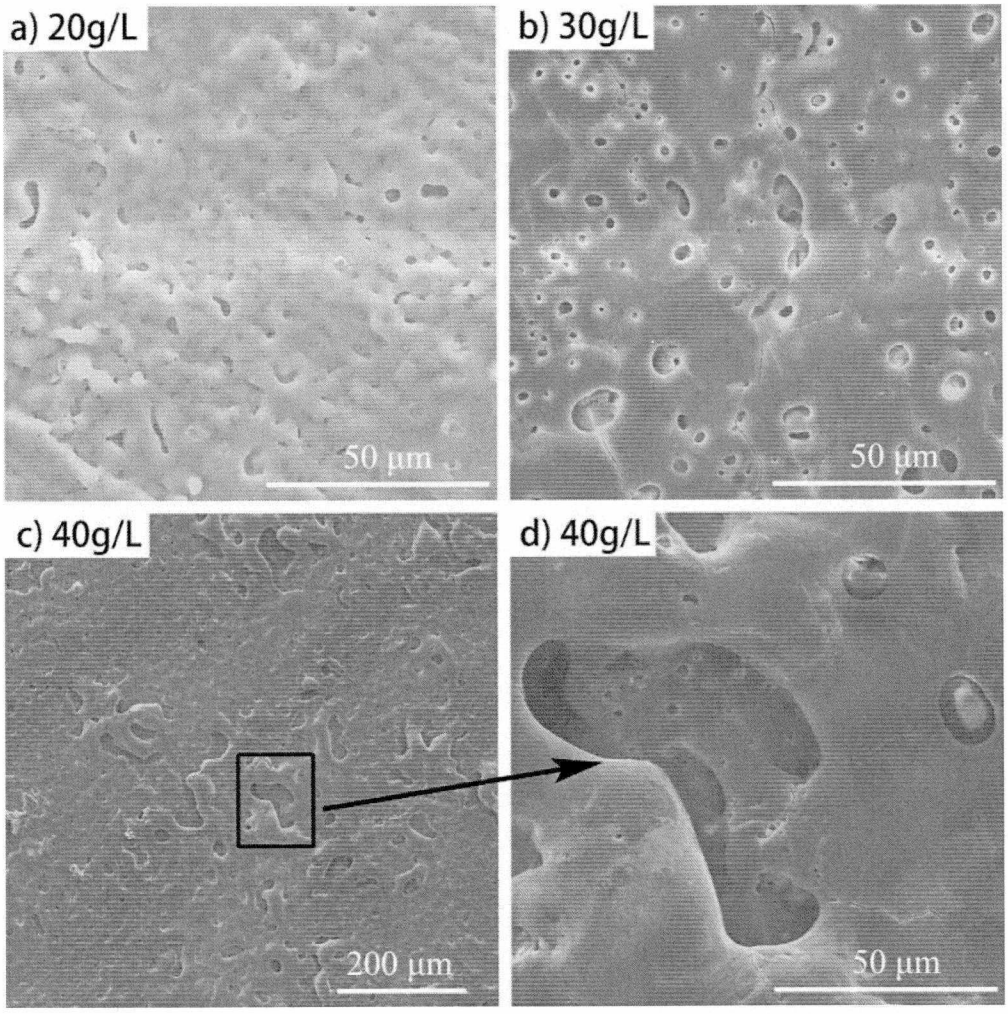

Figure 2.9 Surface morphology of MAO coatings produced at various electrolyte concentrations: (a) 20 g/L; (b) 30 g/L; (c-d) 40 g/L.

The surface morphologies of the MAO coatings produced at various electrolyte concentrations are shown in Figure 2.9. Typical porous microstructures can be observed on the coatings. The influence of the electrolyte concentration on the surface morphology is evident. At a concentration of 20g/L, a well developed melt network is produced. This is due to an incomplete coating (Figure 2.9a). This could be attributed

to fewer electrolyte particles participating in the reaction, and the partial discharge of the plasma. With increasing electrolyte concentration, the micropores increases gradually, and the coating layer tends to be denser. The reaction energy increases during the MAO process with increasing electrolyte concentration. When the concentration is increased to 40 g/L, the surface morphology is very different. Ablation with large pores (Figure 2.9d) occurs locally, which is due to a large discharge spark caused by the participation of large amount of electrolyte particles.

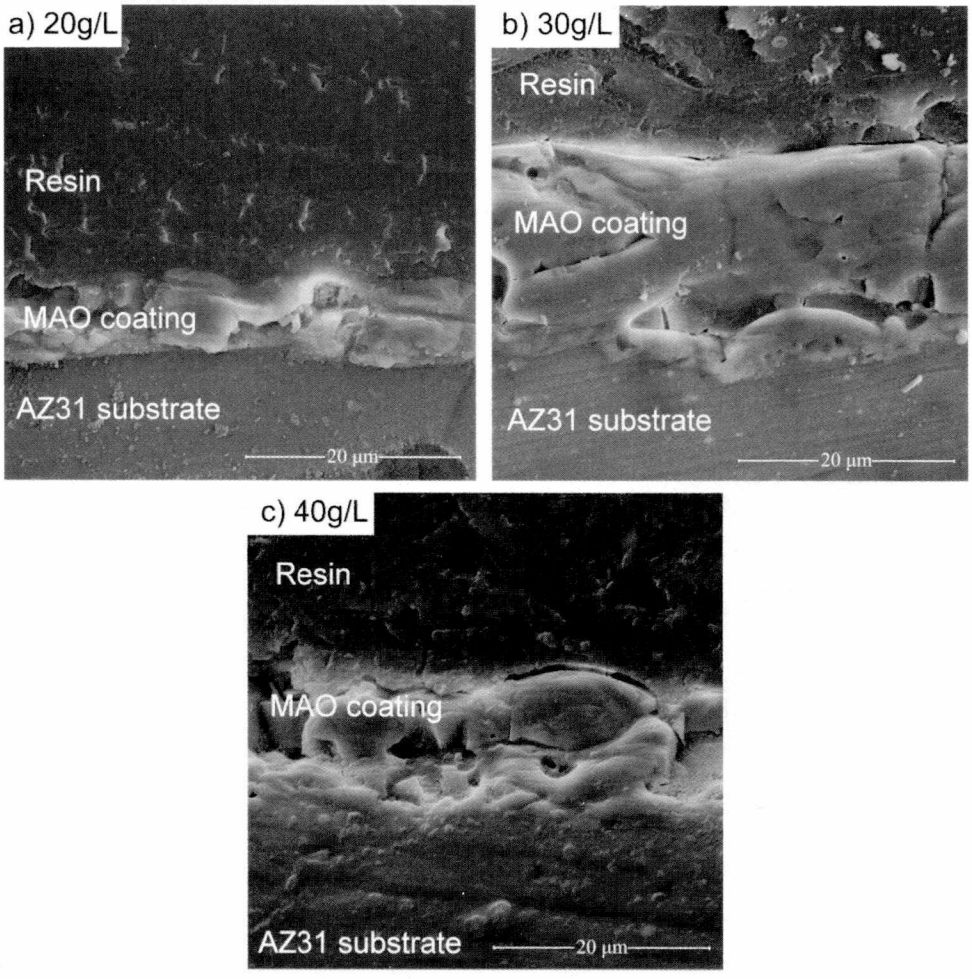

Figure 2.10 Cross-sectional morphology of MAO coatings produced at various electrolyte concentrations: (a) 20 g/L, (b) 30 g/L and (c) 40 g/L

The cross-sectional morphologies of the MAO coatings produced at various electrolyte concentrations are presented in Figure 2.10. It can be seen that the adhesion between the coating and the substrate is good without any visible separation boundary. The coating seems to be very thin for the 20g/L treated sample because of the low electrolyte concentration. The sample coated at higher concentration of 40 g/L shows (Figure 2.10c) a rough morphology with numerous pores and cracks. The coating produced at an electrolyte concentration of 30g/L displayed a more uniform and thicker morphology. The results suggest that the concentration of electrolyte has significant effects on the cross-sectional morphologies.

2.4.2 Porosity Measurement of MAO coatings

The presence of pores, such as closed pores, open pores and pinholes, in the coatings means that the film density and the compactness are less than those of the bulk material. Corrosion-resistant coatings are primarily controlled by the amount of porosity. The experimental methods to measure porosity of the coatings on the substrates are shown in Table 2.3 [79]. The direct porosity measurements are only qualitative and time-consuming [80]. In recent literature, various electrochemical methods have been proposed to determine through-coating porosity. The presence of pores and pinholes in the coatings is indirectly obtained from the measurements of the through pores.

Table 2.3 Experimental methods for the detection of porosity in the coatings [79].

Type of detection	Experimental method
Direct observation	Chemical etching
	Optical metallography
	Scanning electron microscopy
	Transmission electron microscopy
Indirect measurement	(a) Pore resistance method
	(b) Electrochemical method
	(b1) Potentiodynamic polarization test
	(b2) Electrochemical impedance spectroscopy

In this research, the porosity of the MAO coating was evaluated by the potentiodynamic polarization method. For measuring the porosity, the coated samples were immersed in the SBF for a duration of 0.5 hour. The details of polarization method are presented in Section 4.2. The coating porosity (F) polarization results using Equation 1 [81, 82]: is calculated from the

$$F = \left(\frac{R_{pm}}{R_p}\right) \times 10^{-|\Delta E_{corr}/\beta_a|} \qquad \text{Equation 1}$$

Where, R_{pm} is the polarization resistance of the uncoated sample, R_p the polarization resistance of the MAO-coated sample, $\boldsymbol{\Delta E_{corr}}$ the difference of corrosion potential between the coated and the uncoated samples, and β_a is the anodic Tafel slope of the uncoated sample.

A comparison of the potentiodynamic polarization curves of uncoated AZ31 Mg alloy and the coated specimens produced at various control parameters is shown in Figure 2.11. The corrosion potential (E_{corr}), corrosion current density (I_{corr}), and the anodic /cathodic Tafel constants (β_a and β_c) were obtained directly from the

potentiodynamic polarization curves using the Gamry Echem Analyst software. The polarization resistance (R_p) can then be calculated by the Stern–Geary equation:[83]

$$R_p = \frac{\beta_a \beta_c}{2.3 I_{corr} (\beta_a + \beta_c)} \qquad \text{Equation 2}$$

The Tafel data for the MAO coatings produced at various control parameters and the uncoated AZ31 alloy after immersion in the SBF for 0.5 h are listed in Table 2.4.

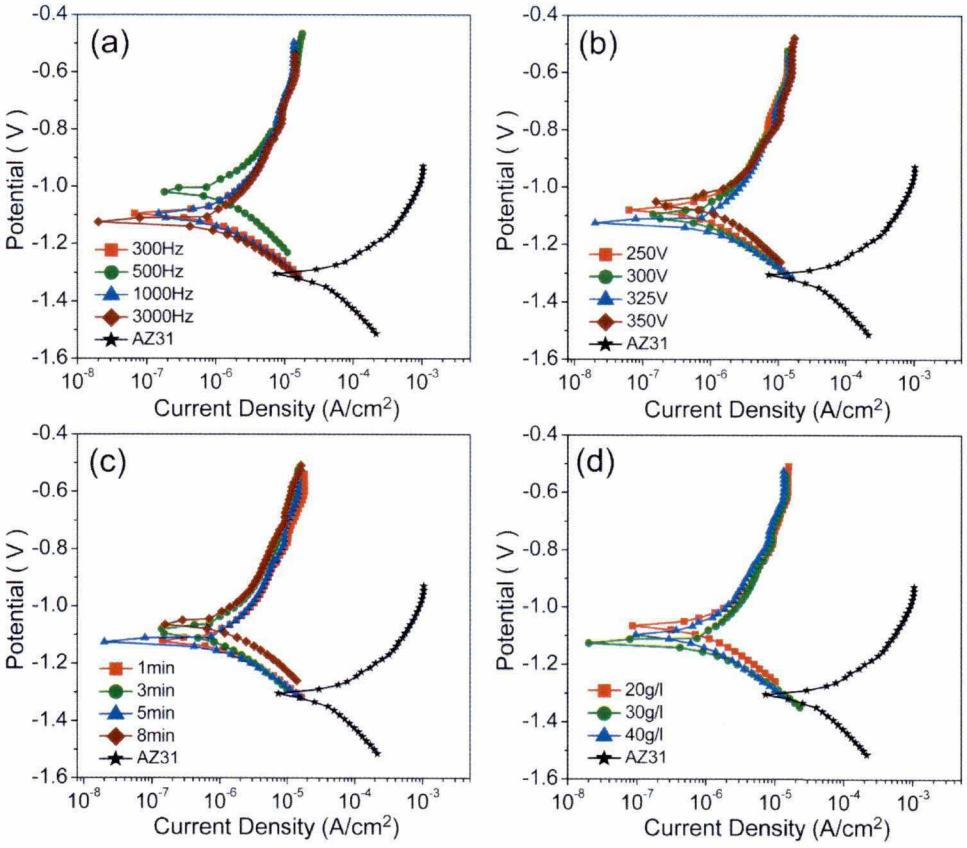

Figure 2.11 Tafel curves of uncoated AZ31 alloy and MAO coatings produced at various a) pulse frequencies b) applied voltages c) oxidation times and d) electrolyte concentrations after immersion in the SBF for 0.5 h.

Table 2.4 Tafel data for uncoated and MAO-coated AZ31 alloy after 0.5h immersion in the SBF.

Sample		E_{corr} (V)	I_{corr} ($\mu A/cm^2$)	β_a (v/decade)	β_c (v/decade)
Group 1	300Hz	-1.10	2.66	0.698	0.290
	500Hz	-1.02	2.78	0.680	0.316
	1000Hz	-1.10	2.42	0.458	0.395
	3000Hz	-1.12	1.48	0.516	0.233
Group 2	250V	-1.08	2.03	0.585	0.290
	300V	-1.10	1.78	0.643	0.237
	325V	-1.12	1.48	0.516	0.233
	350V	-1.06	1.92	0.552	0.287
Group 3	1min	-1.12	3.01	0.675	0.278
	3min	-1.09	1.92	0.558	0.176
	5min	-1.12	1.48	0.516	0.233
	8min	-1.06	1.72	0.712	0.168
Group 4	20g/L	-1.07	3.47	0.637	0.307
	30g/L	-1.12	1.48	0.516	0.233
	40g/L	-1.10	1.93	0.600	0.260
AZ31 alloy		-1.31	97.38	2.579	0.810

Using the data presented in Table 2.4 and equations 1 and 2, the coating porosity (F) was calculated. The results are listed in Table 2.5. The results indicate that the porosity (%) is in the range of 4.93% to 8.55%. The porosity values are very similar to the data presented by Cai [84]. The Group 1 samples show a decrease in porosity value with increasing pulse frequency. For Group 2 samples, the porosity decreases with increasing applied voltage until 325 V, and then increases to 5.15% at 350 V. For Group 3 samples, the porosity for the coating produced at a 30 g/L concentration showed the lowest value (4.93%), and the highest value (8.55%) occurred at 20 g/L. For Group 4 samples, the porosity decreased with increasing the oxidation time until an oxidation time of 5 min, and then increases to 5.59% for an oxidation time of 8 min.

The smallest porosity of 4.93% results at 3000 Hz, 325 V, 30g/L for an oxidation time of 5 min. The densest coating was produced at these operating parameters.

Table 2.5 Calculated porosity of the MAO coatings by Equation 1.

Pulse frequency (Hz)	300	500	1000	3000
Porosity (%)	6.82	6.30	5.99	4.93
Applied voltage (V)	250	300	325	350
Porosity (%)	5.60	5.39	4.93	5.15
Oxidation time (min)	1	3	5	8
Porosity (%)	8.17	7.45	4.93	6.42
Electrolyte concentrations (g/L)	20	30	40	
Porosity (%)	6.73	4.93	5.47	

2.4.3 Element Concentration

In order to determine the phosphorous content in the coating, a dispersive XRF analysis was performed on the surface of Group #1 samples coated at various pulse frequencies. The XRF spectrum is presented in Figure 2.12 and the element concentration is listed in Table 2.6. It was found that the phosphorous content was decreasing with increasing processing pulse frequency. The resultant coatings have a phosphorous content of 18.9, 18.8, 18.5 and 18.1 wt. % for 300 Hz, 500 Hz, 1000 Hz and 3000 Hz frequencies. The concentration of sodium was also found in decreasing order in the coatings as a function of frequency. This validates the effective participation of the Na^+ and the PO_4^{3-} ions in the MAO process at 300Hz, which is attributed to the relatively longer pulse-on-time, thus, providing a higher energy per pulse.

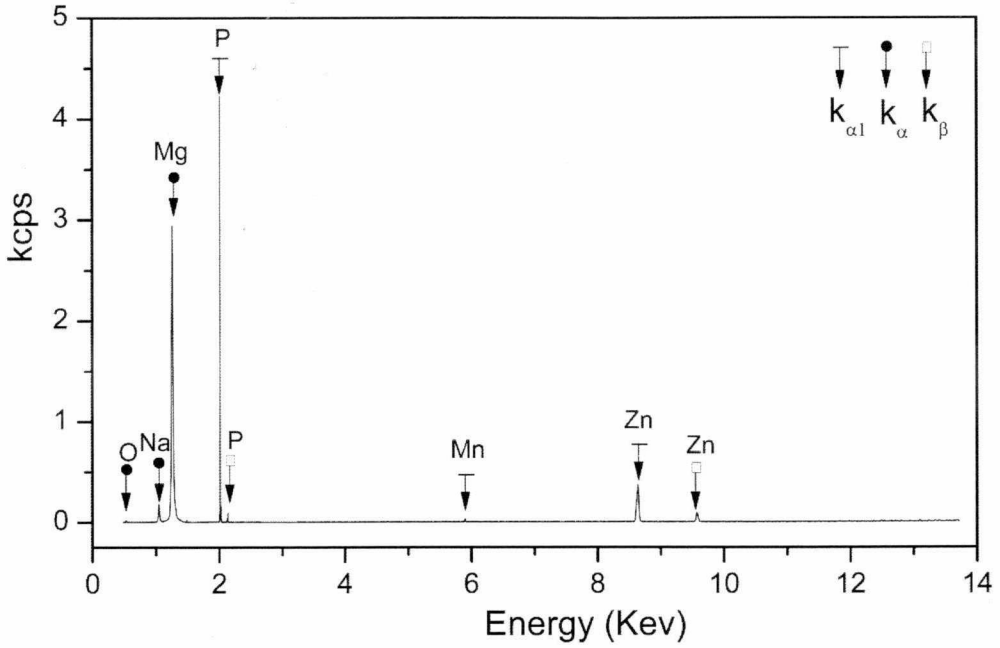

Figure 2.12 An example of XRF spectrum of MAO coating produced at 3000 Hz

Table 2.6 XRF element concentration of MAO coatings (wt.%).

Sample	O	Mg	P	Al	Zn	Na	Mn
300Hz	43.8	28.8	18.9	0.826	0.921	6.49	0.259
500Hz	45.4	28.7	18.8	0.546	0.980	5.25	0.322
1000Hz	46.8	28.3	18.5	0.406	0.909	4.82	0.241
3000Hz	47.3	28.1	18.1	0.691	0.970	4.51	0.318

2.4.4 Phase Composition

The XRD patterns of all the MAO coatings produced at various operating parameters are shown in Figure 2.13. The coating in each sample has the same phase compositions: Mg, MgO, $MgAl_2O_4$ and $Mg_3(PO_4)_2$. The result suggests that the processing parameters have negligible influence on the phase composition. The Mg phase, attributed to the AZ 31 substrate, exhibits a peak in the XRD pattern which differs from sample to sample. The MgO phase is least influenced by the control parameters. The $MgAl_2O_4$ phase has a low intensity for all the samples due mainly to

a small amount of Al present in the substrate AZ 31 alloy. The presence of $Mg_3(PO_4)_2$ suggests that the electrolyte ions participated in the growth process of the coating [85].

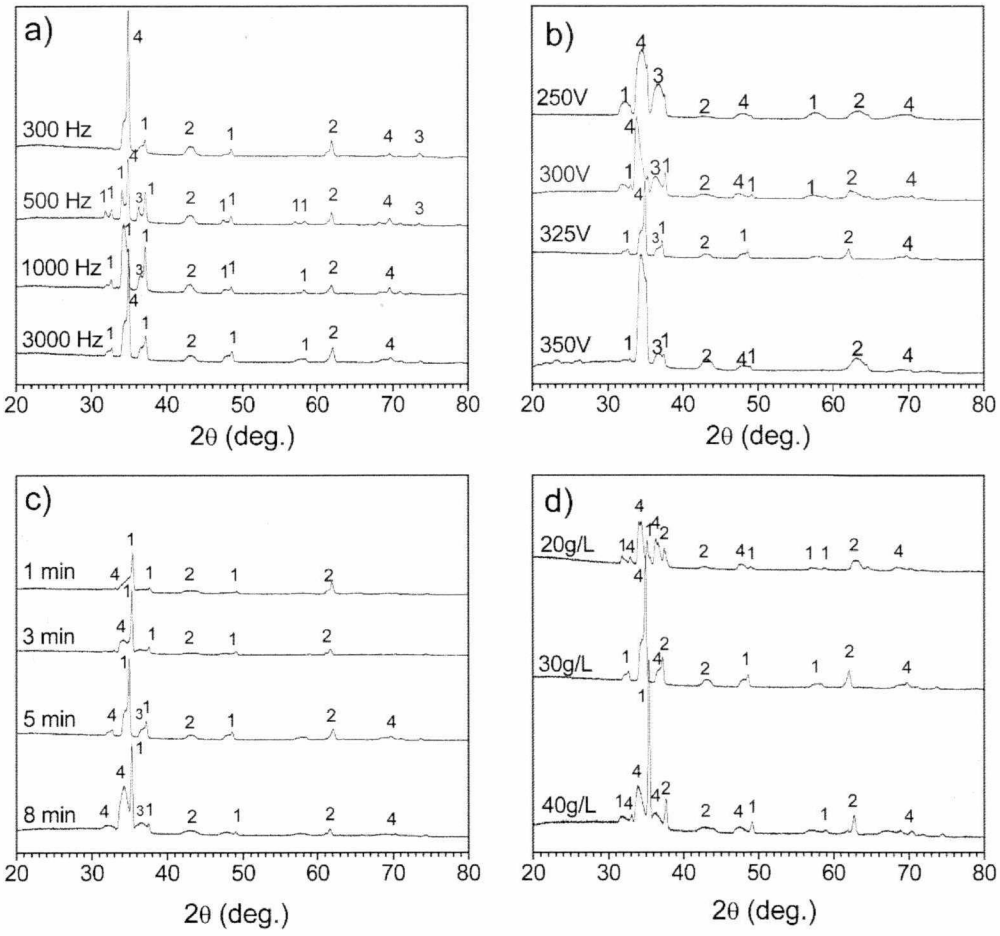

Figure 2.13 XRD spectra of MAO coatings produced at various a) pulse frequencies b) applied voltages c) oxidation times and d) electrolyte concentrations. (1) Mg; (2) MgO; (3) $MgAl_2O_4$; (4) $Mg_3(PO_4)_2$.

Chapter 3: Measurement and Modeling of Residual Stresses

Residual stress is one of the critical parameters of any implants in a human body. For long-term reliability, the residual stress in the implant must be low [86-90]. A considerable amount of research has shown that the compressive residual stress may cause the film delamination from the substrate, whereas, the tensile residual stress may lead to surface cracks in the films [91, 92]. Due to these facts, it is extremely important to develop an implant material with lower residual stress. It is, therefore, also very important to determine the level of residual stress in the MAO coated AZ31 Mg alloys.

There are several methods commonly used to determine stress in the coatings: (1) mathematical modeling (analytical or numerical), (2) material removal techniques (hole drilling, layer removal), (3) mechanical methods (curvature, displacement, fracture or strain measurement) and (4) X-ray diffraction or neutron methods. Each technique has certain advantages and its own limitations. The applicability of a particular method is determined by such factors as the shape, dimensions, materials used in the coating and the substrate, the information on the constituents' properties and processing conditions. The most common non-destructive method to determine the residual strain and stress in crystalline materials is based on the X-ray diffraction (XRD) [93-97]. In this thesis, the residual stress was measured by the XRD method. The measurement of stress by XRD method has the advantages of shallow penetration depth, small change in penetration depth with respect to the ψ angle, and a small effect on the texture. Because of these reasons, the XRD is considered to be a more appropriate method for measuring the residual stress in the MAO coatings.

3.1 X-Ray Diffraction Residual Stress Technique

Stress determination by the X-ray diffraction method is based on the measurement of changes in the crystal lattice spacing, which manifest themselves as shifts in the angular positions of the respective diffraction peaks [98]. From a set of lattice spacing in different orientations and stress-free lattice spacing, an elastic strain tensor can be constructed, which is then converted to a stress tensor using the Hooke's law. In the present research, for stress calculation, a zero stress perpendicular to the film plane was assumed. When a beam of X-ray with a wavelength of λ is incident upon the surface of the samples, the diffraction of the X-ray occurs and can be represented by the Bragg's diffraction equation:

$$n\lambda = 2d\sin\theta \qquad \text{Equation 3}$$

Where, n is an integer, d is the crystal plane spacing, and θ is the Bragg's diffraction angle.

When residual stress exists in a sample, the crystal plane spacing, d, differs from d_0 of a sample with free residual stress. The strain, ε_ψ, in the incident angle, ψ, can be determined by the relative changes of the diffraction crystal plane spacing. The strain is also associated with the displacement of the diffraction peak, ie.,

$$\varepsilon_\psi = \frac{\Delta d}{d} = \frac{d_\psi - d_0}{d_0} = -\cot(\theta_\psi - \theta_0) \qquad \text{Equation 4}$$

Where, θ_0 and θ_ψ is the Bragg's angle at diffraction peak in a sample without and with residual stress. The residual stress, σ_ψ, of a thin film can be calculated from equation 5 [98]:

$$\sigma_{\psi} = -\frac{E}{2(1+\nu)} ctg\theta_0 \frac{\pi}{180} \frac{\partial(2\theta_{\psi})}{\partial(\sin^2 \psi)} \qquad \text{Equation 5}$$

Where, E is the Young's modulus, and v is the Poisson's ratio of the thin film. The relationship between $2\theta_{\psi}$ and the $Sin^2\psi$ is linear. The residual stress σ_{ψ} in the coating can be easily obtained by measuring various diffraction line displacements for varying sample tilt angle ψ.

3.2 Residual Stress Measurement

The residual stress in the MAO coating was measured by the XRD $Sin^2\psi$ method [97] using the diffracted peak (220) at $2\theta = 62.306°$. This 2θ angle was selected to correspond to the MgO phase, shown in Figure 2.13. A comparatively high-angle diffraction peak (220) reduces the errors in measurement and ensures a high sensitivity to the strain. [99, 100] The measurements were carried out at five different ψ values (0°, 7.5°, 15°, 22.5° and 30°) in the 2θ, ranging from 61.75° to 63.00°, with a step size of 0.0125°. For MgO constituent, $E = 248$GPa and $\nu = 0.187$.[101] was used in the calculation of residual stress. The change in the lattice spacing d at various ψ values leads to a shift in the corresponding peak. (Figure 3.1). The measured 2θ plotted against $\sin^2\psi$ is presented in Figure 3.2. The residual stress in the coating is determined by the slope of the linear regression of the 2θ vs. $\sin^2\psi$ plot.

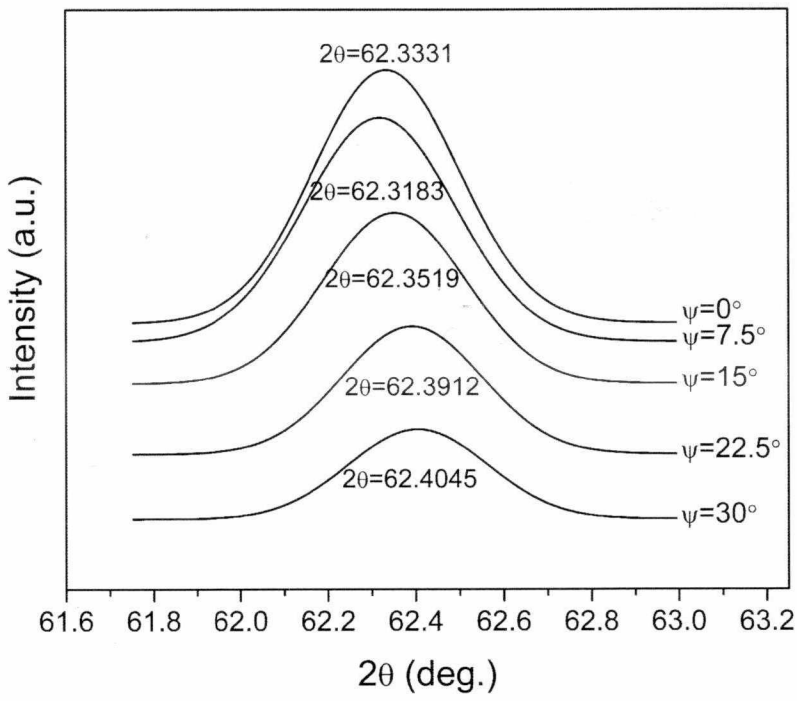

Figure 3.1 An example of XRD spectrum shift at different ψ values for MAO coating produced at 3000 Hz, 325 V, 30g/L for 5 min.

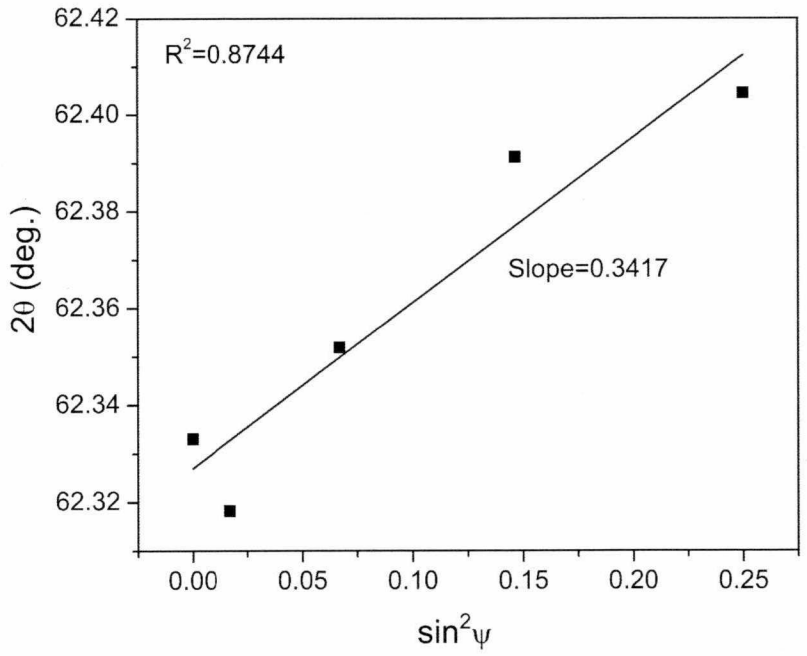

Figure 3.2 A plot of 2θ vs. $\sin^2 \psi$ values for MAO coating produced at 3000 Hz, 325 V, 30g/L for 5 min.

The calculated residual stresses in the MAO coatings are presented in Table 3.1. The stresses are compressive and range from a value of -611 to -1272 MPa. These values are lower than the residual stresses of Aluminum alloy reported by Lonyuk et al. [102]. Most of values (Table 3.1) are less than 1000 MPa, and are in the range of the results reported by Khan on Al alloys [103].

Table 3.1 Residual stresses in MAO coatings produced at various parameters.

Pulse frequency (Hz)	300	500	1000	3000
Residual stress (Mpa)	-1272	-1178	-1032	-611
Applied voltage (V)	250	300	325	350
Residual stress (Mpa)	-1254	-728	-611	-759
Oxidation time (min)	1	3	5	8
Residual stress (Mpa)	-1152	-784	-611	-896
Electrolyte concentration (g/L)	20	30	40	
Residual stress (Mpa)	-1206	-611	-837	

For the samples in Group 1, the residual stress decreases with increasing pulse frequency. For MAO coatings produced at various applied voltages, the stress decreases first with increasing voltages. The lowest value of -611 MPa is obtained at 325 V. The residual stress increases to a value of -759 MPa at 350 V. For samples in Group 3, the stress first decreases with increasing oxidation time until an oxidation time of 5 min is reached, then increases to a value of -896 MPa for an oxidation time of 8 min. The effects of electrolyte concentration on residual stress were also examined. The stress value is the lowest at the electrolyte concentration of 30 g/L and reaches the highest value of -1206 MPa at the electrolyte concentration of 20 g/L.

Porosity of a sample is a function of the density of the coating. Denser coating would result in smaller pores and cracks. The smaller porosity in a sample leads to small

residual stress. Since the porosity changes the equivalent Young's modulus and the Poisson's ratio of the coating, the residual stress in the coating is modified accordingly. The Stoney [76] equation (Equation 6) is used to correlate the coating stress σ_c to the mechanical properties of the coating and the substrate:

$$\sigma_c = \frac{E_s h_s^2 k}{6h_c(1-v_s)} \qquad \text{Equation 6}$$

Where, the subscripts c and s denote the coating and the substrate, respectively; E and v are the Young's modulus and the Poisson's ratio; the parameter k is the curvature of the coating-substrate composite, and h is the thickness. The Young's modulus E_s, Poisson's ratio v_s and the thickness h_s of the substrate were assumed to be the same for all the coatings. If these parameters are kept as constant, the σ_c in equation 6 then changes proportionally to the value of the ratio of k/h_c. From the results of the cross-sectional images and the porosity presented in Section 2.4, it can be seen that if the porosity is less, the coating is thicker. Furthermore, according to the Euler-Bernoulli beam theory[104], the curvature k under a fixed bending is inversely proportional to the equivalent Young's modulus. The equivalent Young's modulus of a porous material (such as the porous MAO coating) can be related to its porosity by:

$$E_p = E(1-F) \qquad \text{Equation 7}$$

Where, E_p is the equivalent Young's modulus, E is the Young's modulus of the bulk material, and F is the porosity. Therefore, the smaller the porosity, the larger is the E_p, thus, the less is the curvature. Additionally, the smaller the porosity, the greater is the h_c, and the ratio of k/h_c is less, thus the less is the residual stress. Using the

trend of the residual stress as a function of MAO control parameters (Figure 3.3), the Stoney equation can be used to explain the experimental data and to extrapolate the residual stress based on the measured thickness and the porosity of the coated samples.

3.3 Predictive Model of Residual Stress

3.3.1 Development of the Regression Equation

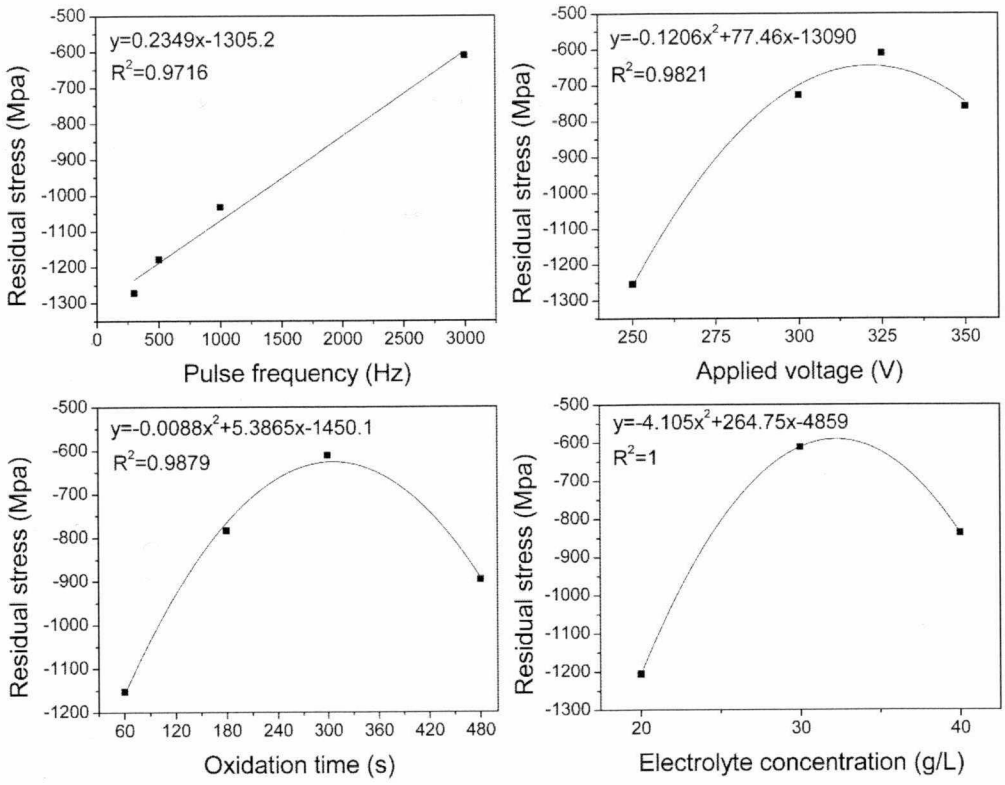

Figure 3.3 The regression of the residual stress with individual MAO process parameter

A regression equation was developed based on the calculated residual stress (Table 3.1) and the selected control variables. The regression equations between the residual stress with applied voltage, oxidation time and electrolyte concentration are second-order polynomials. The equation, however, is linear for the pulse frequency. Based

on the regression equations (Figure 3.3), the proposed mathematical model for predicting residual stress in the coating is:

$$Y = ax_1+bx_2^2+cx_2+dx_3^2+ex_3+fx_4^2+gx_4+h \qquad \text{Equation 8}$$

Where, Y represents the residual stress, MPa. The dependent variables x_1, x_2, x_3 and x_4 denote the pulse frequency, applied voltage, oxidation time and the electrolyte concentration, respectively. The raw (measured) data for non-linear multi-variable regression for residual stress are presented in Appendix B. The constants in the regression equation a, b, c, d, e, f, g and h are the regression coefficients, and the values of these coefficients are obtained from least squares regression. The coefficient values are shown in Table 3.2.

Table 3.2 The regression coefficients for predictive model of residual stress

a	b	c	d
2.23E-1	-1.27E-1	8.17	-8.77E-3
e	f	g	h
5.37	-3.94	2.55E2	-1.93E4

The measured and the simulated residual stresses are presented in Figure 3.4. The coefficient of multiple determination (R^2=0.9660) is very high, thus suggesting that the predictive model accurately reflects the measured data. The predictive model for the residual stress is written in Visual Basic (VB). A program panel is shown in Figure 3.5 and the program code is listed in appendix A.

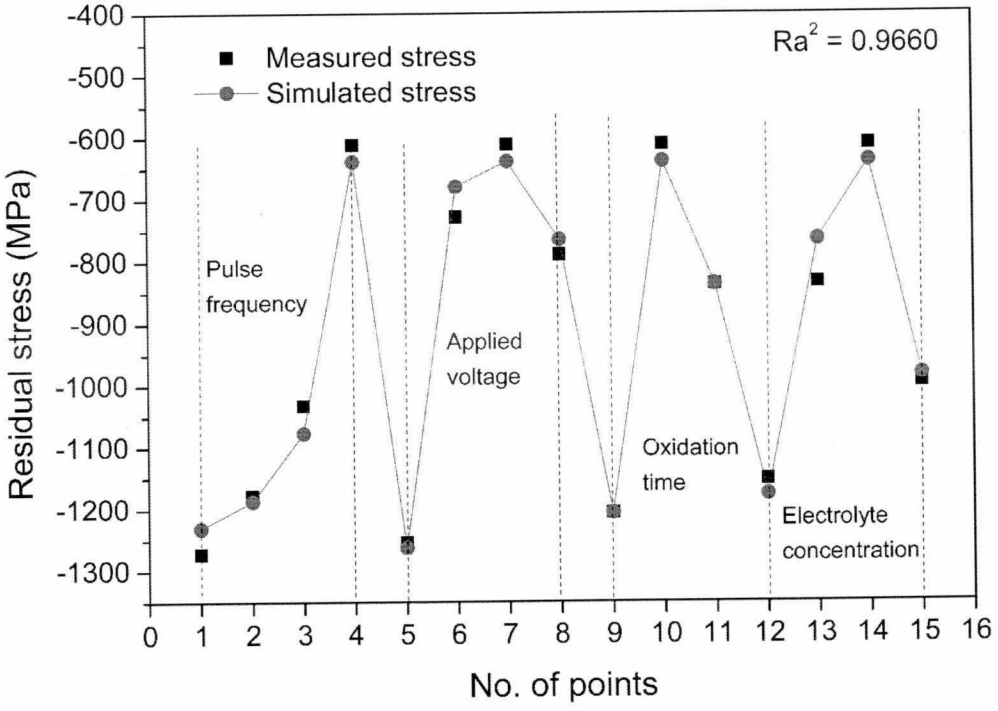

Figure 3.4 The comparison of measured and simulated residual stresses in MAO coatings produced at various control parameters.

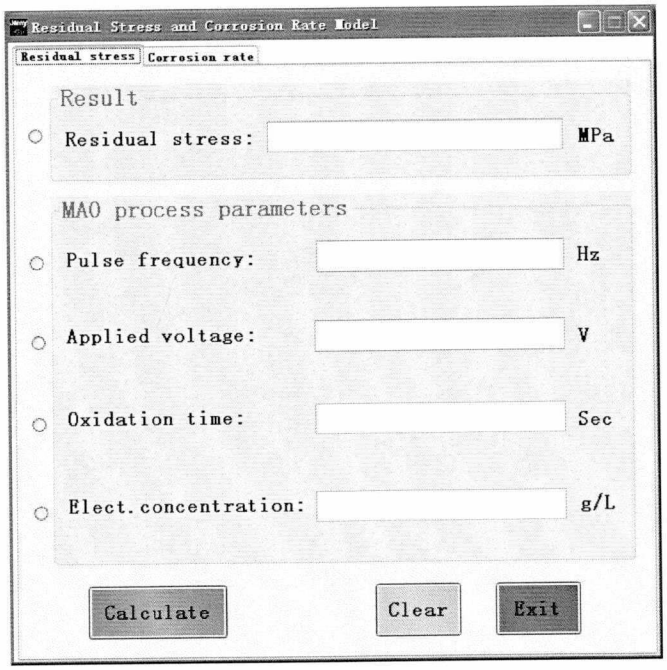

Figure 3.5 Executable program panel to predict the residual stresses in MAO coatings.

3.3.2 Principal Components Analysis

In order to identify any underlying patterns in the data, and to identify the contribution of each of the individual parameters, a principal components analysis (PCA) was conducted. The results of the PCA are shown in Tables 3.3 and 3.4. It can be seen that the ranked eigenvalue of the pulse frequency component is the highest, indicating that pulse frequency is the dominant factor towards residual stress.

Table 3.3 Eigenvector of MAO parameters for the modeling of residual stresses.

	Pulse frequency	Applied voltage	Oxidation time	Electrolyte concentration
Pulse frequency	0.737	-0.128	0.000	0.664
Applied voltage	-0.629	-0.489	0.000	0.604
Oxidation time	-0.248	0.863	0.000	0.441
Electrolyte concentration	0.000	0.000	1.000	0.000

Table 3.4 Eigenvalues of the eigenvector shown in Table 3.3.

	Pulse frequency	Applied voltage	Oxidation time	Electrolyte concentration
Eigenvalue	1.126	1.030	1.000	0.844
Variability (%)	28.143	25.762	25.000	21.096
Cumulative (%)	28.143	53.904	78.904	100.000

Chapter 4: Corrosion Behavior of MAO-coated AZ31 Mg Alloy

Potentiodynamic polarization is often used to provide useful information on the corrosion rate. Electrochemical Impedance Spectroscopy (EIS), on the other hand, is used to characterize the interface between a metal and the conductive solution. The combined information allows understanding of the corrosion mechanism and the approaches to reduce corrosion.

4.1 Electrochemical Corrosion Testing

In this research, the potentiodynamic polarization and EIS tests were used to evaluate the corrosion behavior of MAO coatings on Mg alloys. A brief description of the potentiodynamic polarization and EIS follows:

4.1.1 Potentiodynamic Polarization

Potentiodynamic polarization refers to a polarization technique in which the potential of the electrode is varied over a relatively large potential domain at a selected rate by the application of a current through the electrolyte. It includes a typical anodic or cathodic potentiodynamic scan. In a potentiodynamic experiment, the driving force (i.e., the potential) for anodic or cathodic reactions (depending on the nature of the scan) is controlled, and the net change in the reaction rate (i.e., current) is observed.

4.1.2 Electrochemical Impedance Spectroscopy

Electrochemical impedance spectroscopy (ElS) has been successfully applied to the study of corrosion systems and considered to be an accurate method for measuring impedance [92]. In this approach, a measure of the electrochemical impedance is made at a series of predetermined frequencies. An important advantage of EIS over other electrochemical techniques is the possibility of using very small amplitude

signals without significantly influencing the impedance properties. EIS in principle can determine a number of fundamental parameters relating to electrochemical kinetics [83].

The time-dependent current response *I(t)* of an electrode surface to a sinusoidal alternating potential signal *V(t)* is expressed as an angular frequency (ω) dependent impedance $Z(\omega)$,

$$Z(\omega) = V(t) / I(t) \qquad \text{Equation 9}$$

Where,

$t \equiv time$
$V(t) = V_0 \sin \omega t$
$I(t) = I_0 \sin(\omega t + \theta)$
$\theta = phase\ angle\ between\ V(t)\ and\ I(t)$

During EIS, the surface of the corroded sample absorb electrical energy at discrete frequencies, causing a time lag and a measurable phase angle, θ, between the time-dependent excitation and response signals. The impedance, $Z(\omega)$, may be expressed in terms of real, $Z'(\omega)$, and imaginary, $Z''(\omega)$, components.

$$Z(\omega) = Z'(\omega) + i \cdot Z''(\omega) \qquad \text{Equation 10}$$

The impedance behavior of an electrode can be expressed as Nyquist plots of $Z''(\omega)$ as a function of $Z'(\omega)$ or as Bode plots of $\log|Z|$ versus frequency f in cycles per sec (hertz), Where, $\omega = 2\pi f$.

4.2 Setup for Electrochemical Test

The electrochemical measurements were carried out in a conventional three-electrode

cell using a saturated calomel electrode (SCE) as the reference electrode and a graphite rod as the counter electrode. The exposed area of the working electrode is 4.18cm^2. All the experiments were performed at accepted human body temperature of 36.5±0.5 °C (97.7±0.9 ^{0}F) in the simulated body fluid (SBF) with an ionic concentration as follows: Na^+ 142.0, K^+ 5.0, Ca^{2+} 2.5, Mg^{2+} 1.5, Cl^- 147.8, HPO_4^{2-} 1.0, HCO_3^- 4.2 and SO_4^{2-} 0.5 mmol/L.

The composition of the SBF is presented in Table 4.1. The solution was buffered with tris (hydroxymethyl), minomethane ($(CH_2OH)_3CNH_2$), and 1.0 mol/L HCl to an equivalent pH of 7.25. The SBF was refreshed every 24 hours for the electrochemical tests.

In order to reach a stable potential, the open circuit potential (OCP) was monitored for a period of 10 min, then the polarization and the EIS data were collected at various intervals. The samples were exposed in the SBF for a duration of 28 days. The polarization curves were measured at a scanning rate of 0.5 mV/s. The EIS tests were carried out in the range of 0.1 Hz to 100 kHz with a voltage amplitude of 10 mV.

Table 4.1 Chemical composition of the SBF (pH 7.25, 1 L) [105].

Reagent	Purity (%)	Amount
NaCl	99.5	7.996 g
$NaHCO_3$	99.5-100.3	0.350 g
KCl	99.5	0.224 g
$K_2HPO_4 \cdot 3H_2O$	99.0	0.228 g
$MgCl_2 \cdot 6H_2O$	98.0	0.305 g
1 kmol/m^3 HCl	—	40 cm^3
$CaCl_2$	95.0	0.278 g
Na_2SO_4	99.0	0.071 g
$(CH_2OH)_3CNH_2$	99.9	6.057 g
1 kmol/m^3 HCl	—	Appropriate amount for adjusting pH

4.3 Corrosion Behavior Results

4.3.1 Potentiodynamic Polarization

The effects of MAO control parameters (pulse frequency, applied voltage, oxidation time and electrolyte concentration) on the potentiodynamic polarization are discussed in this section.

4.3.1.1 Effect of Pulse Frequency

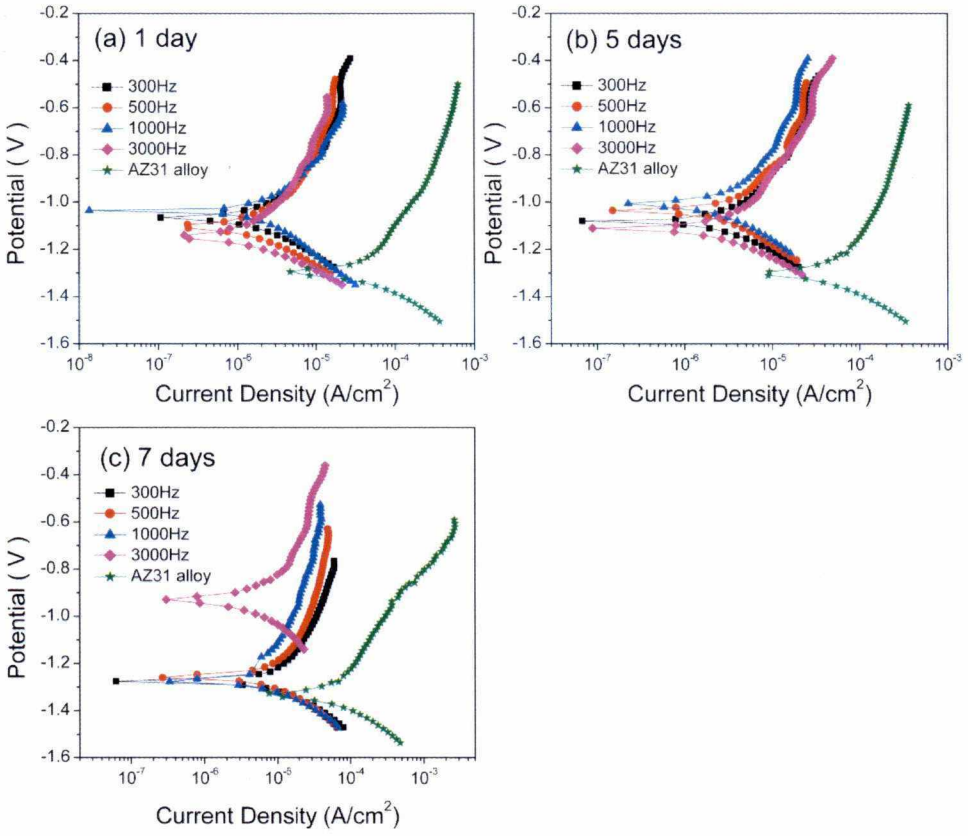

Figure 4.1 Tafel plots of uncoated AZ31 alloy and MAO coatings produced at various pulse frequencies (7 d immersion).

The potentiodynamic polarization curves of uncoated AZ31 alloy and MAO-coated samples produced at various pulse frequencies are shown in Figure 4.1. The important parameters such as the corrosion potential (E_{corr}) and the corrosion current density (I_{corr}), were generated directly from the potentiodynamic polarization curves by the Tafel method. The corrosion potential (E_{corr}) and the corrosion current density (I_{corr}) for the uncoated AZ31 alloy and MAO coatings produced at various pulse frequencies are listed in Tables 4.2 and Figure 4.2 respectively.

Table 4.2 Corrosion potential (V) for uncoated AZ31 alloy and MAO coatings produced at various pulse frequencies.

Immersion time (day)	300Hz	500Hz	1000Hz	3000Hz	AZ31 alloy
1	-1.07	-1.10	-1.14	-1.15	-1.30
5	-1.08	-1.04	-1.01	-1.11	-1.31
7	-1.27	-1.26	-1.27	-0.93	-1.33

It can be observed from Table 4.2 that all the coated samples show higher E_{corr} value than the uncoated AZ31 alloy irrespective of the immersion time. This suggests that the MAO-coated samples are less reactive to SBF as compared to the uncoated AZ31 alloys. At the end of the 7-day corrosion tests, the 3000 Hz samples have the highest E_{corr} value (-0.93 V). However, the MAO coatings produced at 300 Hz, 500 Hz and 1000 Hz show lower corrosion potential ranging from -1.27 V to -1.26 V.

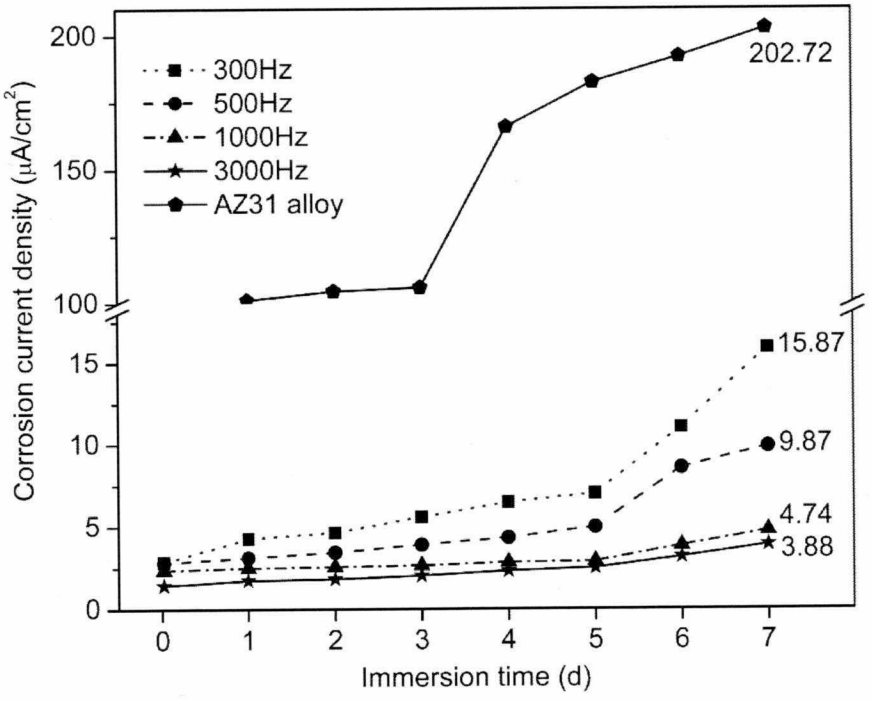

Figure 4.2 Corrosion current density of uncoated AZ31 alloy and MAO coatings produced at various pulse frequencies (7 d immersion).

The most commonly used method to determine the corrosion rates of coatings is the potentiodynamic polarization test [79]. Corrosion rate of the coatings is determined primarily on the basis of corrosion current density (I_{corr}). The lesser the I_{corr}, the smaller is the corrosion rate. From the corrosion current density shown in Figure 4.2,

It can be seen that after 7 days immersion, the I_{corr} value of the uncoated AZ31 alloy reaches the highest value of 202.72 $\mu A/cm^2$, indicating very poor corrosion resistance. All the coated samples, however, have much lower I_{corr} value than the uncoated AZ31 alloy. This indicates that the corrosion resistance of the AZ31 alloy is greatly enhanced by the MAO coating. In each case, the I_{corr} value increases with increasing immersion time. The increase of the I_{corr} value is relatively much larger after immersion of the samples for more than 5 days. The larger corrosion rate is due to the enlarged pores and cracks that may have been formed due to longer immersion. The I_{corr} has a decreasing trend with increasing frequency. After immersing the samples for a period of 7 days, the 3000 Hz treated samples exhibited the lowest corrosion current density (3.88 $\mu A/cm^2$), approximately 50 times slower than that of the uncoated AZ31 alloy.

4.3.1.2 Effect of Applied Voltage

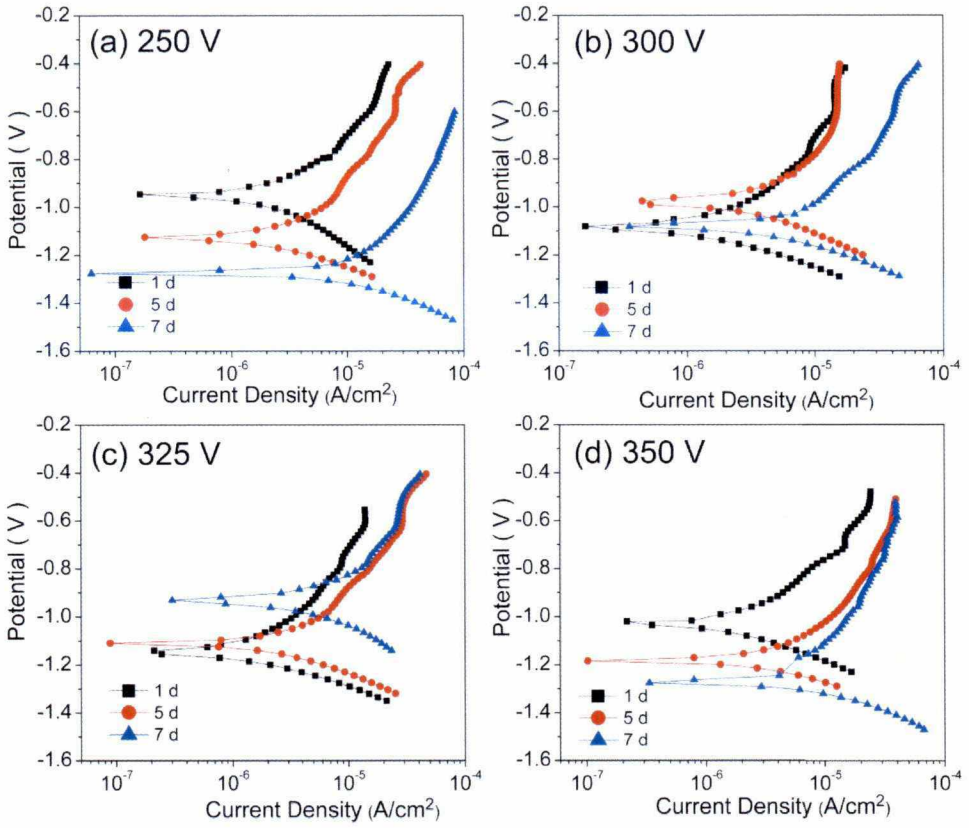

Figure 4.3 Tafel plots of MAO coatings produced at various applied voltages (7 days immersion).

The polarization curves for the MAO coatings produced at various applied voltages are shown in Figure 4.3. The corrosion potential (E_{corr}) and the corrosion current density (I_{corr}) for the MAO coatings produced at various applied voltages are listed in Tables 4.3 and Figure 4.4 respectively.

After immersing the samples in the SBF for a period of 7 days, the samples produced at 250V and 350V show the lowest corrosion potential (-1.27 V). While the 325V treated samples show the highest corrosion potential (-0.93 V). This suggests that the

samples produced at 325V are less reactive than the other MAO-coated samples.

Table 4.3 Corrosion potential (V) for MAO coatings produced at various applied voltages

Immersion time (d)	250V	300V	325V	350V
1	-0.95	-1.09	-1.15	-1.03
5	-1.13	-0.98	-1.11	-1.08
7	-1.27	-1.08	-0.93	-1.27

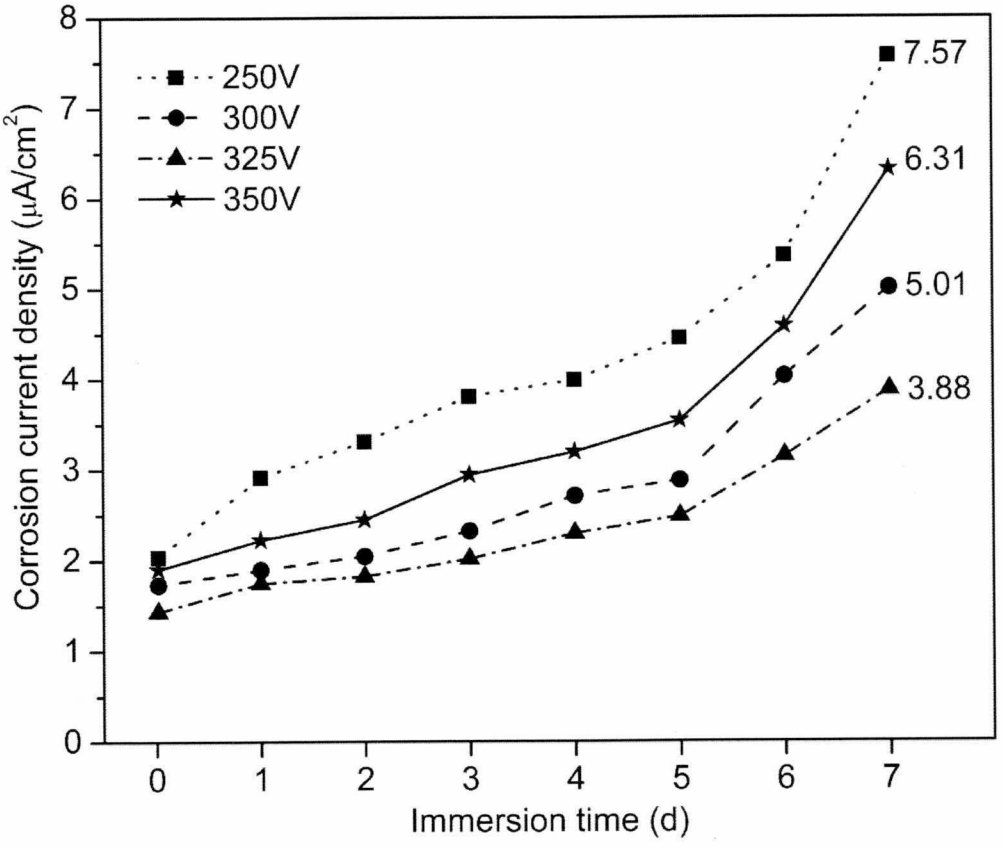

Figure 4.4 Corrosion current density of MAO coatings produced at various applied voltages (7 d immersion).

It can be seen from the data presented in Figure 4.4 that the corrosion current density increases with increasing immersion time for each sample. After immersing the samples for a period of 5 days, the I_{corr} value continues to increase more sharply until 7-day immersion. After 7-day immersion, the 250V treated samples show a high I_{corr} value of 7.57 $\mu A/cm^2$. The samples produced at 325V, however, offer a considerable corrosion protection (with a lowest corrosion current density of 3.88 $\mu A/cm^2$), indicating a superior corrosion resistance among this group samples.

4.3.1.3 Effect of Oxidation Time

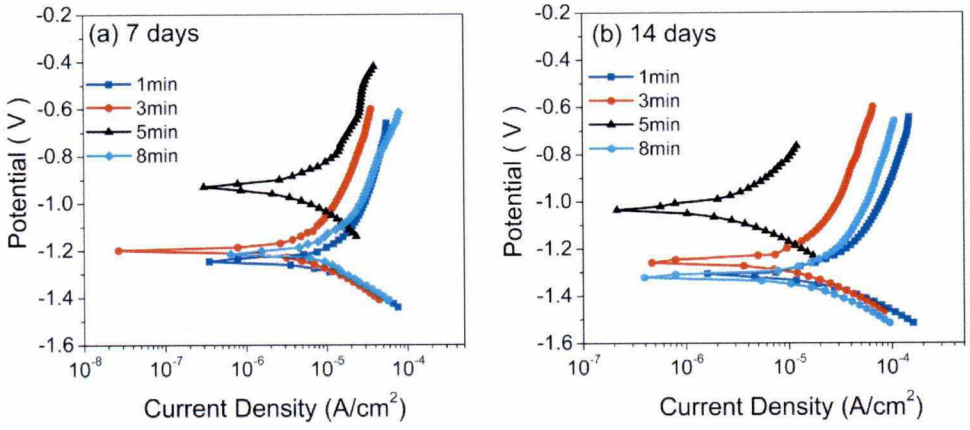

Figure 4.5 Tafel plots of MAO coatings produced at various oxidation times (14 d immersion).

Figure 4.5 shows the Tafel curves of the MAO coatings produced at various oxidation times after immersion in the SBF for 7 and 14 days. The corrosion potential (E_{corr}) and corrosion current density (I_{corr}) values are presented in Table 4.4 and Figure 4.6.

The E_{corr} value decreases with increasing immersion time, irrespective of the oxidation times. This indicates that the coated samples are more reactive at longer immersion time. The I_{corr} value increases with the increase of immersion time.

Table 4.4 Tafel data for MAO coatings produced at various oxidation times.

Sample	1min		3min		5min		8min	
Immersion time	7d	14d	7d	14d	7d	14d	7d	14d
E_{corr} (V)	-1.24	-1.31	-1.2	-1.26	-0.93	-1.03	-1.21	-1.32
I_{corr} ($\mu A/cm^2$)	16.14	21.52	9.35	17.93	4.01	10.97	5.26	14.63

From the corrosion current density shown in Fig. 4.6, it can be seen that all the coated samples show much lower value than the uncoated AZ31 alloy irrespective of the immersion time. This indicates that the corrosion resistance of AZ31 alloy is significantly enhanced by the MAO coating technique. For each sample, the I_{corr} value increases with increasing immersion time. After 14-day immersion, the I_{corr} value reaches the highest magnitude (62.1 $\mu A/cm^2$) for the MAO coating produced at 1 min, indicating that lesser MAO oxidation time does not produce an efficient protective coating on the Mg alloy. The MAO coating produced at 5 min has the lowest I_{corr} value, indicating that the coating is the most corrosion resistant when compared to the MAO coatings produced at other oxidation times (1 min, 3 min and 8 min).

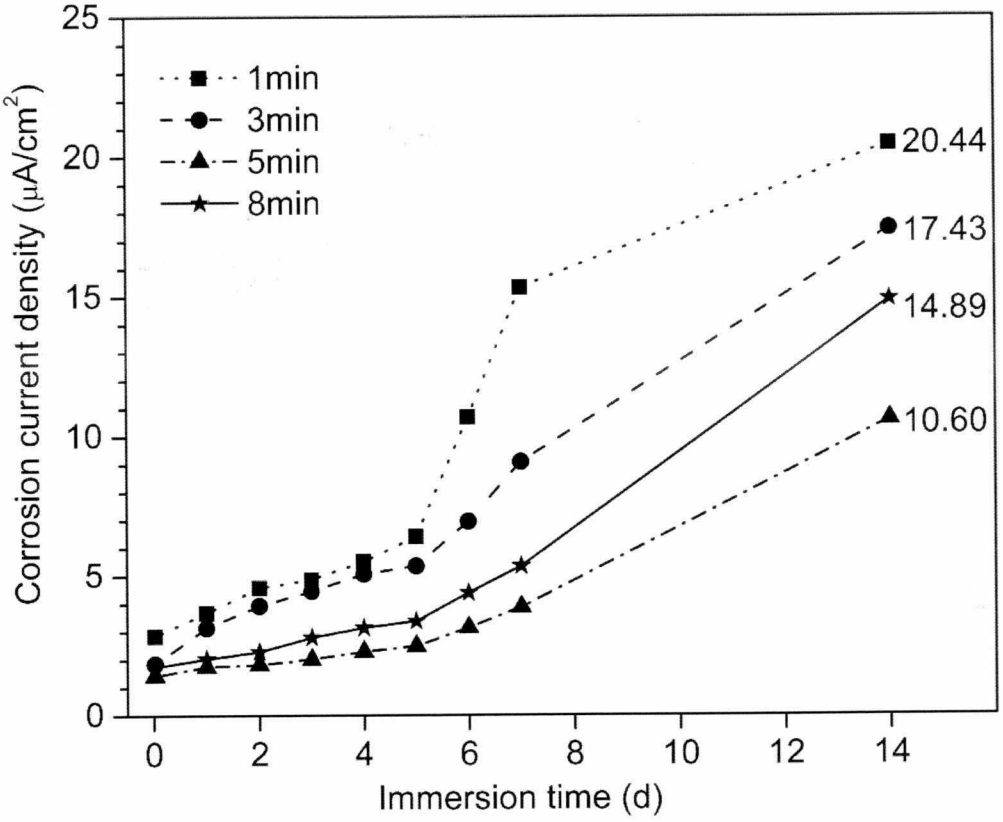

Figure 4.6 Corrosion current density of MAO coatings produced at various oxidation times (14 d immersion).

4.3.1.4 Effect of Electrolyte Concentration

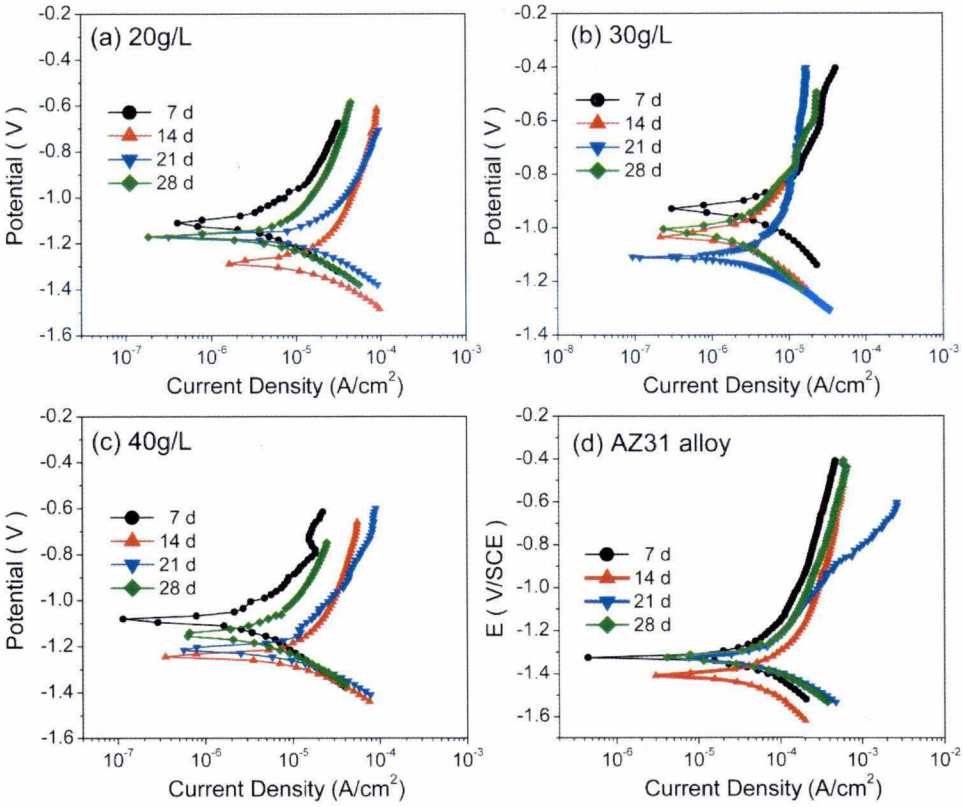

Figure 4.7 Tafel plots of uncoated AZ31 alloys and MAO coatings produced at various electrolyte concentrations (28 d immersion).

The Tafel plots of the MAO-coated AZ31 alloys produced at various electrolyte concentrations after immersion in the SBF for various durations are shown in Figure 4.7. The corrosion potential (E_{corr}), the corrosion current density (I_{corr}) and the Tafel slopes (β_a and β_c) were obtained by Echem Analyst software, and presented in Table 4.9.

Table 4.5 Tafel data of uncoated AZ31 alloy and MAO coatings produced at various electrolyte concentrations.

Immersion time	Sample	E_{corr} (V)	I_{corr} ($\mu A/cm^2$)	β_a (v/decade)	β_c (v/decade)
7 d	20g/L	−1.11	9.84	0.588	0.297
	30g/L	−0.93	3.88	0.512	0.297
	40g/L	−1.08	6.75	0.638	0.321
	AZ31 alloy	−1.32	202.72	3.390	0.745
14 d	20g/L	−1.28	27.99	1.954	0.422
	30g/L	−1.03	10.60	0.768	0.264
	40g/L	−1.24	18.31	1.458	0.375
	AZ31 alloy	−1.41	294.54	2.494	2.124
21 d	20g/L	−1.17	21.52	0.626	0.258
	30g/L	−1.13	9.15	0.400	0.197
	40g/L	−1.21	15.69	0.952	0.316
	AZ31 alloy	−1.33	215.55	1.136	0.589
28 d	20g/L	−1.17	18.20	1.093	0.331
	30g/L	−1.01	4.55	0.309	0.146
	40g/L	−1.15	11.94	1.552	0.289
	AZ31 alloy	−1.33	209.43	2.183	0.573

It can be seen from Table 4.9 that all the MAO-coated AZ31alloys have higher E_{corr} values (−0.94 ~ −1.28 V) than those of the uncoated AZ31 alloy (−1.31 ~ −1.41 V) at each immersion time. This indicates that the MAO-coated AZ31 alloys are relatively more stable than the uncoated samples. The MAO-coated samples produced at 30g/L electrolyte concentration has a higher E_{corr} value than the coatings produced at 20 g/L and 40 g/L concentrations, irrespective of the immersion times. These results suggest that samples produced at 30g/L concentration are less reactive than the other two samples.

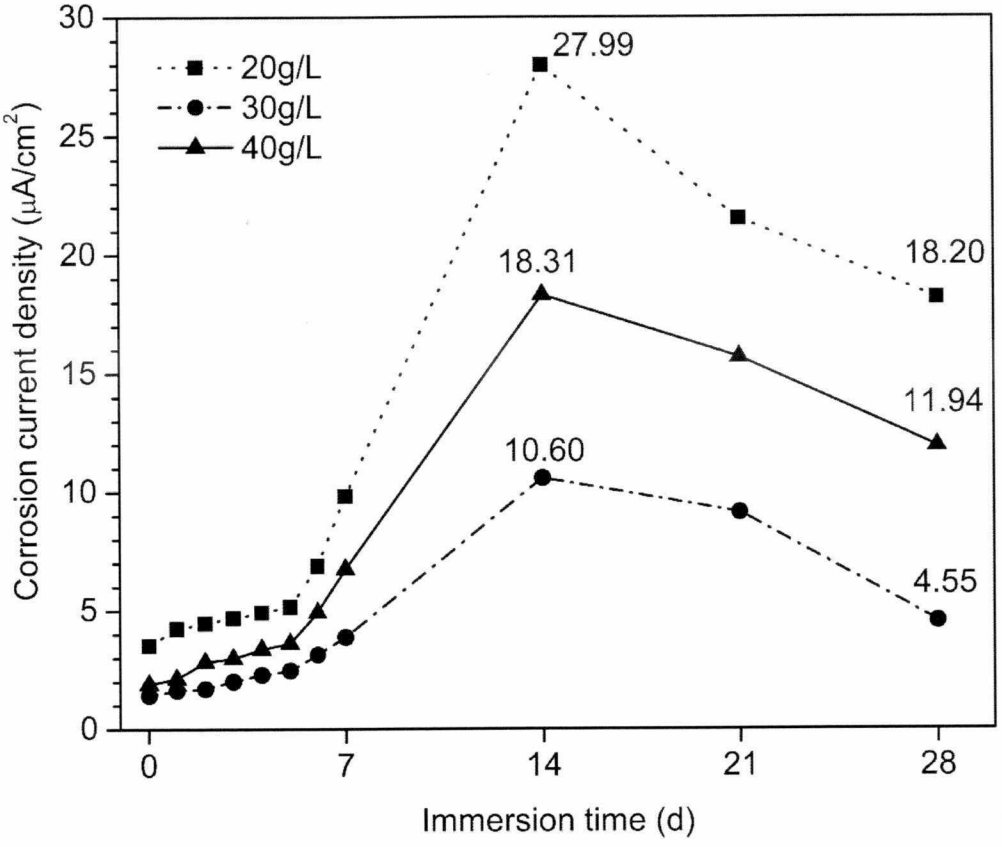

Figure 4.8 Corrosion current density of MAO coatings produced at various electrolyte concentrations (28 d immersion).

The plot of the corrosion current density versus immersion time is also presented in Figure 4.8. It can be seen that after 28 days immersion, all the coated samples have much lower I_{corr} value than the uncoated AZ31 alloy. This suggests that the corrosion resistance of the AZ31 alloy is greatly improved by the MAO coating. For each of the sample, the I_{corr} value increased with increasing immersion time up to 14 days, and then, decreased in the subsequent days. This is due to the formation of a corrosion product layer on the sample surface. The MAO coating produced at 30g/L concentration has the lowest corrosion current density (corrosion rate) among all the

MAO coatings, irrespective of the immersion time.

Based on the porosity calculation procedure presented in Section 2.4.2, the coating porosity (F) is calculated after an immersion of the samples in the SBF for 7 d, 14 d, 21 d and 28 d. The results are presented in Figure 4.9. A similar trend could be observed for all the three samples coated at the electrolyte concentration of 20 g/L, 30 g/L and 40 g/L. The porosity increased as a function of the immersion time until the 14th day. With a longer immersion time, the porosity decreased sharply from 40.38 to 13.53% for the 20g/L sample and then decreased rather slowly to 9.75% at the 28th day. In comparison, the porosity value is slightly higher than the samples after 7-day immersion (8.46%). It is also observed that the 30g/L samples have the lowest porosity value among the samples tested. Lower porosity values greatly enhance resistance to corrosion.

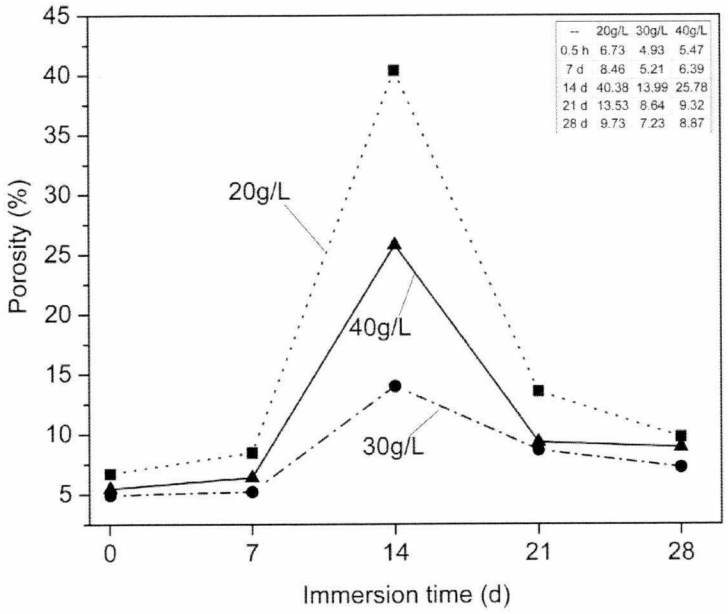

Figure 4.9 The porosity of MAO coatings produced at various electrolyte concentrations (28 d immersion).

4.3.2 Electrochemical Impedance Spectroscopy

Electrochemical impedance spectroscopy (EIS) was used to investigate the corrosion behavior of the MAO-coated specimens and the uncoated AZ31 alloy. For uncoated AZ31 alloy, the EIS data can be represented as an equivalent electrical circuit, shown in Figure 4.10a. For the coated samples, two equivalent circuits are proposed, shown in Figures 4.10b and 4.10c. These equivalent electrical circuits are based on the EIS studies on MAO coatings [71, 80, 106]. The EIS curves were fit by the equivalent circuit shown in Figure 4.11b. In the equivalent circuits, R_s is the solution resistance, R_{po} is the porous region resistance of the MAO coating in parallel with constant phase element (CPE) C_{po}; R_b is the barrier layer resistance of the MAO coating in parallel with C_b; R_{ct} is the resistance of the barrier layer-substrate interface in parallel with C_{dl}; R_{pa} is the passive layer resistance in parallel with C_{pa}.

Capacitors in an EIS experiment often do not behave ideally. Instead, they act as a constant phase element (CPE). The impedance (Z) of a CPE has the form [106]:

$$Z=(1/Y_0)/(j\overline{w})^{\alpha} \qquad \text{Equation 11}$$

Where, Y_0 is a CPE constant, j is the imaginary unit ($\sqrt{-1}$), ω is the angular frequency (1 rad/s) of the sine wave being considered as $\omega=2\pi f$, f is the frequency in Hz. The value of α ranges between 0 and 1. When this equation is used to describe a capacitor, the constant Y_0 = C (the capacitance) and the exponent $\alpha=1$. For a constant phase element, the exponent α is less than one. A "double layer capacitor", on real cells often behaves like a CPE instead of a capacitor.

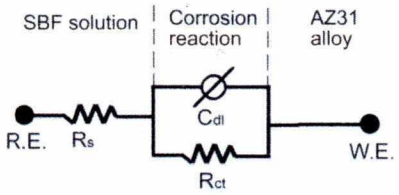

Figure 4.10 Equivalent electrical circuits used to fit the impedance data for uncoated AZ31 alloy

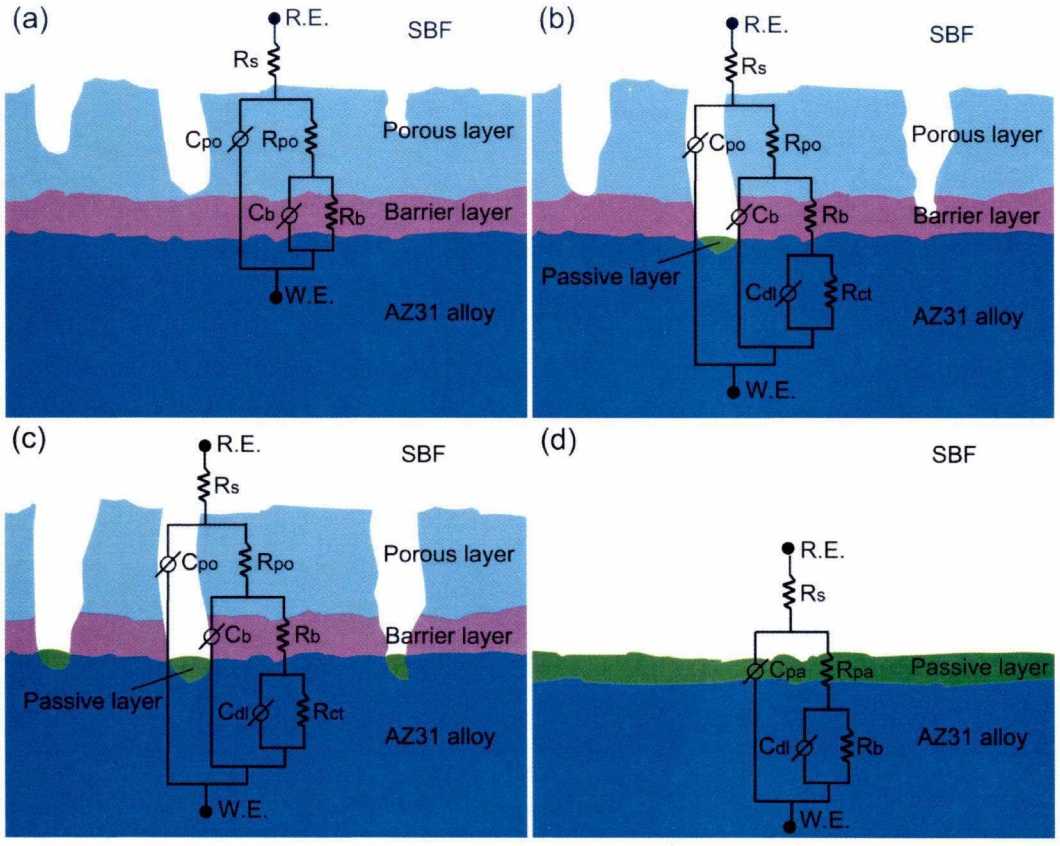

Figure 4.11 Equivalent circuits for fitting EIS data in a physical model of corrosion process of MAO coated AZ31 alloy immersed in the SBF. (a) 0-0.5h, (b-c) 0.5h-28 d and (d) ≥28 d

At the initial corrosion stage, the equivalent circuit (Figure 4.11a) includes two pairs of resistors and CPEs-the porous layer and the barrier layer of the coating. This means

that the SBF is not in contact with the substrate Mg alloy because of the shorter period of immersion. With increasing immersion time, the SBF starts to penetrate the porous layer and the barrier layer through the enlarged pores, and gradually move to the substrate. Therefore, the pair of $R_{ct}//C_{dl}$ is added to the equivalent circuit as shown in Figure 4.11b-c. During these above two stages, the corrosion products are slowly formed. The MAO coatings and the corrosion products can suppress the corrosion process by inhibiting the diffusion and the transport of the SBF to the substrate. Once the MAO coating deteriorates completely, the SBF is entirely in contact with the substrate, and would cause the formation of a passive layer on the surface of the AZ31 substrate (Figure 4.11d).

4.3.2.1 Effect of Pulse Frequency

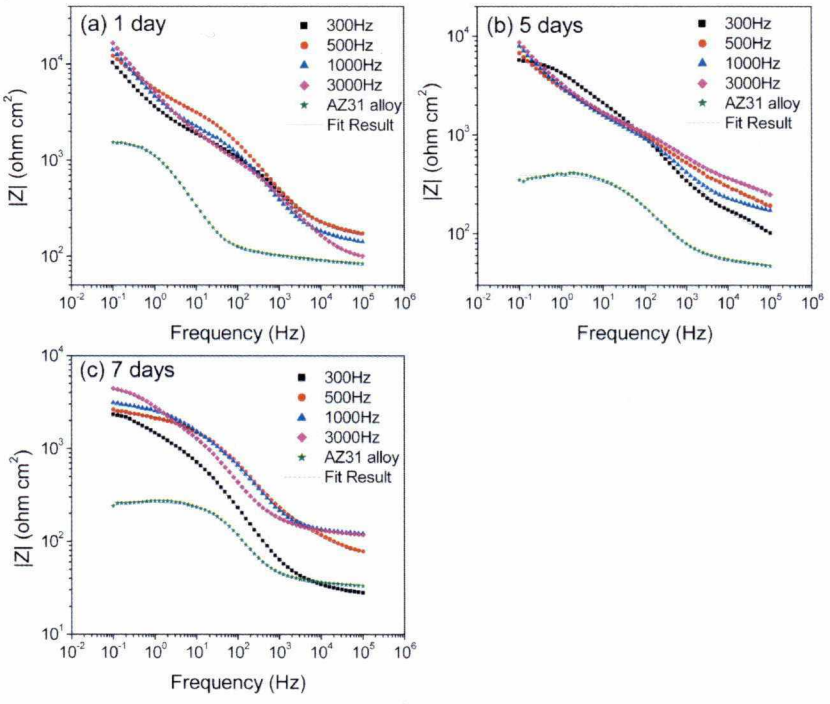

Figure 4.12 Bode plots of uncoated AZ31 alloy and MAO coatings produced at various pulse frequencies (7 days immersion).

The Bode plots of the samples after immersion in the SBF for a period of 7 days are presented in Figure 4.11. These samples were produced at various pulse frequencies. The corresponding EIS data are presented in Table 4.10. The resistance of the solution (R_s) is very low for all the samples because SBF is very conductive. The global impedance of all the coated samples is much higher than that of the uncoated AZ31 alloy. This indicates that the MAO is an effective coating technique which enhances the resistance to corrosion. From Table 4.10, it can be seen that the charge transfer resistance (R_{ct}) of the MAO coating is approximately 2 times and 5-15 times higher than the corresponding value of resistance of the porous layer (R_{po}) and the barrier layer (R_b), respectively. This suggests that the interface layer plays a key role in protecting the magnesium alloy from corrosion[71]. In addition, R_{po} and R_b decrease with increasing immersion time. This is due to the fact that the corrosive SBF enters the samples, reacts with the substrate, and enlarges the micropores in the MAO coating.

Table 4.6 EIS data for uncoated AZ31alloy and MAO coatings produced at various pulse frequencies.

Sample	Immersion time (d)	R_s ($\Omega \cdot cm^2$)	R_{po} ($\Omega \cdot cm^2$)	R_b ($\Omega \cdot cm^2$)	R_{ct} ($\Omega \cdot cm^2$)
300Hz	1	75	2317	6941	11658
	5	80	1012	3026	7215
	7	63	236	718	4136
500Hz	1	134	2576	7738	12507
	5	143	727	2081	8326
	7	35	248	764	6124
1000Hz	1	60	3358	9074	12623
	5	16	785	2655	8739
	7	75	335	1405	6425
3000Hz	1	73	4097	11291	12302
	5	114	1276	3928	7641
	7	68	459	1477	5063
AZ31 alloy	1	12	-		1534
	5	48	-		349
	7	35	-		240

Therefore, the charge transfer resistance (R_{ct}) is the dominating parameter influencing the electrochemical impedance of the coated samples. Figure 4.13 shows the R_{ct} value for all the specimens as a function of the immersion time. A sample with a higher R_{ct} value is more resistant to corrosion. It can be observed that all the coated samples have shown much higher charge transfer resistance values compared to the uncoated AZ31 alloy. It may be noted that higher the pulse frequency, the larger is the R_{ct}. Therefore, with larger R_{ct}, the coated samples are more resistant to corrosion than the AZ31 alloy. The samples produced at 3000Hz have the higher R_{ct} value.

It can also be observed that the R_{ct} value decreases with increasing immersion time. Specifically, for the samples coated at 300 Hz, 500 Hz and 1000 Hz, the R_{ct} value showed a steep drop after 5-day immersion. The results shown in Figures 4.13 and 4.2 taken together would suggest that for a constant immersion time, a steep reduction in

R_{ct} value would indicate a much higher corrosion rate (CR). The steep drop of the R_{ct} value is due to the penetration of the SBF in the MAO coating through the pores, reaching the substrate and thus causing the MAO coating to degrade rapidly. Thus, the 3000Hz treated sample demonstrates the slowest degradation among all the coated samples, since it has the highest R_{ct} value.

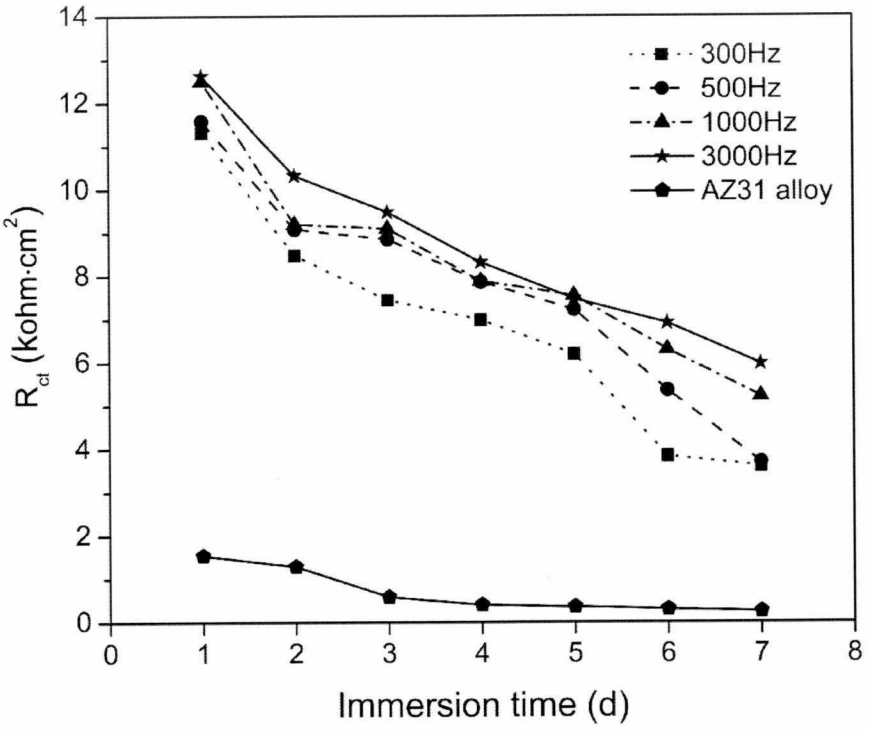

Figure 4.13 Charge transfer resistance of uncoated AZ31 alloy and MAO coatings produced at various pulse frequencies (7 d immersion).

4.3.2.2 Effect of Applied Voltage

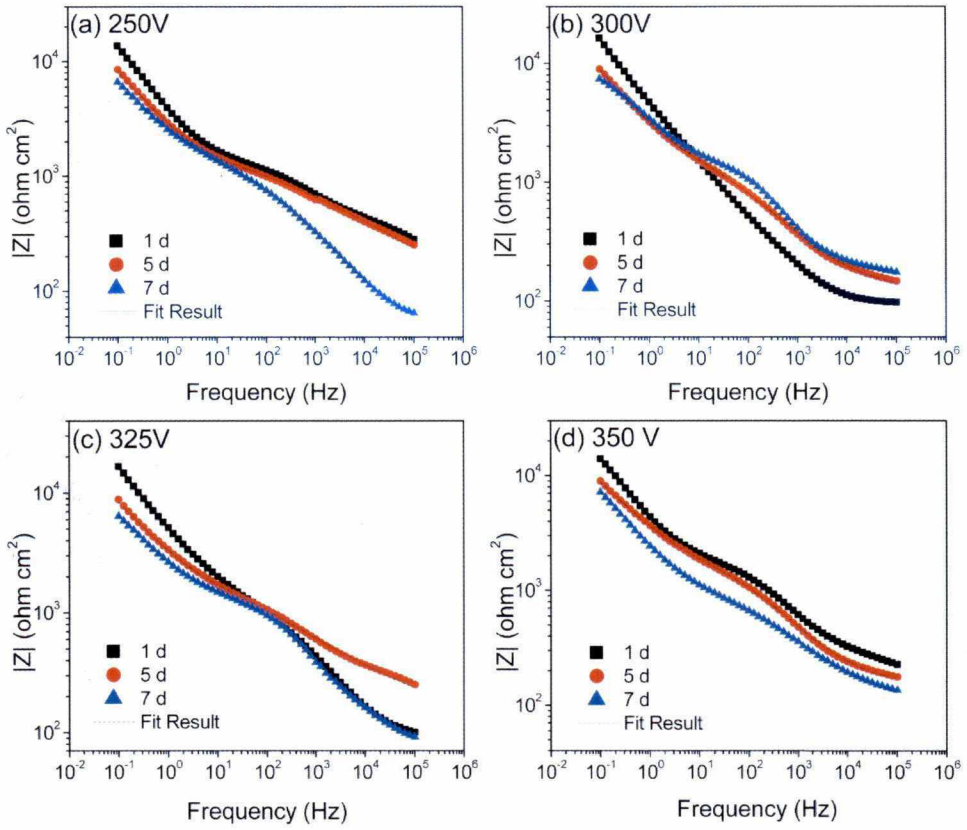

Figure 4.14 Bode plots of MAO coatings produced at various applied voltages (7 d immersion).

The Bode plots of the samples after immersion in the SBF for a period of 7 days are presented in Figure 4.14. These samples were produced at various applied voltages. The corresponding EIS data are shown in Table 4.11. From the Bode plots, it can be seen that the 325V treated samples have the highest total impedance, followed by the 300V samples.

Table 4.7 EIS data for MAO coatings produced at various applied voltages.

Sample	Immersion time (d)	R_s ($\Omega \cdot cm^2$)	R_{po} ($\Omega \cdot cm^2$)	R_b ($\Omega \cdot cm^2$)	R_{ct} ($\Omega \cdot cm^2$)
250V	1	83	1092	3286	11658
	5	30	1274	3812	7215
	7	0	153	489	4136
300V	1	85	1277	3931	12507
	5	118	632	1996	8326
	7	100	1066	3298	6124
325V	1	73	4097	11291	12623
	5	114	1276	3928	7463
	7	68	459	1387	6425
350V	1	165	1023	3169	12302
	5	147	1249	3947	7641
	7	86	697	2291	5063

It can also be observed that the R_{ct} value increases with increasing applied voltage up to 325 V, and then decreases for samples produced at 350 V, irrespective of the immersion times. For a specific applied voltage, however, the R_{ct} value decreases with increasing immersion time. At the end of 7-day immersion, the MAO coating produced at 325 V shows the highest R_{ct} value, indicating the slowest degradation rate among all the Group 2 samples produced at various applied voltages.

4.3.2.3 Effect of Oxidation Time

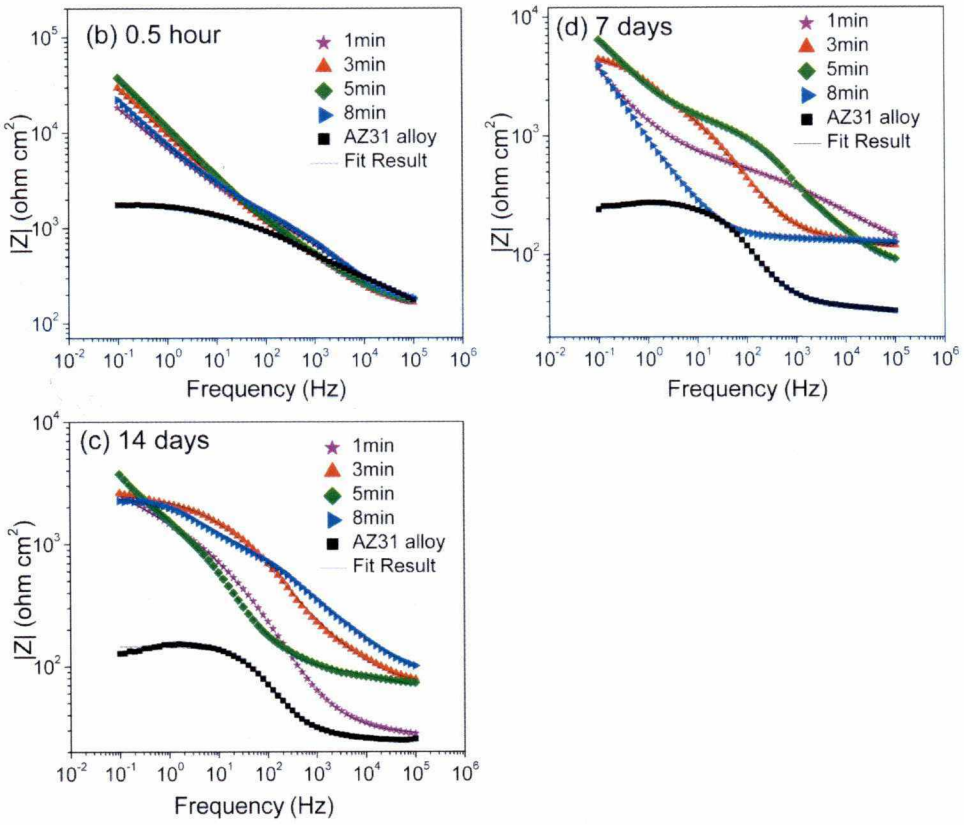

Figure 4.15 Bode plots of uncoated AZ31 alloy and MAO coatings produced at various oxidation times (14 d immersion).

The Bode plots of the samples after immersion in the SBF for a period of 14 days are presented in Figure 4.15. These samples were produced at various oxidation times. It can be seen that the global impedance of all the coated samples is much higher than the uncoated AZ31 alloy. This indicates that the MAO is an efficient coating technique which improves the corrosion resistance.

Table 4.8 EIS data for MAO coatings produced at various oxidation times.

Sample	Immersion time	R_s ($\Omega \cdot cm^2$)	R_{po} ($\Omega \cdot cm^2$)	R_b ($\Omega \cdot cm^2$)	R_{ct} ($\Omega \cdot cm^2$)
1-min	0.5 h	68	1177	17193	-
	7 d	38	408	4685	3326
	14 d	28	113	1469	2069
3-min	0.5 h	72	1535	28065	-
	7 d	12	469	5211	4984
	14 d	27	621	2875	2265
5-min	0.5 h	69	1853	35707	-
	7 d	68	659	7834	6929
	14 d	30	689	3258	3041
8-min	0.5 h	80	1331	20829	-
	7 d	35	542	5048	3988
	14 d	66	430	2264	2617

The corresponding EIS data are presented in Table 4.8. The charge transfer resistance (R_{ct}) of all the coatings was higher than the corresponding value of R_{po} and R_b, irrespective of the immersion time. This indicates that the interface layer between the barrier layer (dense layer [107]) and the substrate is primarily responsible for protecting the Mg alloy from corrosion during the immersion duration of 14 days.

It can be observed from Table 4 that, the R_b values are quite high during the initial immersion time and significantly decrease after 0.5 h immersion. This suggests no diffusion of electrolyte through the pores within the short immersion period. The value of R_{ct} for all the samples, irrespective of the oxidation time at which they were produced, showed a decrease with increasing immersion time. A steep decrease in the R_{ct} value over the immersion time from 0.5 hour to 14 days suggests that the corrosive SBF initially penetrates the porous layer through the micropores, reaching the barrier

layer and finally reacting with the Mg substrate, thus causing the MAO coated samples to degrade rapidly. The samples produced at 5 min have the highest R_{ct} value, which indicates that it provides the most resistance to corrosion among these samples.

4.3.2.4 Effect of Electrolyte Concentration

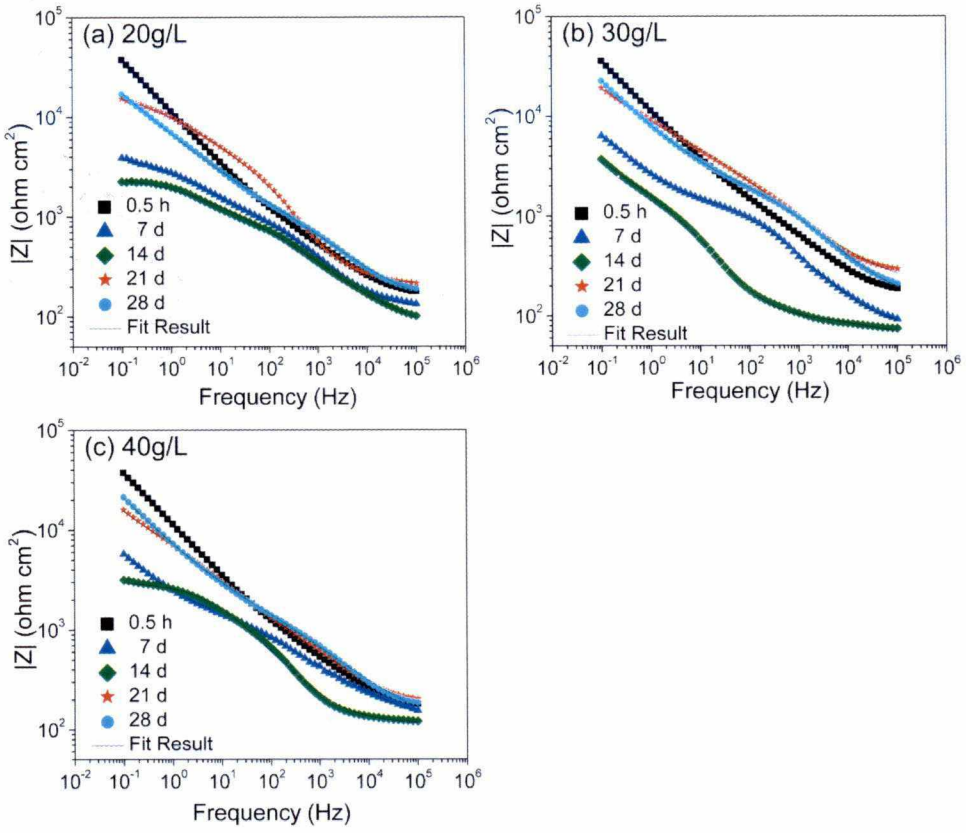

Figure 4.16 Bode plots of MAO coatings produced at various electrolyte concentrations (28 d immersion).

Table 4.9 EIS data for MAO coatings produced at various electrolyte concentrations.

Sample	Immersion time	R_s (Ω cm^2)	R_{po} (Ω cm^2)	R_b (Ω cm^2)	R_{ct} (Ω cm^2)
20g/L	0.5 h	128	3008	8999	
	7 d	26	115	347	3926
	14 d	11	95	256	2265
	21 d	215	1106	3619	15280
	28 d	122	1294	3853	17220
30g/L	0.5 h	36	3215	9044	
	7 d	68	156	459	6425
	14 d	30	119	351	3730
	21 d	177	1811	4832	19050
	28 d	122	1847	5240	22930
40g/L	0.5 h	119	2953	8860	
	7 d	39	161	394	5760
	14 d	26	12	337	3155
	21 d	118	1387	4160	15970
	28 d	98	1617	4850	21390

The Bode plots of the samples after immersion in the SBF for a period of 28 days are presented in Figure 4.16. These samples were produced at various electrolyte concentrations. From the EIS data presented in Table 4.9, after immersion of the sample for a period of 0.5 hour, the samples produced at 30g/L of electrolyte concentration show the higher R_b value. The R_{ct} value shows a decrease with increasing immersion time till 14 d, irrespective of the electrolyte concentrations. The R_{ct} value increases after 14 days till the end of the test. The increase in the R_{ct} value from day 14 to day 28 suggests that the corrosion product layer (passive layer) deposited on the surface of the samples inhibits the corrosive SBF from contacting with the substrate. The passive layer causes the MAO coated samples to degrade slowly and keep a steady level till the end of the 28th day. The sample produced at the

electrolyte concentration of 30 g/L has a higher R_{ct} value than the 20g/L and 40g/L samples, irrespective of immersion time, thus indicates that the 30g/L sample has the best resistance to corrosion.

4.4 Post-corrosion Surface Characterization

The changes in the surface micro morphology of a sample were observed by an Olympus BX60 optical microscope and SEM after the immersion of the samples for various durations. The changes in the surface macrograph were recorded by a digital camera at the end of the corrosion tests to evaluate the extent of the corrosion damage.

A PanAlytical Axios dispersive X-Ray Fluorescence (XRF) instrument was used for analysis of the quantitative element concentration of the corroded samples. The compositions of the corrosion products were determined by the X-ray diffraction (XRD) method using an X'Pert PRO diffractometer.

4.4.1 Macroscopic Appearance

In this section, the effects of the MAO control parameters (pulse frequency, applied voltage, electrolyte concentration and the oxidation time) on the macroscopic appearances after immersion in the SBF for various durations are presented. The macroscopic appearances were obtained at the end of each immersion test.

4.4.1.1 Effect of Pulse Frequency

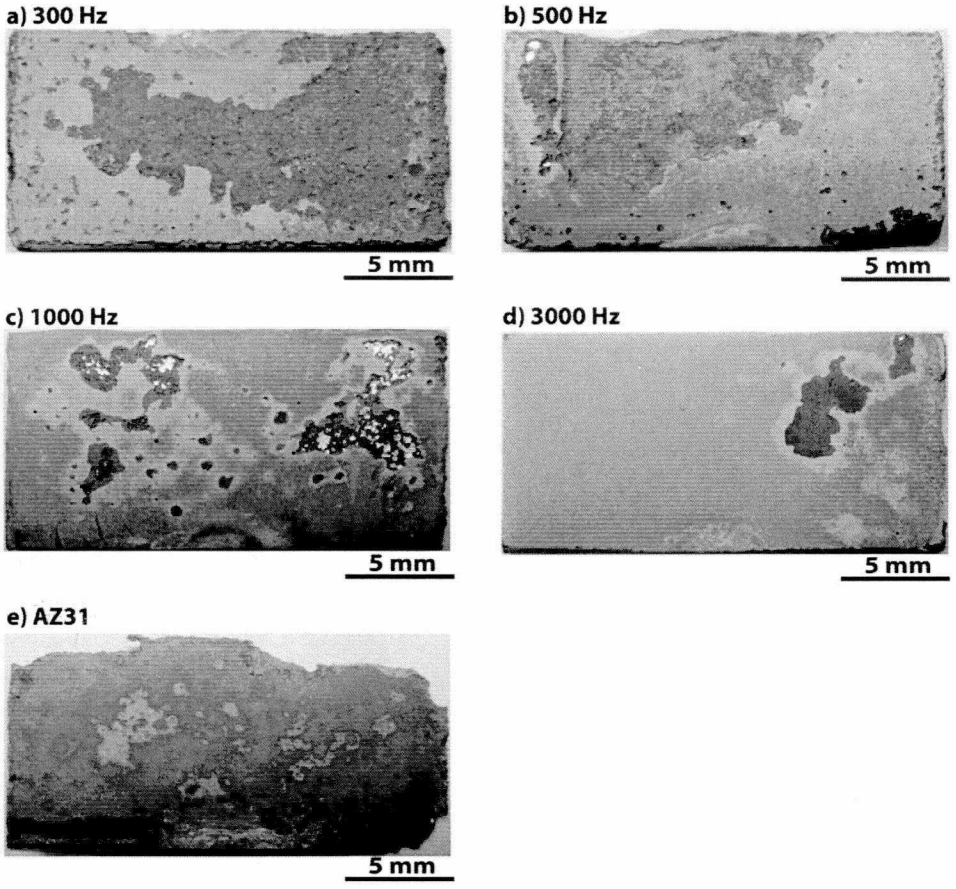

Figure 4.17 Sample appearance of uncoated AZ31 alloy and MAO coatings produced at various pulse frequencies (7 d immersion): (a) 300 Hz, (b) 500 Hz, (c) 1000 Hz, (d) 3000 Hz and (e) AZ31 alloy.

The surface appearances of the uncoated AZ31 alloy and the MAO coatings produced at various pulse frequencies after immersion in the SBF for 7 days are shown in Figure 4.17. It can be clearly seen that the extent of corrosion damage is significantly reduced for MAO coating (Figure 4.17a-d) as compared to uncoated AZ31 Mg alloy (Figure 4.17e). The corroded surface of the MAO coating produced at 3000 Hz is much smoother with few local corrosion pits except on the top right of the sample.

The 300 Hz sample has the most local pits and shows delamination. Therefore, it can be concluded that the MAO coating produced at 3000 Hz is more corrosion resistant than those produced at 300 Hz, 500Hz and1000Hz respectively.

4.4.1.2 Effect of Applied Voltage

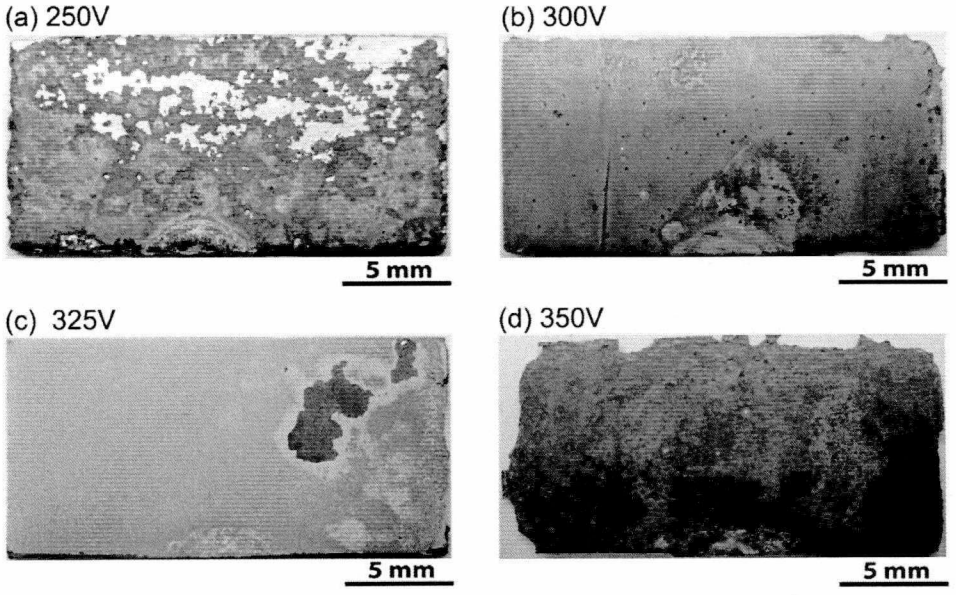

Figure 4.18 Sample appearance of MAO coatings produced at various applied voltages (7 d immersion): (a) 250 V, (b) 300 V, (c) 325 V and (d) 350 V.

The surface appearances of the MAO coatings produced at various applied voltages after immersion in the SBF for 7 days are shown in Figure 4.18. Formation of numerous precipitates on the surface of the sample produced at 250 V can be observed. In addition, the sample surface is very rough with various pits and scratch. This is due to the fact that this sample has the thinnest coating. The MAO coating produced at 350 V shows a local corrosion flaking at the edge of the sample. The MAO coating produced at 325 V displays a lesser level of delamination and flaking. Thus, it seems that the coating produced at 325V is more resistant to corrosion than

those produced at other operating conditions.

4.4.1.3 Effect of Oxidation Time

The macroscopic appearances of the MAO coatings produced for various oxidation times after immersion in the SBF for 14 days are shown in Figure 4.19. It can be observed that the extent of corrosion damage is significantly reduced with increasing oxidation time (up to 5 min). When oxidation times increase to 8 min, more local flaking occurred. The 1-min sample corroded most severely resulting in localized corrosion flake from the edges of the sample, and a large amount of deeper corrosion pits appeared on the surface. Localized edge corrosion flakes are also found in the 3-min and 8-min samples. 5-min sample has the fewest corrosion flakes and presents the best corrosion resistance.

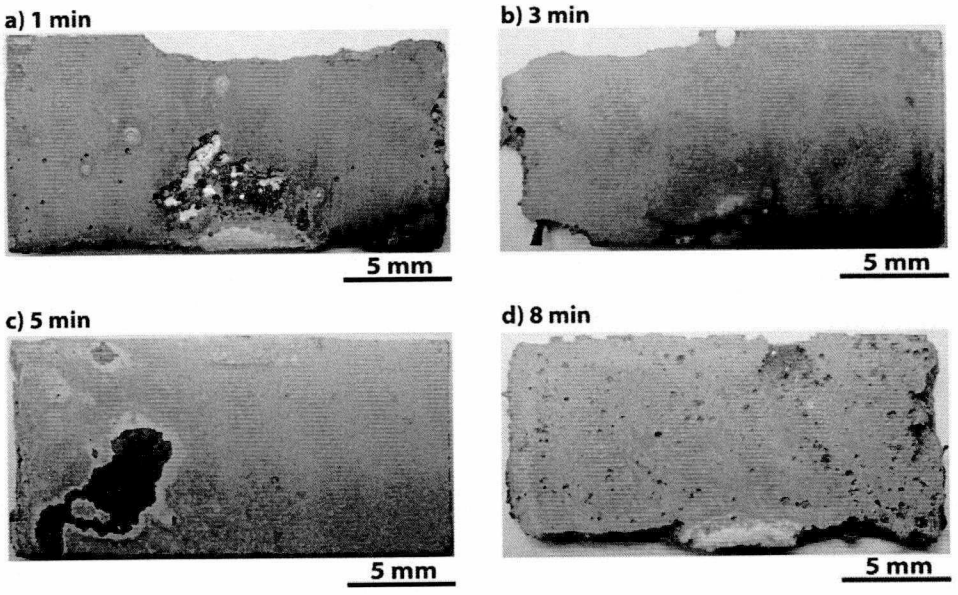

Figure 4.19 Sample appearance of MAO coatings produced at various oxidation times (14 d immersion): (a) 1 min, (b) 3 min, (c) 5 min and (d) 8 min.

4.4.1.4 Effect of Electrolyte Concentration

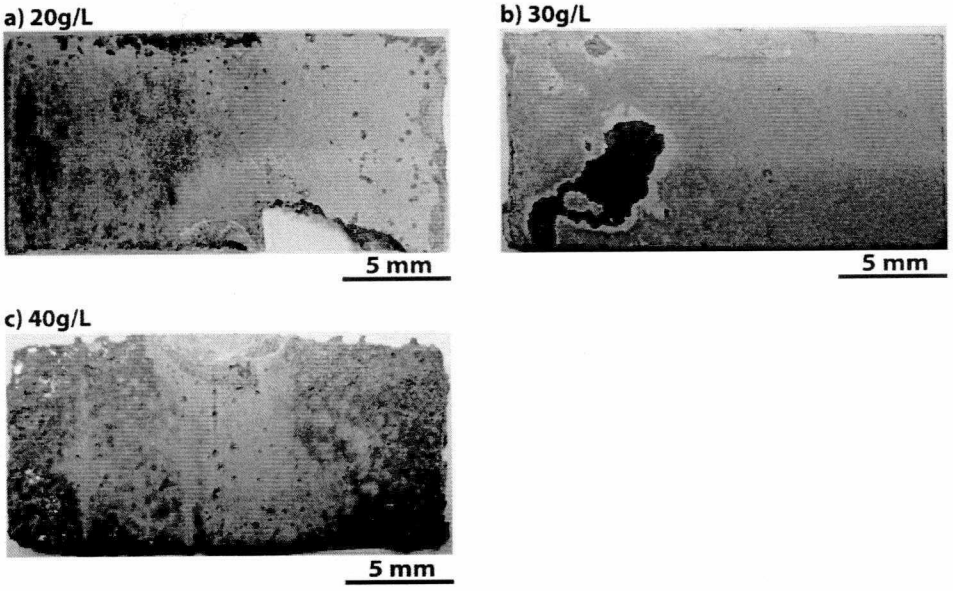

Figure 4.20 Sample appearance of MAO coatings produced at various electrolyte concentrations (28 d immersion): (a) 20 g/L, (b) 30 g/L and (c) 40 g/L.

The surface appearances of Group 4 samples after immersion in the SBF for 28 days are shown in Figure 4.20. These samples were produced at various electrolyte concentrations. The extent of the corrosion damage of the samples is less with increased electrolyte concentration to 30 g/L, while the sample produced at higher concentration (40 g/L) shows a larger extent of damage. The 20 g/L sample corroded most severely from localized corrosion flaking at the edges of the sample, and a large deeper corrosion pit formed on the surface. The localized flaking is also found in the 40g/L sample. The coating produced at 30g/L has the fewest corrosion flakes, thus provides the best resistance to corrosion.

4.4.2 Surface Micrographs

In this section, the effects of the MAO control parameters (pulse frequency, applied

voltage, electrolyte concentration and the oxidation time) on the surface micrographs after immersion in the SBF for various durations are presented.

4.4.2.1 Effect of Pulse Frequency

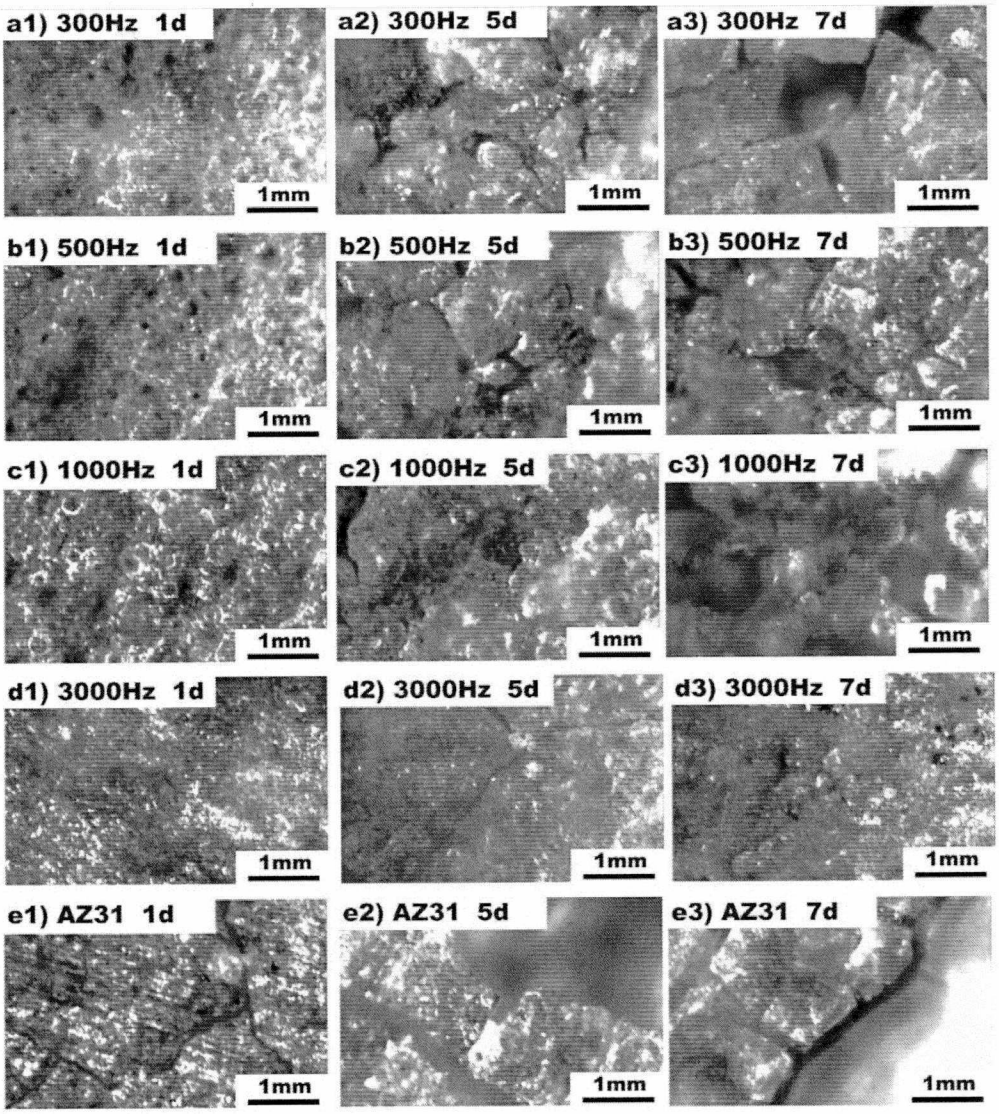

Figure 4.21 Surface micrographs of uncoated AZ31 alloy and MAO coatings produced at various pulse frequencies (7 d immersion).

The optical surface micrographs of the samples (Figure 4.21) were taken after immersion in the SBF for 7 days. The micrographs show the differences in the extent

of damage due to corrosion of the uncoated AZ31 alloy and the MAO coatings. The MAO coating (Figure 4.21a-d) enhances the resistance to corrosion of the AZ31 alloy (Figure 4.21e). For each specimen, increasing immersion time results in larger extent of corrosion with more fractures, cracks, holes and pits. As it can be observed, at day 1, the surfaces of all the coated samples are full of numerous small pinholes. As the reaction proceeds, cracks, fractures and pits are formed gradually. After 5-days immersion, more cracks can be observed in the 300Hz specimen (Figure 4.21a2) compared to the other coated specimens. At the end of 7-day immersion, severe fractures and deep large pits are formed in the 300Hz and the 500Hz specimens (Figures 4.21a3-b3). Overall, the 3000 Hz samples (Figures 4.21 d1-d3) show relatively uniform micrographs with fewer fractures and shallower corrosion pits, thus, endowing the AZ31 alloy with greatly enhanced resistance to corrosion. The micrographs presented above correlate very well with the Tafel and EIS results.

4.4.2.2 Effect of Applied Voltage

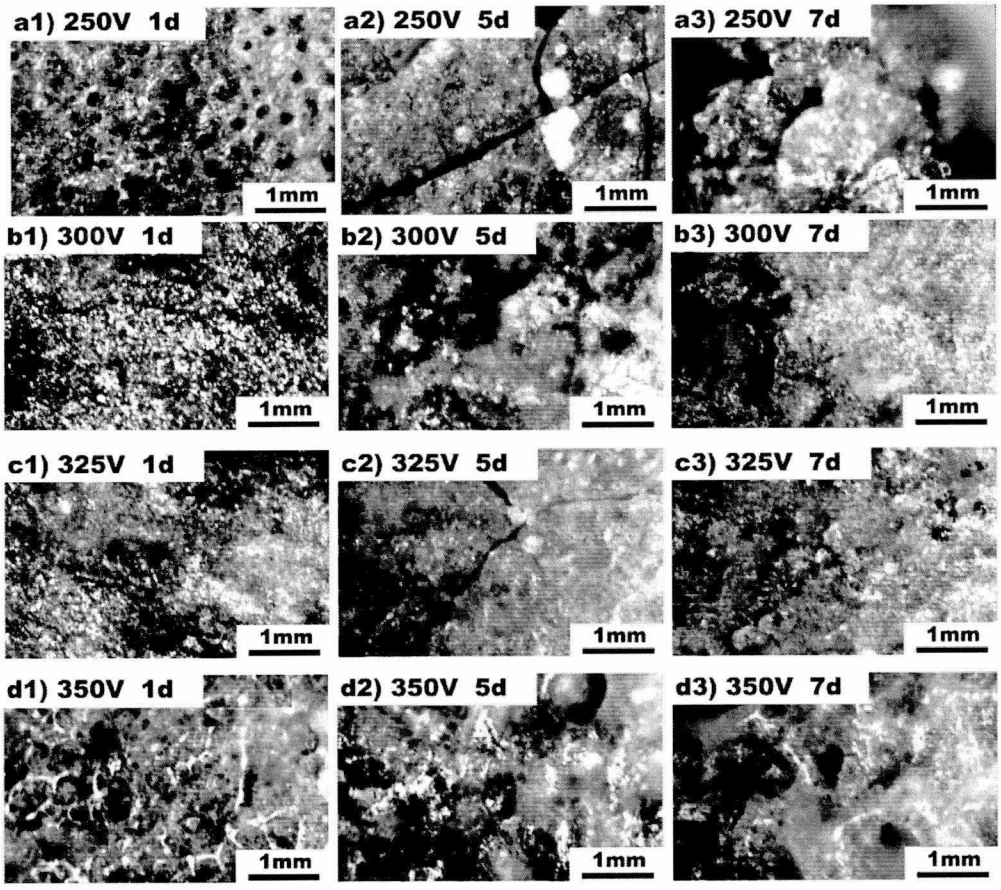

Figure 4.22 Surface micrographs of MAO coatings produced at various applied voltages (7 d immersion).

The optical surface micrographs of the Group 2 samples after 7 days immersion are shown in Figure 4.22. Group 2 samples were produced at various applied voltages. The micrographs show the extent of damages due to corrosion on the MAO coating produced at various voltages. Due to corrosion, a few deeper pits and longer cracks can be observed on the surface of the samples produced at 250 V (Figure 4.22a). The samples produced at 350 V displayed numerous deeper pits than that can be observed on samples produced at 300V and 325V. A relatively uniform surface with fewer

cracks and pits is observed on the 325V samples, thus endowing the AZ31 alloy with greatly enhanced resistance to corrosion. Among the four samples, the samples produced at 325 V exhibit the best resistance to corrosion. The observation from the micrographs correlates very well with the Tafel and EIS results.

4.4.2.3 Effect of Oxidation Time

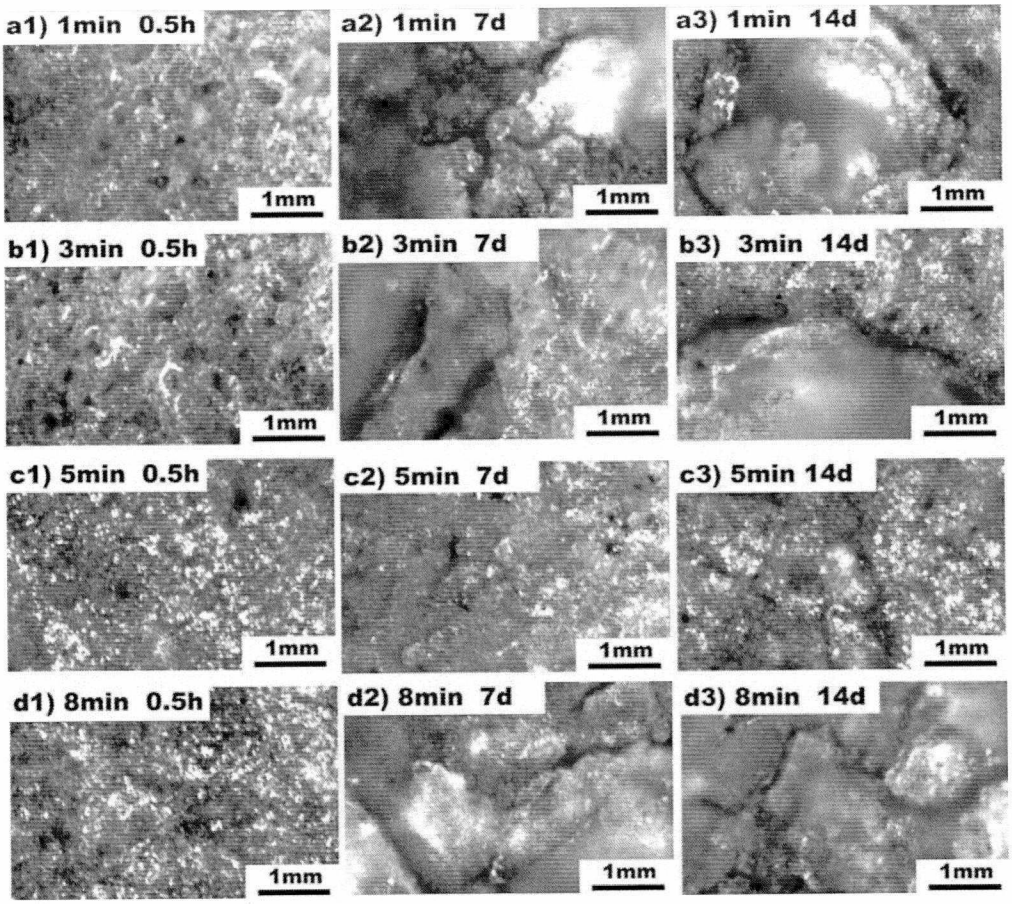

Figure 4.23 Surface micrographs of MAO coatings produced at various oxidation times (14 d immersion).

The optical surface micrographs of the MAO coatings after immersion in the SBF for a duration of 14 days are shown in Figure 4.23. The micrographs show the extents in the corrosion damage on the MAO coatings produced at various oxidation times. For

the 0.5 h immersion, the images exhibit a typical porous microstructure without any fractures. After a 7-d immersion (Figures 4.23 a2, b2 and c2), it can be clearly observed that more fractures, cracks and pits have formed on the surface of all the samples. A 5-min sample shows fewer fractures, smaller pits and cracks, thus endowing the AZ31 alloy with greatly enhanced resistance to corrosion. When the immersion time increased to 14 days, the corrosion produced larger fractures, cracks and deeper pits. The MAO coating produced at an oxidation time of 5 min provides the best resistance to corrosion. The observation from the micrographs correlates very well with the Tafel and EIS results.

4.4.2.4 Effect of Electrolyte Concentration

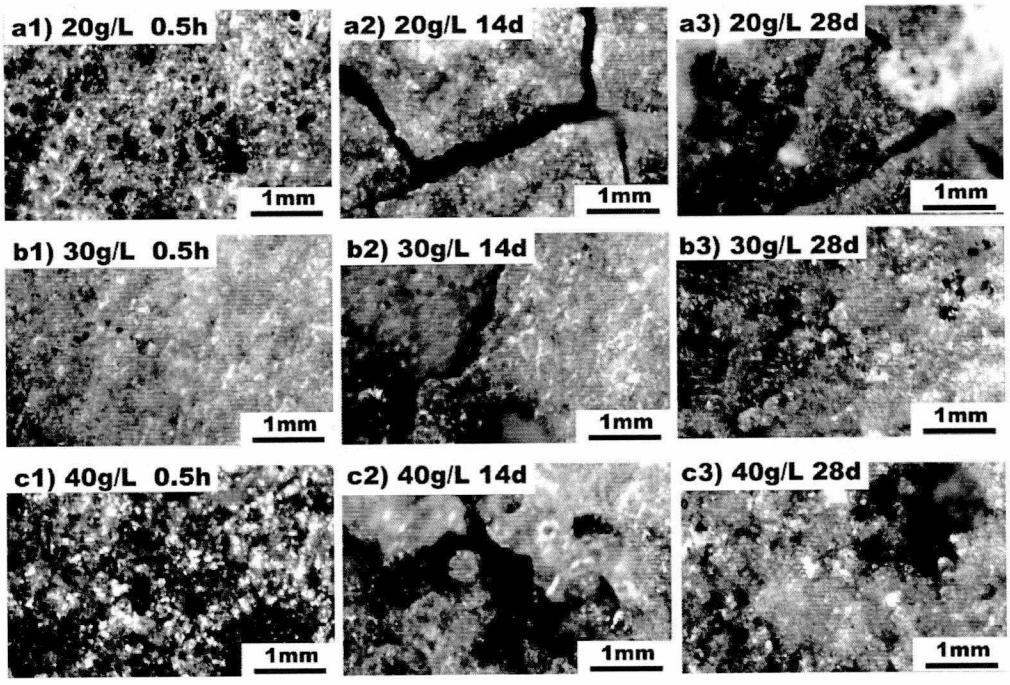

Figure 4.24 Surface micrographs of MAO coatings produced at various electrolyte concentrations (28 d immersion).

The optical surface micrographs of the samples after immersion in the SBF for a

duration of 28 days are shown in Figure 4.24. These samples were produced at various electrolyte concentrations. Absence of cracks and fractures can be observed after an initial immersion of 0.5 h. The corrosion damage level of the samples continues to increase after 14−day immersion. The extent of damage is the highest for each coated sample with numerous fractures, cracks and pits. However, with immersion time extended to 28 days, smaller fractures, cracks and pits can be observed on the ample surface. The sample coated at 30 g/L shows relatively fewer fractures, smaller pits and cracks, thus, endowing the AZ31 alloy with greatly enhanced resistance to corrosion. The observation from the micrographs correlates very well with the Tafel and EIS results.

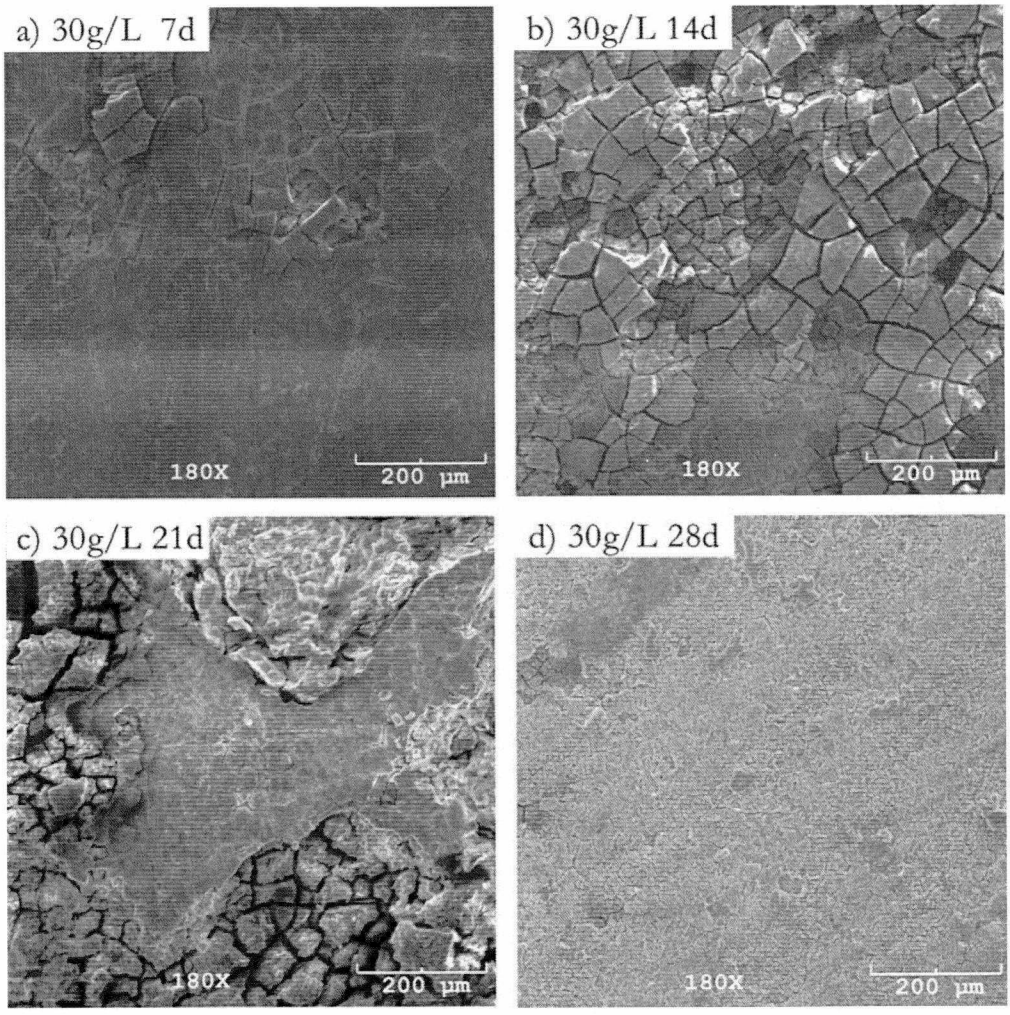

Figure 4. 25 Low-magnification (180 X) SEM images of MAO-coated AZ31 alloy produced at 30g/L after immersion in SBF for: (a) 7 d, (b) 14 d, (c) 21 d and (d) 28 d.

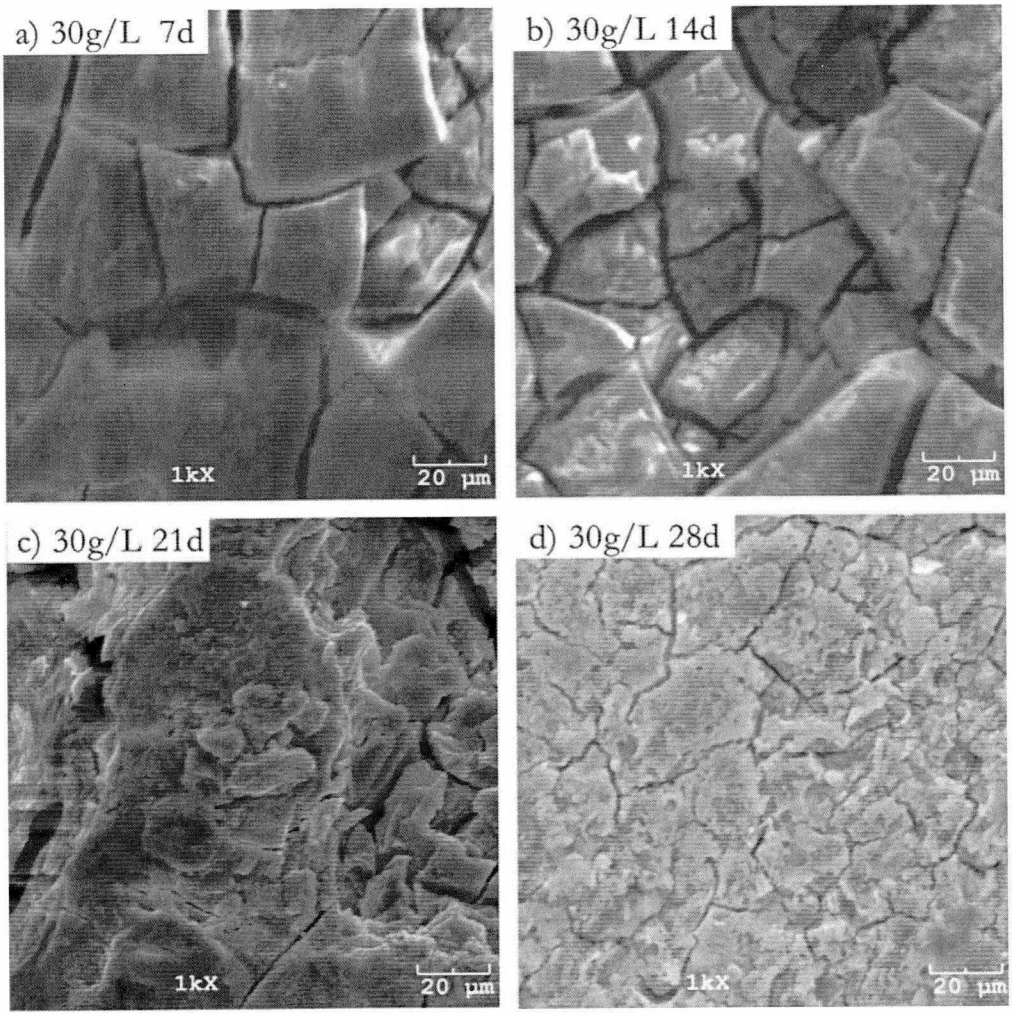

Figure 4. 26 High-magnification (1000 X) SEM images of MAO-coated AZ31 alloy produced at 30g/L after immersion in SBF for: (a) 7 d, (b) 14 d, (c) 21 d and (d) 28 d.

The SEM morphologies of the 30g/L sample after immersion in the SBF for various durations are shown in Figures 4.25 and 4.26. The morphologies show the differences in the extent of corrosion damages of the MAO coatings after various immersion durations. From the images produced at low magnification, shown in Figure 4.25, it can be observed that for the 7 days of immersion, cracks and pits due to corrosion are formed. With an immersion time of 14 days, larger fractures, cracks and deeper pits can be observed. The level of corrosion damage on the samples after 14–day

immersion is significant. After 21 days immersion, it can be clearly observed that the sample surface is partially coated with a corrosion product layer (Figure 4.25c). This corrosion product layer reduces further damage due to corrosion. At the end of 28 days immersion, the formation of the corrosion product layer on the sample surface is complete (Figure 4.25d). From the SEM images at high magnification, shown in Figure 4.26, it can be seen that the number, size of the fractures increase as a function of immersion time from 7 to 14 days. However, after 21 days immersion, the fractures are partially filled with the corrosion products. At the end of the 28days immersion, the entire surface is smoother with few smaller cracks.

4.4.3 XRD Analysis after Corrosion

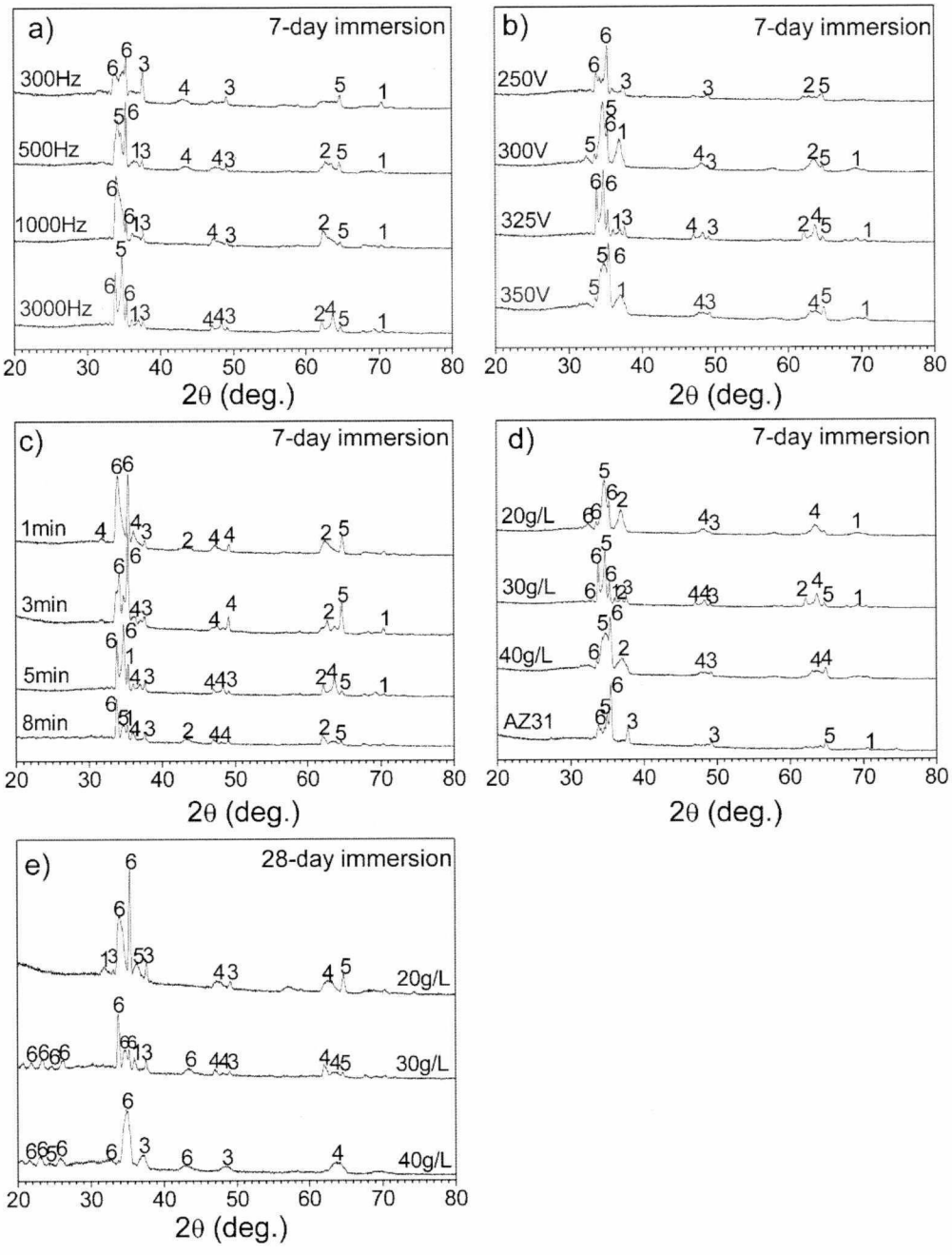

Figure 4.27 XRD spectra of MAO coatings produced at various (a) pulse frequency (b) applied voltage (c) oxidation time and (d-e) electrolyte concentration. (1) Mg; (2) MgO; (3) $Mg(OH)_2$ (brucite); (4) $Mg_3(PO_4)_2$; (5) $Mg_4Al_2(CO_3)(OH)_{12} \cdot 3H_2O$ (Quintinite); (6) $Ca_{10}(PO_4)_6(OH)_2$ (Hydroxyapatite).

The XRD spectra of the MAO coatings produced at various control parameters are shown in Figure 4.27. It can be seen that the MAO control parameters has negligible effect on the phase composition of the corroded surface. The corroded surface of the uncoated AZ31 alloy is composed of Mg, brucite -$Mg(OH)_2$, quintinite and hydroxyapatite (HA)-$Ca_{10}(PO_4)_6(OH)_2$. The magnesium is from the substrate. Brucite, quintinite and hydroxyapatite, however, are the corrosion products. For the MAO coatings, the corroded surface is comprised of MgO and $Mg_3(PO_4)_2$, in addition to Mg, brucite, quintinite and hydroxyapatite. The magnesium oxide and the $Mg_3(PO_4)_2$ are constituents of the MAO coating. The magnesium oxide peaks are weak and are only found at approximately 62.3 degree. This is due to the conversion of MgO to $Mg(OH)_2$ phase. It can be observed from the XRD patterns that the main phase composition of the samples after a total of 28−day immersion (Figure 4.27e) is similar to that of the samples after 7 days immersion (Figure 4.27b). The components of Mg and MgO phases are not detected after 28 days immersion due to the conversion of MgO to $Mg(OH)_2$ phase. The difference in the peaks of the biocompatible hydroxyapatite is evident at 20−30° for the 30g/L and the 40g/L samples.

The products of corrosion such as $Mg(OH)_2$, quintinite and hydroxyapatite are generated in the SBF due to the following reactions:

$$Mg + 2H_2O = Mg(OH)_2 + H_2\uparrow$$

$$MgO + H_2O = Mg(OH)_2$$

$$4Mg^{2+} + 2Al^{3+} + HCO_3^- + 13OH^- + 2H_2O \rightarrow Mg_4Al_2(CO_3)(OH)_{12}\cdot 3H_2O$$

$$10Ca^{2+} + 6PO_4^{3-} + 2OH^{-1} = Ca_{10}(PO_4)_6(OH)_2$$

4.4.4 XRF Analysis after Corrosion

In order to determine the Ca/P ratio in the HA on the corroded samples, a XRF analysis was conducted. An example of the dispersive XRF spectrum of the MAO coated AZ31 alloy after 14-day SBF immersion is shown in Figure 4.28. A Ca/P ratio of 1.67 is generally accepted for good biocompatibility and bioactivity [108-111]. The Ca/P ratios in the MAO coated samples are presented in Table 5. It can be seen that the ratio of Ca/P in the HA ranges from 1.58 to 1.65, which is slightly lower than 1.67. This may be due to the fact that one part of the phosphorous in the coated samples comes from the coating constituent $Mg_3(PO_4)_2$. Based on the generally accepted ratio (1.67), it seems that the HA formed on the corroded samples is an acceptable biocompatible and bioactive supplement/implant.

Table 4.10 The Ca/P ratio in the MAO coated samples determined by XRF.

Samples	1-min	3-min	5-min	8-min
Ca/P ratio	1.58	1.62	1.65	1.63
Samples	20g/L	30g/L	40g/L	
Ca/P ratio	1.63	1.65	1.64	

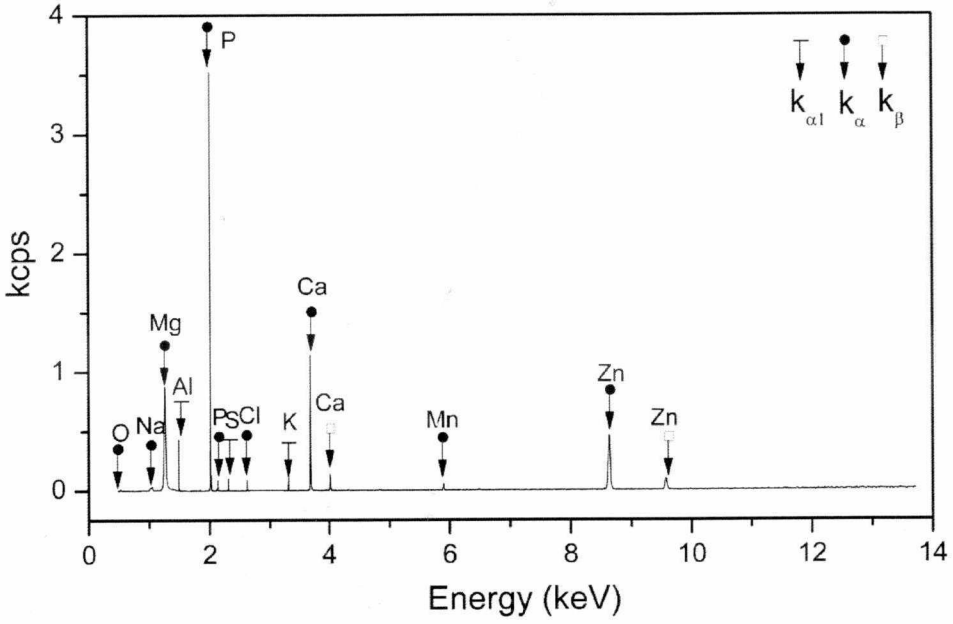

Figure 4.28 An example of dispersive XRF spectrum of MAO coating produced at 3000 Hz after 7-day immersion in the SBF.

Chapter 5: Modeling of Long-term Corrosion Rate and Corrosion Mechanism

The effects of the long-term immersion on the corrosion behavior of the MAO-coated Mg alloys produced at various electrolyte concentrations are discussed in Chapter 4. In this chapter, a predictive model for the long-term corrosion rate and a model for long-term corrosion behavior are presented.

5.1 Predictive Model of Corrosion Current Density and PCA

A regression equation based on the calculated corrosion rate and the selected variables is developed to model the long-term corrosion rate. The regression equations between the corrosion rate as a function of applied voltage, oxidation time and electrolyte concentration are third-order polynomials. The equations are, however, second-order polynomials for the pulse frequency and the immersion time. Based on the regression equations, the proposed mathematical model for the corrosion rate is:

$$Y= (ax_1^3+bx_1^2+cx_1)+(dx_2^2+ex_2)+(fx_3^2+gx_3)+(hx_4^2+ix_4)+ (jx_5^4+kx_5^3+lx_5^2+mx_5)+n \quad \text{Equation 12}$$

Where, Y represents the corrosion rate. The variables x_1, x_2, x_3, x_4 and x_5 denote the pulse frequency, applied voltage, oxidation time, electrolyte concentration and the immersion time, respectively. The raw (measured) data for non-linear multi-variable regression for corrosion rate are presented in Appendix C. The constants a, b, c, d, e, f, g, h, i, j, k, l, m and n are the regression coefficients, and the values of these coefficients are obtained by least squares regression. The coefficient values of the predictive model are shown in Table 5.1.

Table 5.1 The regression coefficients for the predictive model of corrosion rate

a	b	c	d	e
-4.80E-11	2.24E-07	-2.75E-04	4.47E-06	-2.86E-03
f	g	h	i	j
3.89E-07	-2.12E-04	1.36E-04	-8.98E-03	2.49E-09
k	l	m	n	
-7.87E-07	8.48E-05	-3.33E-03	7.99E-01	

For a comparison, the measured and the simulated corrosion rates are presented in Figure 5.1. The coefficient of multiple determination (R^2=0.9021) is very high, thus, suggesting that the predictive model accurately reflects the measured data. The predictive model for the corrosion rate is written in Visual Basic programming language. The program panel is shown in Figure 5.2 and the entire program code is listed in appendix B.

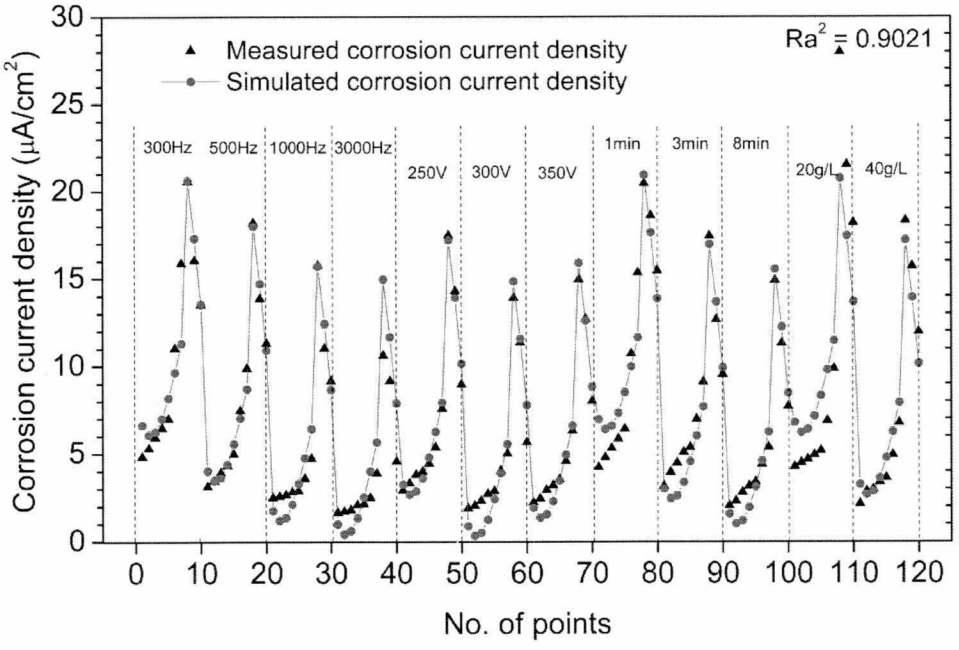

Figure 5.1 The model plot of measured and simulated corrosion current density of MAO-coated AZ31 Mg alloys.

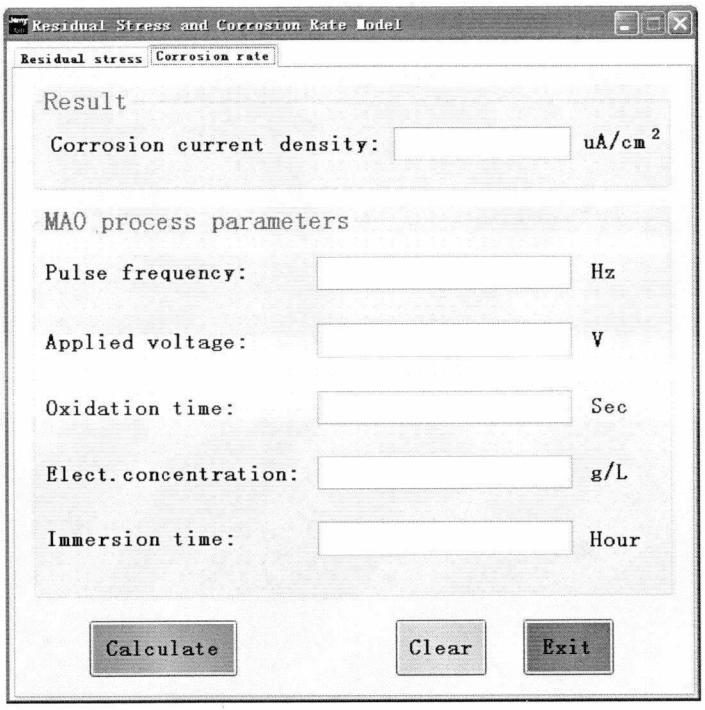

Figure 5.2 Executable program panel to predict the corrosion rate.

In order to identify any underlying patterns in the data, and to identify the contribution of each of the control parameters, a principal components analysis (PCA) was conducted. The results of the PCA are shown in Tables 5.2 and 5.3. It can be seen that the ranked eigenvalue of pulse frequency, one of the control parameters, is the highest (1.126). Together with the Tafel, EIS, post-test surface analysis and the PCA, it can be concluded that pulse frequency is the dominant factor towards resistance to corrosion.

Table 5.2 Eigenvector of five parameters for the modeling of corrosion rates.

	Pulse frequency	Applied voltage	Oxidation time	Electrolyte concentration	Immersion time
Pulse frequency	0.737	-0.128	0.000	0.000	0.664
Applied voltage	-0.629	-0.489	0.000	0.000	0.604
Oxidation time	-0.248	0.863	0.000	0.000	0.441
Electrolyte concentration	0.000	0.000	1.000	-0.021	0.000
Immersion time	0.000	0.000	0.021	1.000	0.000

Table 5.3 Eigenvalues of the eigenvector shown in Table 5.2.

	Pulse frequency	Applied voltage	Oxidation time	Electrolyte concentration	Immersion time
Eigenvalue	1.126	1.030	1.000	1.000	0.844
Variability (%)	22.514	20.609	20.000	20.000	16.877
Cumulative (%)	22.514	43.123	63.123	83.123	100.000

5.2 Modeling of Corrosion Mechanism

Long-term immersion test was conducted for the MAO-coated AZ31 alloy produced at various electrolyte concentrations. The Tafel and EIS results, the post-test specimen surface and microstructural analysis have been discussed earlier. Based on those results and general corrosion principle, a schematic diagram of the corrosion process in SBF of MAO-coated AZ31 alloy is presented in Figure 5.3.

The coating produced on the AZ31 alloy is composed of two layers [112]: a 5~10 μm outer porous layer and a dense inner layer. It may be seen from Figure 5.3 a, the outer porous layer has several large-sized, deep pores or cavities. Some pores start from the outermost surface while the other exists within this layer. The underneath layer is denser with fewer micropores.

When the MAO coated sample was immersed into the SBF, the MgO constituent on the outermost surface starts to react with the corrosive solution and converts to $Mg(OH)_2$ (Figure 5.3 b). The amount of this corrosion product is not significantly large at the initial immersion due to the smaller amount of MgO than the magnesium in the substrate.

In addition to the deposit of $Mg(OH)_2$, the hydroxyapatite is found on the surface of the samples (Figure 5.3b). Understanding of the precipitation of hydroxyapatite is extremely important for MAO coated Mg alloys in biomedical applications. This hydroxyapatite is the implant material due to its excellent biocompatibility and bioactivity [113]. The formation of the hydroxyapatite in the SBF is self-generated after a certain length of immersion [59]. It has been reported that if a material is able to have 'apatite' formed on its surface in SBF, when implanted, the 'apatite' produced on its surface in the living body, and will bond to living bone through this apatite layer[59]. The hydroxyapatite has been observed to be formed on the MAO coatings after immersion in the SBF. Thus, if the MAO coated Mg alloy is implanted to the human body, the hydroxyapatite would be produced in the living body and will bond to the living bone. Therefore, the SBF solution takes significant effect on the corrosion behavior of MAO coated Mg alloys. The SBF would be very useful to predict the in-vivo bioactivity for the MAO coatings on the Mg alloys for biomedical applications.

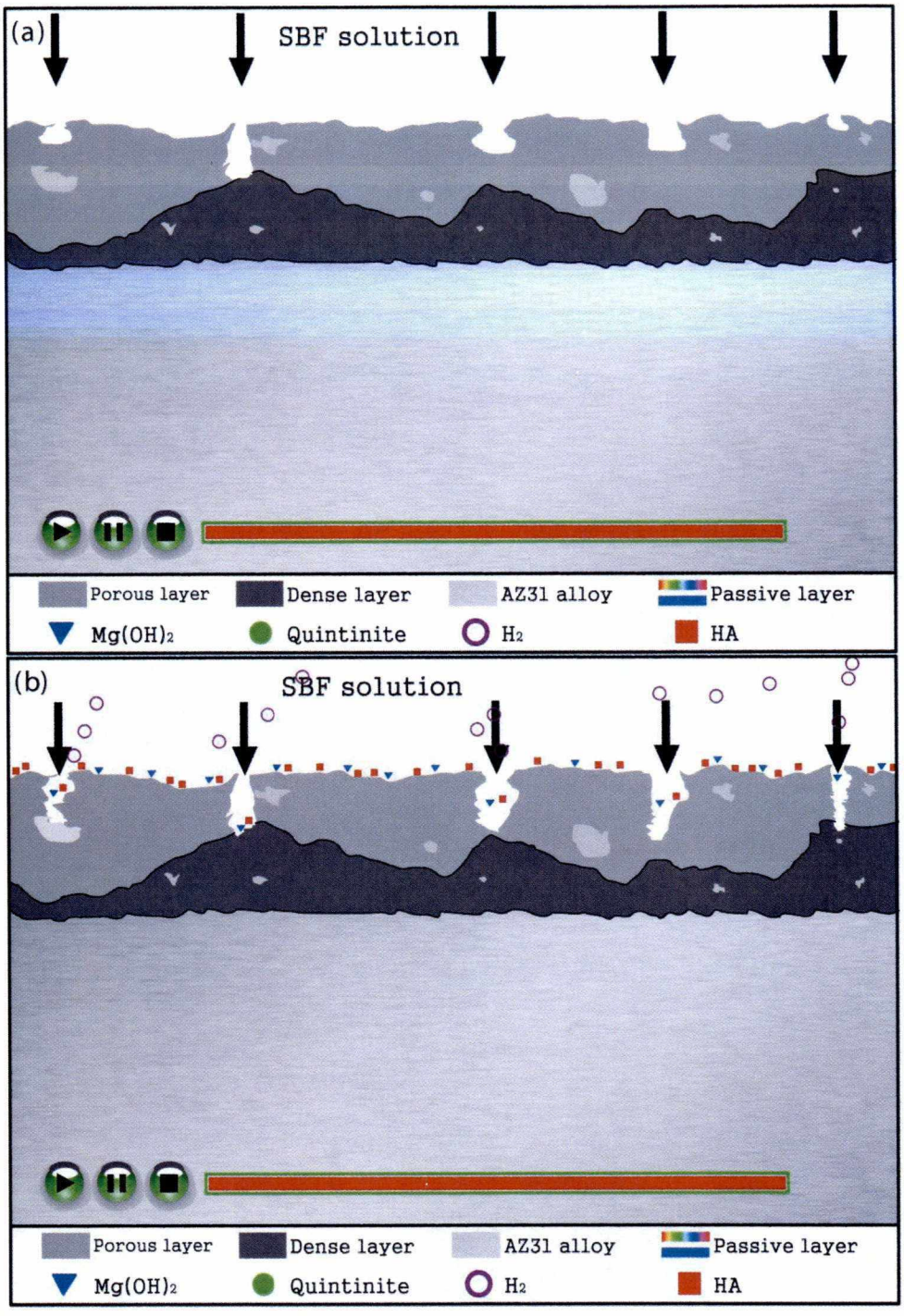
(a)
SBF solution
Porous layer
Dense layer
AZ31 alloy
Passive layer
Mg(OH)2
Quintinite
H2
HA
(b)
SBF solution
Porous layer
Dense layer
AZ31 alloy
Passive layer
Mg(OH)2
Quintinite
H2
HA

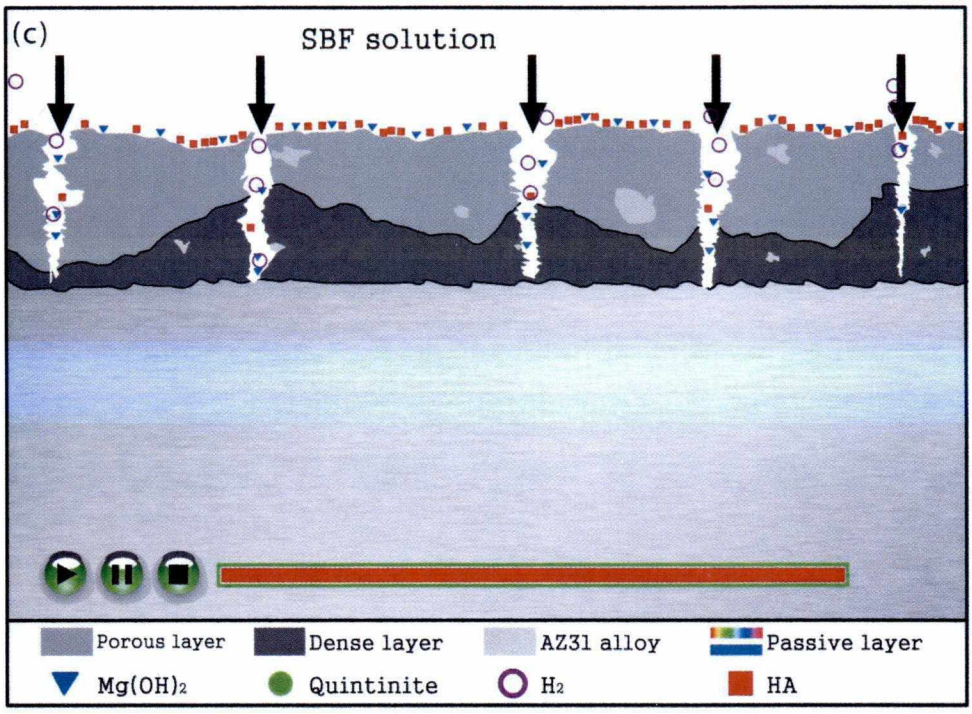
(c)
SBF solution
Porous layer
Dense layer
AZ31 alloy
Passive layer
Mg(OH)2
Quintinite
H2
HA

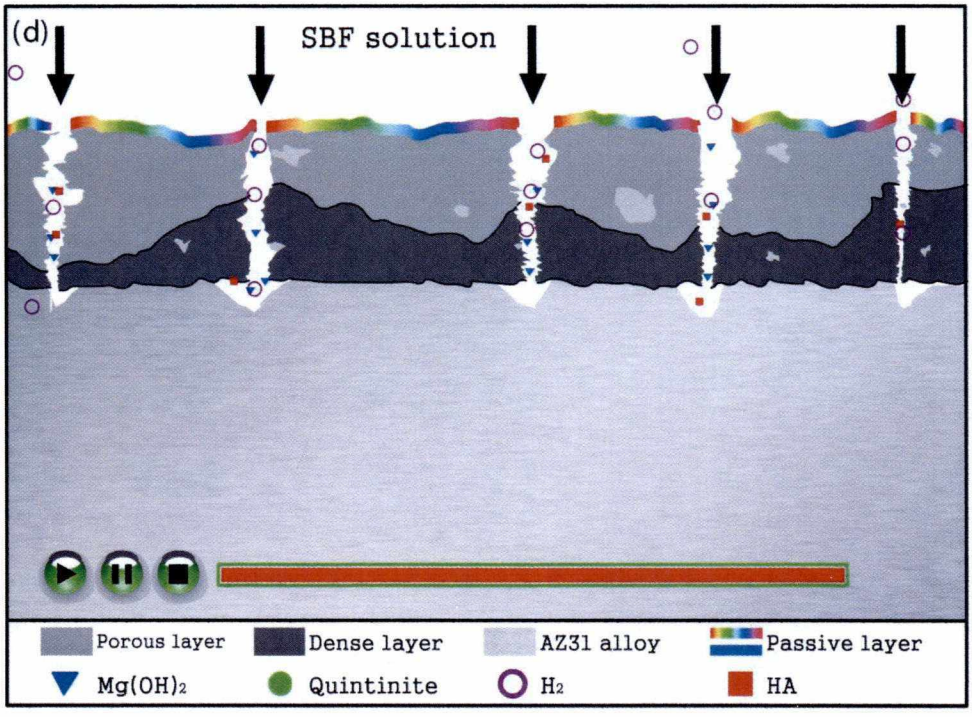
(d)
SBF solution
Porous layer
Dense layer
AZ31 alloy
Passive layer
Mg(OH)2
Quintinite
H2
HA

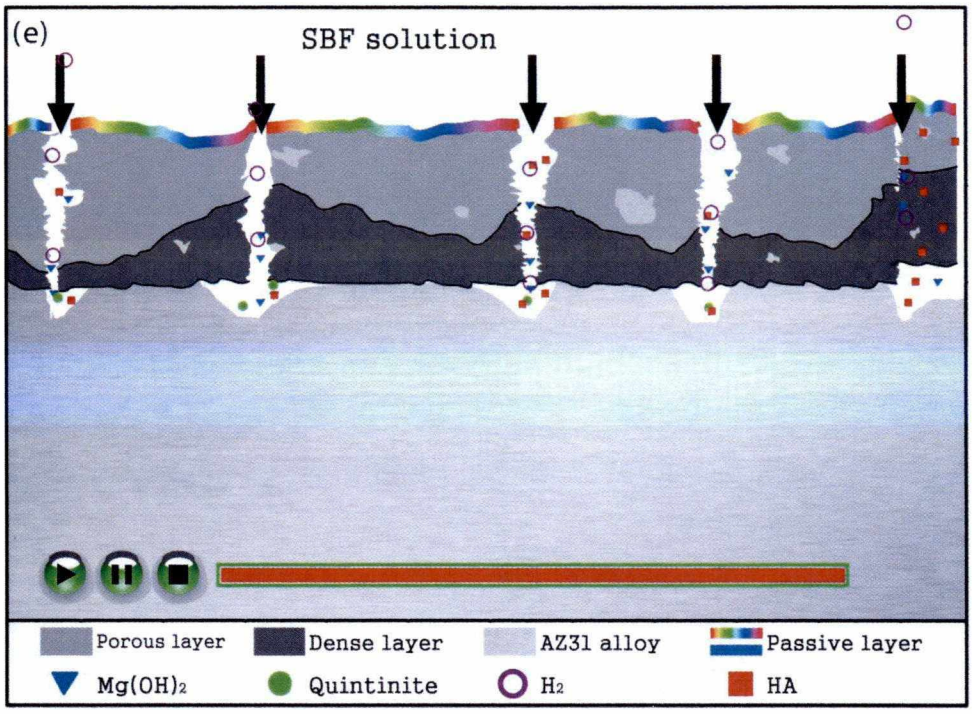
(e)
SBF solution
Porous layer
Dense layer
AZ31 alloy
Passive layer
Mg(OH)2
Quintinite
H2
HA

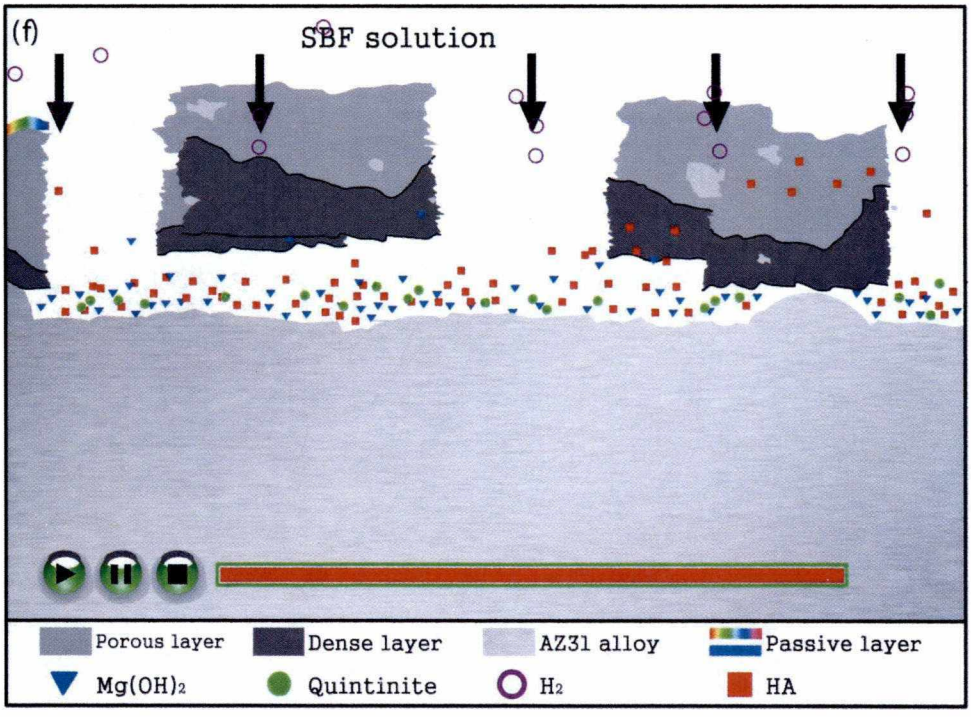
(f)
SBF solution
Porous layer
Dense layer
AZ31 alloy
Passive layer
Mg(OH)2
Quintinite
H2
HA

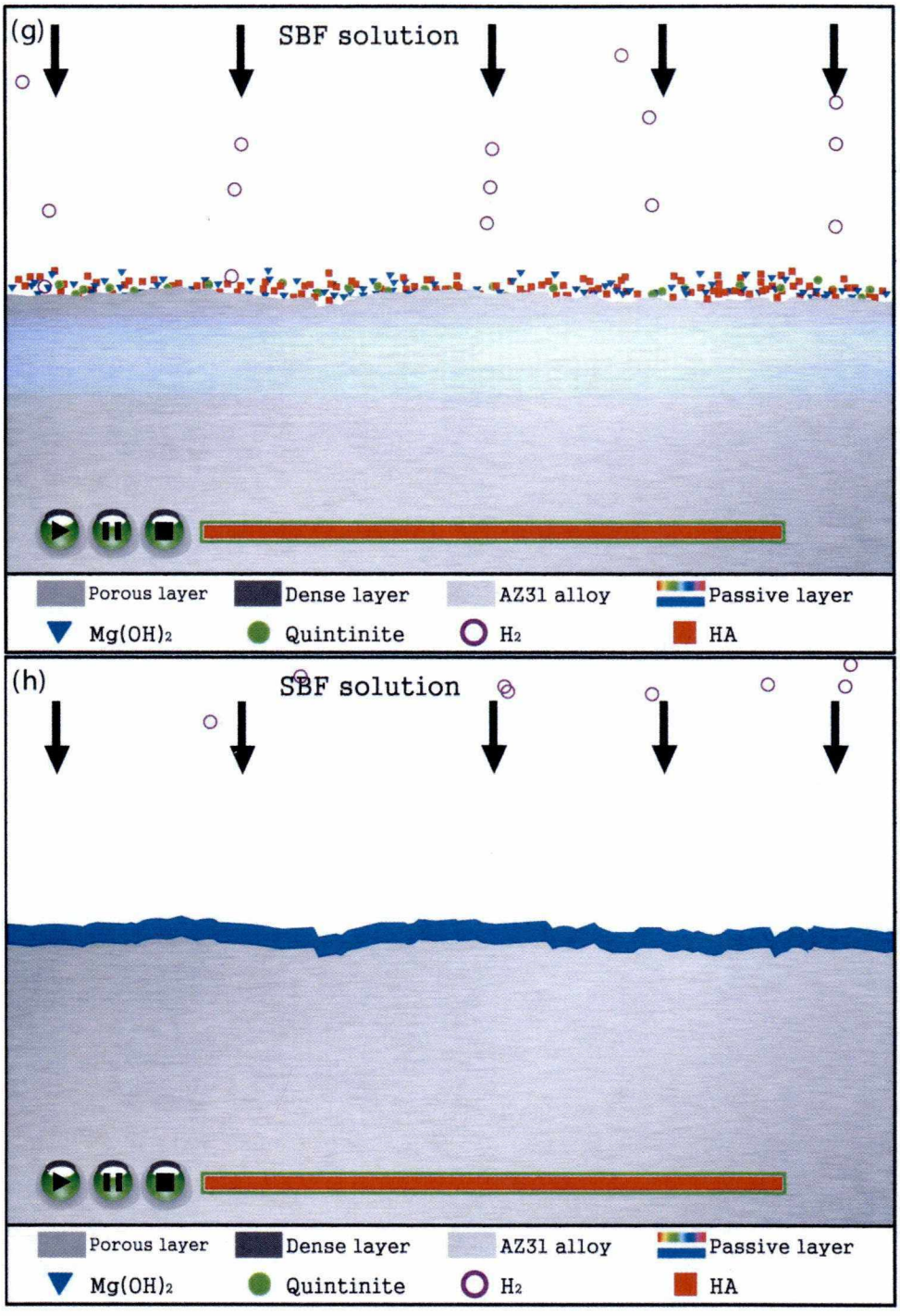

Figure 5.3 Schematic diagram of the corrosion process and mechanism of MAO coated AZ31 Mg alloy after immersion in the SBF.

With the ongoing reactions, the pores in the outer layer slowly enlarge. Therefore, the solution SBF solution goes through outer layer and reaches the inner dense layer, as well as the interface between the dense layer and the AZ31 substrate (Figure 5.3 b-c).The time to penetrate from the outermost surface layer to the interface takes longer because of small micropores in the dense layer. This indicates that the protective function of the MAO coating is primarily due to the dense layer. At the same time, more and more hydroxyapatite is deposited on the outermost surface of the MAO coating, so that a corrosion product layer is formed (Figure 5.3d).

Once the corrosive SBF solution reaches the interface layer, the substrate is easily corroded. Magnesium reacts with the SBF solution, and more $Mg(OH)_2$ is produced with gas bubbles rising and a new corrosion product quintinite is formed as precipitate (Figure 5.3e). If the SBF penetrates all the pores on the coating and reaches the substrate, fast degradation occurs. With increasing the immersion time, the MAO coating layer loses the support of the substrate and detaches from the substrate (Figure 5.3 e-f). More precipitates including hydroxyapatite, brucite and quintinite are accumulated on the interface layer (Figure 5.3 g). A thin passive layer is formed on the substrate. Therefore, when the corrosion continues, this passive layer will become relatively thicker (Figure 5.3 h).

The hydroxyapatite, however, would behave differently since hydroxyapatite will bond to the living bone. The detached MAO coating layer and the precipitate layer may lead to several unexpected side effects. Further research is warranted in this area including the development of a suitable MAO coating which will dissolve in the human body without any side effects.

Generally the extent of corrosion damage of MAO coated Mg alloy in the SBF depends on the size, depth and the number of micropores on the outermost surface layer of the MAO coatings, the uniformity of the coatings and the thickness of the dense layer. Additionally the corrosive simulated body fluid has a significant effect on the corrosion performance of MAO coated Mg alloy.

Chapter 6: Conclusions and Future Work

6.1 Conclusions

This research has investigated the residual stresses and the corrosion behavior of the MAO-coated AZ31 magnesium alloys in simulated body fluid for biomedical applications. It was found that the corrosion resistance of MAO-coated Mg alloys can be improved by optimizing the MAO control parameters.

The SEM images showed typical porous surface morphologies or MAO coatings. The phase of the MAO coating is primarily composed of Mg, MgO, $MgAl_2O_4$ and $Mg_3(PO_4)_2$. The post-corrosion XRD spectra indicate that brucite, quintinite and hydroxyapatite, by-products of the coating are formed on the corroded surfaces. The formation of HA indicated that simulating corrosion behavior of the samples in SBF is essential to predict the in-vivo bioactivity of MAO coated Mg alloys for biomedical applications. The ratio of Ca/P in the HA determined by the XRF technique is close to 1.67, suggesting that the HA formed on the corroded samples is an acceptable biocompatible and bioactive supplement/implant.

The residual stresses in the MAO coating are compressive and in the range of -611 to -1272 MPa. The magnitude of the residual stresses in the MAO coating are closely related to the porosity and the thickness of the coating. A relationship between the residual stresses and the porosity and thickness of the coating was developed using the Stoney equation. This equation extrapolates the influence of the MAO parameters on residual stresses.

Potentiodynamic polarization results indicates that with increasing immersion time,

the corrosion rate of the MAO-coated samples increases during the first 14 days, and then decreases in the subsequent days. EIS results indicate that the charge transfer resistance is consistent with the corrosion rates.

Together with the Tafel, EIS, post-test surface analysis results, it can be concluded that MAO control parameters of 3000 Hz (pulse frequency), 325V (applied voltage), 30g/L (electrolyte concentration) for 5 min (oxidation time) produce the optimum coating with best corrosion resistance and lowest residual stress. These results show the prospect for optimization of the process variables, surface properties and biocompatibility.

The proposed equations correlates well the experimental data of residual stress and the corrosion current density within the bounds of the data collected. Validation of the results beyond the bounds of the data is still needed. A principal components analysis of the control parameters shows that pulse frequency has the dominant role on the residual stress and the corrosion rate.

The proposed animation model accurately presents the corrosion processes and the corrosion mechanism of the MAO-coated AZ31 Mg alloys in the SBF. The original MAO coating and the formation of corrosion product layer on the sample after long-term immersion effectively inhibited the SBF from penetrating the substrate.

6.2 Future Work

Future work is needed to expand the scope of the current research. The following are few suggestions for future research:

6.2.1 Biodegradable and Biocompatible Coating

During corrosion, the Mg alloys continue to degrade and eventually, the alloy is completely dissolved. The insoluble coating constituents ($MgAl_2O_4$ and $Mg_3(PO_4)_2$) and the corrosion precipitates (brucite, quintinite and hydroxyapatite) are, however, of significant concern since these byproducts are not biodegradable. As the AZ31 Mg alloy corrodes away, the MAO coating layer and the precipitation layer will lose the support of the substrate and will further detach from the substrate. The detached fragments will remain, unless removed otherwise in the human body. The hydroxyapatite, one of the products of corrosion, however, behaves differently because the hydroxyapatite bonds to the living bone. The detached MAO coating layer and the precipitate layer may lead to several undesirable side effects. Therefore, a biodegradable coating with biocompatibility is needed for developing any Mg alloy for biomedical applications. If hydroxyapatite is the only byproduct, then the alloy would be more biocompatible. An approach to this challenge is in the development of a metal matrix composite that is made of magnesium alloy with hydroxyapatite particles as reinforcements. Further research is warranted in this area including the development of a suitable coating which would dissolve in the human body without any significant side effects.

6.2.2 Stress Corrosion Cracking

Another important consideration for the MAO coated samples for biomedial implants

is the behavior of the material under tension or compression. In real application, the MAO AZ31 implant is in actuality under a level of stress. The compressive residual stress is induced during the MAO process. A larger (compressive) stress is detrimental to the corrosion rate. The corrosion behavior of the MAO coated samples in SBF under a varying external stresses has not been studied. The externally induced stress is different from the intrinsic stress that arises in the fabrication process.

An implant employed in the human body must have sufficient strength to sustain and transmit the repeated loading actions resulting from joints and muscular forces. The mechanical stress along with the corrosive physiological environment poses further complications, such as stress corrosion cracking (SCC). SCC is considered to be one of the most dangerous forms of corrosion-assisted failures. SCC may be of particular concern for devices such as pins and screws that are used for securing orthopaedic implants. SCC may cause an unexpected or sudden catastrophic failure. Such sudden failures caused by the SCC of an implant may have serious consequences, such as removal of the failed device, and painful irritation or inflammation of surrounding tissues. Magnesium alloys are susceptible to SCC in chloride environment [114-116]. However, there are only few studies on SCC of magnesium alloys in physiological environment [117, 118]. Therefore, further research on SCC of AZ31 alloy in SBF is needed.

6.2.3 Longer immersion time

In order to verify the corrosion process and the corrosion mechanism proposed in this research, longer immersion time is needed in the future work.

Literature Cited

[1] M.P. Staiger, Pietak, A.M., Huadmai, J., Dias, G., Magnesium and its alloys as orthopedic biomaterials: A review, Biomaterials, 27 (2006) 1728-1734.

[2] Y. Xin, T. Hu, P.K. Chu, In vitro studies of biomedical magnesium alloys in a simulated physiological environment: A review, Acta Biomater., 7 (2011) 1452-1459.

[3] D.A. Puleo, W.W. Huh, ACUTE TOXICITY OF METAL-IONS IN CULTURES OF OSTEOGENIC CELLS DERIVED FROM BONE-MARROW STROMAL CELLS, Journal of Applied Biomaterials, 6 (1995) 109-116.

[4] J.J. Jacobs, J.L. Gilbert, R.M. Urban, Corrosion of metal orthopaedic implants, Journal of Bone and Joint Surgery-American Volume, 80A (1998) 268-282.

[5] C. Lhotka, T. Szekeres, I. Steffan, K. Zhuber, K. Zweymuller, Four-year study of cobalt and chromium blood levels in patients managed with two different metal-on-metal total hip replacements, Journal of Orthopaedic Research, 21 (2003) 189-195.

[6] J.J. Jacobs, A.K. Skipor, L.M. Patteson, N.J. Hallab, W.G. Paprosky, J. Black, J.O. Galante, Metal release in patients who have has a primary total hip arthroplasty - A prospective, controlled, longitudinal study, Journal of Bone and Joint Surgery-American Volume, 80A (1998) 1447-1458.

[7] J.J. Jacobs, N.J. Hallab, A.K. Skipor, R.M. Urban, Metal degradation products - A cause for concern in metal-metal bearings?, Clinical Orthopaedics and Related Research, (2003) 139-147.

[8] D. Granchi, G. Ciapetti, S. Stea, L. Savarino, F. Filippini, A. Sudanese, G. Zinghi, L. Montanaro, Cytokine release in mononuclear cells of patients with Co-Cr hip prosthesis, Biomaterials, 20 (1999) 1079-1086.

[9] Y. Niki, H. Matsumoto, Y. Suda, T. Otani, K. Fujikawa, Y. Toyama, N. Hisamori, A. Nozue, Metal ions induce bone-resorbing cytokine production through the redox pathway in synoviocytes and bone marrow macrophages, Biomaterials, 24 (2003) 1447-1457.

[10] D.R. Haynes, S.J. Boyle, S.D. Rogers, D.W. Howie, B. Vernon-Roberts, Variation in cytokines induced by particles from different prosthetic materials, Clinical Orthopaedics and Related Research, (1998) 223-230.

[11] J.Y. Wang, B.H. Wicklund, R.B. Gustilo, D.T. Tsukayama, Titanium, chromium and cobalt ions modulate the release of bone-associated cytokines by human monocytes/macrophages in vitro, Biomaterials, 17 (1996) 2233-2240.

[12] Y.M. Bi, R.R. Van de Motter, A.A. Ragab, V.M. Goldberg, J.M. Anderson, E.M. Greenfield, Titanium particles stimulate bone resorption by inducing differentiation of murine osteoclasts, Journal of Bone and Joint Surgery-American Volume, 83A (2001) 501-508.

[13] M.J. Allen, B.J. Myer, P.J. Millett, N. Rushton, The effects of particulate cobalt, chromium and cobalt-chromium alloy on human osteoblast-like cells in vitro, Journal of Bone and Joint Surgery-British Volume, 79B (1997) 475-482.

[14] M.L. Wang, L.J. Nesti, R. Tuli, J. Lazatin, K.G. Danielson, P.F. Sharkey, R.S. Tuan, Titanium particles suppress expression of osteoblastic phenotype in human mesenchymal stem cells, Journal of Orthopaedic Research, 20 (2002) 1175-1184.

[15] J. Nagels, M. Stokdijk, P.M. Rozing, Stress shielding and bone resorption in shoulder arthroplasty, Journal of Shoulder and Elbow Surgery, 12 (2003) 35-39.

[16] K.Y. Park JB, Metallic biomaterials., 2003.

[17] T. Okuma, Magnesium and bone strength, Nutrition, 17 679-680.

[18] S. NEL., Magnesium: an update on physiological, clinical and analytical aspects., Clinica Chimica Acta 2000, 294 1-26.

[19] Water, electrolyte mineral and acid/base metabolism. Section 2. Endocrine & Metabolic Disorders. Merk Manual of Diagnosis and Therapy [Chapter 12].

[20] J. Vormann, Magnesium: nutrition and metabolism, Mol. Aspects. Med., 24 (2003) 27-37.

[21] F.I. Wolf, A. Cittadini, Chemistry and biochemistry of magnesium, Mol. Aspects. Med., 24 (2003) 3-9.

[22] A. Hartwig, Role of magnesium in genomic stability, Mutation Research/Fundamental and Molecular Mechanisms of Mutagenesis, 475 (2001) 113-121.

[23] R.F. Zhang, G.Y. Xiong, C.Y. Hu, Comparison of coating properties obtained by MAO on magnesium alloys in silicate and phytic acid electrolytes, Curr. Appl Phys., 10 (2010) 255-259.

[24] S. Shrestha, Magnesium and surface engineering, Surf. Eng., 26 (2010) 313-316.

[25] Y. Dai, Q. Li, H. Gao, L.Q. Li, F.N. Chen, F. Luo, S.Y. Zhang, Effects of five additives on electrochemical corrosion behaviours of AZ91D magnesium alloy in sodium chloride solution, Surf. Eng., 27 (2011) 536-543.

[26] Z.X. Li, M. Kawashita, Current progress in inorganic artificial biomaterials, J. Artif. Organs, 14 (2011) 163-170.

[27] F. Witte, N. Hort, C. Vogt, S. Cohen, K.U. Kainer, R. Willumeit, F. Feyerabend, Degradable biomaterials based on magnesium corrosion, Current Opinion in Solid State and Materials Science, 12 63-72.

[28] Z. Wen, C. Wu, C. Dai, F. Yang, Corrosion behaviors of Mg and its alloys with

different Al contents in a modified simulated body fluid, J. Alloys Compd., 488 (2009) 392-399.

[29] S.X. Zhang, X.N. Zhang, C.L. Zhao, J.A. Li, Y. Song, C.Y. Xie, H.R. Tao, Y. Zhang, Y.H. He, Y. Jiang, Y.J. Bian, Research on an Mg-Zn alloy as a degradable biomaterial, Acta Biomater., 6 (2010) 626-640.

[30] N.T. Kirkland, J. Lespagnol, N. Birbilis, M.P. Staiger, A survey of bio-corrosion rates of magnesium alloys, Corros. Sci., 52 (2010) 287-291.

[31] W.-D. Mueller, M. Lucia Nascimento, M.F. Lorenzo de Mele, Critical discussion of the results from different corrosion studies of Mg and Mg alloys for biomaterial applications, Acta Biomater., 6 (2010) 1749-1755.

[32] G. Song, Control of biodegradation of biocompatable magnesium alloys, Corros. Sci., 49 (2007) 1696-1701.

[33] W.C. Kim, J.G. Kim, J.Y. Lee, H.K. Seok, Influence of Ca on the corrosion properties of magnesium for biomaterials, Mater. Lett., 62 (2008) 4146-4148.

[34] Y. Wan, G. Xiong, H. Luo, F. He, Y. Huang, X. Zhou, Preparation and characterization of a new biomedical magnesium–calcium alloy, Materials & Design, 29 (2008) 2034-2037.

[35] H.X. Wang, S.K. Guan, X. Wang, C.X. Ren, L.G. Wang, In vitro degradation and mechanical integrity of Mg-Zn-Ca alloy coated with Ca-deficient hydroxyapatite by the pulse electrodeposition process, Acta Biomater., 6 (2010) 1743-1748.

[36] E.L. Zhang, L. Yang, Microstructure, mechanical properties and bio-corrosion properties of Mg-Zn-Mn-Ca alloy for biomedical application, Materials Science and Engineering a-Structural Materials Properties Microstructure and Processing, 497 (2008) 111-118.

[37] L.P. Xu, E.L. Zhang, D.S. Yin, S.Y. Zeng, K. Yang, In vitro corrosion behaviour of Mg alloys in a phosphate buffered solution for bone implant application, Journal of Materials Science-Materials in Medicine, 19 (2008) 1017-1025.

[38] L. Yang, E. Zhang, Biocorrosion behavior of magnesium alloy in different simulated fluids for biomedical application, Mater. Sci. Eng., C, 29 (2009) 1691-1696.

[39] F. Witte, V. Kaese, H. Haferkamp, E. Switzer, A. Meyer-Lindenberg, C.J. Wirth, H. Windhagen, In vivo corrosion of four magnesium alloys and the associated bone response, Biomaterials, 26 (2005) 3557-3563.

[40] N. Hort, Y. Huang, D. Fechner, M. Stormer, C. Blawert, F. Witte, C. Vogt, H. Drucker, R. Willumeit, K.U. Kainer, F. Feyerabend, Magnesium alloys as implant materials - Principles of property design for Mg-RE alloys, Acta Biomater., 6 (2010) 1714-1725.

[41] A.C. Hanzi, I. Gerber, M. Schinhammer, J.F. Loffler, P.J. Uggowitzer, On the in vitro and in vivo degradation performance and biological response of new biodegradable Mg-Y-Zn alloys, Acta Biomater., 6 (2010) 1824-1833.

[42] Q.M. Peng, Y.D. Huang, L. Zhou, N. Hort, K.U. Kainer, Preparation and properties of high purity Mg-Y biomaterials, Biomaterials, 31 (2010) 398-403.

[43] L. Li, J. Gao, Y. Wang, Evaluation of cyto-toxicity and corrosion behavior of alkali-heat-treated magnesium in simulated body fluid, Surf. Coat. Technol., 185 (2004) 92-98.

[44] M.A. Gonzalez-Nunez, C.A. Nunez-Lopez, P. Skeldon, G.E. Thompson, H. Karimzadeh, P. Lyon, T.E. Wilks, A non-chromate conversion coating for magnesium alloys and magnesium-based metal matrix composites, Corros. Sci., 37 (1995) 1763-1772.

[45] Y. Mizutani, S.J. Kim, R. Ichino, M. Okido, Anodizing of Mg alloys in alkaline solutions, Surf. Coat. Technol., 169-170 (2003) 143-146.

[46] H.M. Wong, K.W.K. Yeung, K.O. Lam, V. Tam, P.K. Chu, K.D.K. Luk, K.M.C. Cheung, A biodegradable polymer-based coating to control the performance of magnesium alloy orthopaedic implants, Biomaterials, 31 (2010) 2084-2096.

[47] T.M. Yue, A.H. Wang, H.C. Man, Improvement in the corrosion resistance of magnesium composite by excimer laser surface treatment, Scripta Materialia, 38 (1997) 191-198.

[48] H. Hoche, H. Scheerer, D. Probst, E. Broszeit, C. Berger, Plasma anodisation as an environmental harmless method for the corrosion protection of magnesium alloys, Surf. Coat. Technol., 174-175 1002-1007.

[49] H. Altun, S. Sen, The effect of DC magnetron sputtering AlN coatings on the corrosion behaviour of magnesium alloys, Surf. Coat. Technol., 197 (2005) 193-200.

[50] Y.K. Lee, K. Lee, T. Jung, Study on microarc oxidation of AZ31B magnesium alloy in alkaline metal silicate solution, Electrochem. Commun., 10 (2008) 1716-1719.

[51] A.L. Yerokhin, X. Nie, A. Leyland, A. Matthews, S.J. Dowey, Plasma electrolysis for surface engineering, Surf. Coat. Technol., 122 (1999) 73-93.

[52] Y.M. Wang, D.C. Jia, L.X. Guo, T.Q. Lei, B.L. Jiang, Effect of discharge pulsating on microarc oxidation coatings formed on Ti6Al4V alloy, Mater. Chem. Phys., 90 (2005) 128-133.

[53] G. Sundararajan, L. Rama Krishna, Mechanisms underlying the formation of thick alumina coatings through the MAO coating technology, Surf. Coat. Technol., 167 (2003) 269-277.

[54] W. Xue, Z. Deng, R. Chen, T. Zhang, Growth regularity of ceramic coatings

formed by microarc oxidation on Al-Cu-Mg alloy, Thin Solid Films, 372 (2000) 114-117.

[55] E. Atar, Sarioglu, C., Demirler, U., Sabri Kayali, E., Cimenoglu, H., Residual stress estimation of ceramic thin films by X-ray diffraction and indentation techniques, Scripta Materialia, 48 (2003) 1331-1336.

[56] A. Oyane, H.M. Kim, T. Furuya, T. Kokubo, T. Miyazaki, T. Nakamura, Preparation and assessment of revised simulated body fluids, Journal of Biomedical Materials Research Part A, 65A (2003) 188-195.

[57] Y. Wang, M. Wei, J. Gao, J. Hu, Y. Zhang, Corrosion process of pure magnesium in simulated body fluid, Mater. Lett., 62 (2008) 2181-2184.

[58] Y. Song, D. Shan, R. Chen, F. Zhang, E.-H. Han, Biodegradable behaviors of AZ31 magnesium alloy in simulated body fluid, Mater. Sci. Eng., C, 29 (2009) 1039-1045.

[59] T. Kokubo, H. Takadama, How useful is SBF in predicting in vivo bone bioactivity?, Biomaterials, 27 (2006) 2907-2915.

[60] M. Lihe, W. Yulin, W. Yizao, H. Fang, H. Yuan, Corrosion Resistance of Ag-ion Implanted Mg-Ca-Zn Alloys in SBF, Rare Metal Materials and Engineering, 39 (2010) 2075-2078.

[61] A.M. Fekry, R.M. El-Sherif, Electrochemical corrosion behavior of magnesium and titanium alloys in simulated body fluid, Electrochim. Acta, 54 (2009) 7280-7285.

[62] M.B. Kannan, R.K.S. Raman, In vitro degradation and mechanical integrity of calcium-containing magnesium alloys in modified-simulated body fluid, Biomaterials, 29 (2008) 2306-2314.

[63] J. Hu, C. Wang, W.C. Ren, S. Zhang, F. Liu, Microstructure evolution and corrosion mechanism of dicalcium phosphate dihydrate coating on magnesium alloy in simulated body fluid, Mater. Chem. Phys., 119 (2010) 294-298.

[64] X.N. Gu, Y.F. Zheng, L.J. Chen, Influence of artificial biological fluid composition on the biocorrosion of potential orthopedic Mg-Ca, AZ31, AZ91 alloys, Biomedical Materials, 4 (2009).

[65] N. Hara, Y. Kobayashi, D. Kagaya, N. Akao, Formation and breakdown of surface films on magnesium and its alloys in aqueous solutions, Corros. Sci., 49 (2007) 166-175.

[66] L. Zhao, C. Cui, Q. Wang, S. Bu, Growth characteristics and corrosion resistance of micro-arc oxidation coating on pure magnesium for biomedical applications, Corros. Sci., 52 (2010) 2228-2234.

[67] J. Chen, R.-c. Zeng, W.-j. Huang, Z.-q. Zheng, Z.-l. Wang, J. Wang,

Characterization and wear resistance of macro-arc oxidation coating on magnesium alloy AZ91 in simulated body fluids, Transactions of Nonferrous Metals Society of China, 18 (2008) s361-s364.

[68] Y.M. Wang, F.H. Wang, M.J. Xu, B. Zhao, L.X. Guo, J.H. Ouyang, Microstructure and corrosion behavior of coated AZ91 alloy by microarc oxidation for biomedical application, Appl. Surf. Sci., 255 (2009) 9124-9131.

[69] H. Duan, K. Du, C. Yan, F. Wang, Electrochemical corrosion behavior of composite coatings of sealed MAO film on magnesium alloy AZ91D, Electrochim. Acta, 51 (2006) 2898-2908.

[70] Q. Cai, L. Wang, B. Wei, Q. Liu, Electrochemical performance of microarc oxidation films formed on AZ91D magnesium alloy in silicate and phosphate electrolytes, Surf. Coat. Technol., 200 (2006) 3727-3733.

[71] J. Liang, P.B. Srinivasan, C. Blawert, M. Störmer, W. Dietzel, Electrochemical corrosion behaviour of plasma electrolytic oxidation coatings on AM50 magnesium alloy formed in silicate and phosphate based electrolytes, Electrochim. Acta, 54 (2009) 3842-3850.

[72] H.M. Wang, Z.H. Chen, L.L. Li, Corrosion resistance and microstructure characteristics of plasma electrolytic oxidation coatings formed on AZ31 magnesium alloy, Surf. Eng., 26 (2010) 385-391.

[73] P.B. Srinivasan, N. Scharnagl, C. Blawert, W. Dietzel, Enhanced corrosion protection of AZ31 magnesium alloy by duplex plasma electrolytic oxidation and polymer coatings, Surf. Eng., 26 (2010) 354-360.

[74] C. Blawert, V. Heitmann, W. Dietzel, H.M. Nykyforchyn, M.D. Klapkiv, Influence of electrolyte on corrosion properties of plasma electrolytic conversion coated magnesium alloys, Surf. Coat. Technol., 201 (2007) 8709-8714.

[75] Y.G. Ko, S. Namgung, D.H. Shin, Correlation between KOH concentration and surface properties of AZ91 magnesium alloy coated by plasma electrolytic oxidation, Surf. Coat. Technol., 205 (2010) 2525-2531.

[76] G.G. Stoney, The Tension of Metallic Films Deposited by Electrolysis, Proceedings of the Royal Society of London. Series A, Containing Papers of a Mathematical and Physical Character, 82 (1909) 172-175.

[77] P. Bala Srinivasan, J. Liang, R.G. Balajeee, C. Blawert, M. Störmer, W. Dietzel, Effect of pulse frequency on the microstructure, phase composition and corrosion performance of a phosphate-based plasma electrolytic oxidation coated AM50 magnesium alloy, Appl. Surf. Sci., 256 (2010) 3928-3935.

[78] G.-H. Lv, H. Chen, W.-C. Gu, L. Li, E.-W. Niu, X.-H. Zhang, S.-Z. Yang, Effects of current frequency on the structural characteristics and corrosion property of ceramic coatings formed on magnesium alloy by PEO technology, J. Mater. Process.

Technol., 208 (2008) 9-13.

[79] S. Nakahara, Microporosity in thin films, Thin Solid Films, 64 (1979) 149-161.

[80] S.H. Ahn, J.H. Lee, H.G. Kim, J.G. Kim, A study on the quantitative determination of through-coating porosity in PVD-grown coatings, Appl. Surf. Sci., 233 (2004) 105-114.

[81] M. Laleh, A.S. Rouhaghdam, T. Shahrabi, A. Shanghi, Effect of alumina sol addition to micro-arc oxidation electrolyte on the properties of MAO coatings formed on magnesium alloy AZ91D, J. Alloys Compd., 496 (2010) 548-552.

[82] C. Liu, Q. Bi, A. Leyland, A. Matthews, An electrochemical impedance spectroscopy study of the corrosion behaviour of PVD coated steels in 0.5 N NaCl aqueous solution: Part II.: EIS interpretation of corrosion behaviour, Corros. Sci., 45 (2003) 1257-1273.

[83] D.A. Jones, Principles and Prevention of Corrosion, in, Prentic Hall, Upper Saddle River, 1996, pp. 572.

[84] J. Cai, F. Cao, L. Chang, J. Zheng, J. Zhang, C. Cao, The preparation and corrosion behaviors of MAO coating on AZ91D with rare earth conversion precursor film, Appl. Surf. Sci., 257 (2011) 3804-3811.

[85] K.L. Rama, Somaraju, K. R. C., Sundararajan, G., The tribological performance of ultra-hard ceramic composite coatings obtained through microarc oxidation, Surf. Coat. Technol., 163-164 (2003) 484-490.

[86] A.R. Boccaccini, Z. Fan, A new approach for the Young's modulus-porosity correlation of ceramic materials, Ceram. Int., 23 (1997) 239-245.

[87] I. Yagi, K. Tsukagoshi, Y. Aoyagi, Growth control of pentacene films on SiO2/Si substrates towards formation of flat conduction layers, Thin Solid Films, 467 (2004) 168-171.

[88] M. Laleh, F. Kargar, A.S. Rouhaghdam, Formation of a compact oxide layer on AZ91D magnesium alloy by microarc oxidation via addition of cerium chloride into the MAO electrolyte, J. Coat. Technol. Res., 8 (2011) 765-771.

[89] L. Guo-Hua, G. Wei-Chao, C. Huan, L. Li, N. Er-Wu, Y. Si-Ze, Microstructure and Corrosion Performance of Oxide Coatings on Aluminium by Plasma Electrolytic Oxidation in Silicate and Phosphate Electrolytes, Chinese Physics Letters, 23 (2006) 3331.

[90] K. Ling-Bin, L. Mei, L. Meng-Ke, G. Xin-Yong, L. Hu-Lin, Morphology of Platinum Nanowire Array Electrodeposited Within Anodic Aluminium Oxide Template Characterized by Atomic Force Microscopy, Chinese Physics Letters, 20 (2003) 763.

[91] J.W. Hutchinson, Z. Suo, Mixed Mode Cracking in Layered Materials, in: W.H. John, Y.W. Theodore (Eds.) Advances in Applied Mechanics, Elsevier, 1991, pp. 63-191.

[92] A.G. Evans, J.W. Hutchinson, The thermomechanical integrity of thin films and multilayers, Acta Metallurgica et Materialia, 43 (1995) 2507-2530.

[93] W. Han-Hua, J. Zeng-Sun, L. Bei-Yu, Y. Feng-Rong, L. Xian-Yi, Characterization of Microarc Oxidation Process on Aluminium Alloy, Chinese Physics Letters, 20 (2003) 1815.

[94] B.V. I, T.O. P, M.G. A, Protection of Metal, (1998).

[95] O. Terleeva, V. Belevantsev, A. Slonova, D. Boguta, V. Rudnev, Comparison analysis of formation and some characteristics of microplasma coatings on aluminum and titanium alloys, Protection of Metals, 42 (2006) 272-278.

[96] F. Witte, F. Feyerabend, P. Maier, J. Fischer, M. Störmer, C. Blawert, W. Dietzel, N. Hort, Biodegradable magnesium-hydroxyapatite metal matrix composites, Biomaterials, 28 (2007) 2163-2174.

[97] X. Zheng, J. Li, Y. Zhou, X-ray diffraction measurement of residual stress in PZT thin films prepared by pulsed laser deposition, Acta Mater., 52 (2004) 3313-3322.

[98] Y.C. Zhou, Yang, Z.Y., Zheng, X.J., Residual stress in PZT thin films prepared by pulsed laser deposition, Surf. Coat. Technol., 162 (2003) 202-211.

[99] P.S. Prevéy, X-ray Diffraction Residual Stress Techniques, in: Lambda Research, 5521 Fair Lane, Cincinnati, OH Metals Handbook. 10. Metals Park: American Society for Metals, 1986, pp. 380-392.

[100] R.H.U. Khan, A. Yerokhin, X. Li, H. Dong, A. Matthews, Surface characterisation of DC plasma electrolytic oxidation treated 6082 aluminium alloy: Effect of current density and electrolyte concentration, Surf. Coat. Technol., 205 (2010) 1679-1688.

[101] H. Heinrich, J.B. Mullin, II-VI and I-VII Compounds; Semimagnetic Compounds, in, Springer, 1999.

[102] B. Lonyuk, I. Apachitei, J. Duszczyk, The effect of oxide coatings on fatigue properties of 7475-T6 aluminium alloy, Surf. Coat. Technol., 201 (2007) 8688-8694.

[103] R.H.U. Khan, Yerokhin, A. L., Pilkington, T., Leyland, A., Matthews, A., Residual stresses in plasma electrolytic oxidation coatings on Al alloy produced by pulsed unipolar current, Surface and Coatings Technology, 200 (2005) 1580-1586.

[104] M. Bohner, J. Lemaitre, Can bioactivity be tested in vitro with SBF solution?, Biomaterials, 30 (2009) 2175-2179.

[105] H.K. T. Kokubo, S. Sakka, T. Kitsugi, T. Yamamuro, J. Biomed., Solutions able to reproduce in vivo surface-structure changes in bioactive glass-ceramic A-W, J. Biomed. Mater. Res., 24 (1990) 721-734.

[106] A. Ghasemi, V.S. Raja, C. Blawert, W. Dietzel, K.U. Kainer, Study of the structure and corrosion behavior of PEO coatings on AM50 magnesium alloy by electrochemical impedance spectroscopy, Surf. Coat. Technol., 202 (2008) 3513-3518.

[107] Y.H. Gu, C.-f. Chen, S. Bandopadhyay, C.Y. Ning, Y.J. Zhang, Y.J. Guo, Corrosion mechanism and model of pulsed DC microarc oxidation treated AZ31 alloy in simulated body fluid, Appl. Surf. Sci., 10.1016/j.apsusc.2012.03.016 (2012).

[108] L. Wen, Y.M. Wang, Y. Liu, Y. Zhou, L.X. Guo, J.H. Ouyang, D.C. Jia, EIS study of a self-repairing microarc oxidation coating, Corros. Sci., 53 (2011) 618-623.

[109] H. Zhang, B.W. Darvell, Morphology and structural characteristics of hydroxyapatite whiskers: Effect of the initial Ca concentration, Ca/P ratio and pH, Acta Biomater., 7 (2011) 2960-2968.

[110] M.T. Carayon, J.L. Lacout, Study of the Ca/P atomic ratio of the amorphous phase in plasma-sprayed hydroxyapatite coatings, Journal of Solid State Chemistry, 172 (2003) 339-350.

[111] P. Das, O. Akkus, A.-M. Azad, Optimization of the mineral content in polymeric gels: The effect of calcium to phosphate molar ratio, Journal of Crystal Growth, 280 (2005) 587-593.

[112] O. Khaselev, Weiss, D., Yahalom, J., Structure and composition of anodic films formed on binary Mg-Al alloys in KOH-aluminate solutions under continuous sparking, Corros. Sci., 43 (2001) 1295-1307.

[113] W. Suchanek, M. Yoshimura, Processing and properties of hydroxyapatite-based biomaterials for use as hard tissue replacement implants, Journal of Materials Research, 13 (1998) 94-117.

[114] M.B. Kannan, V.S. Raja, Enhancing stress corrosion cracking resistance in Al-Zn-Mg-Cu-Zr alloy through inhibiting recrystallization, Engineering Fracture Mechanics, 77 (2010) 249-256.

[115] Y. Uematsu, T. Kakiuchi, M. Nakajima, Stress corrosion cracking behavior of the wrought magnesium alloy AZ31 under controlled cathodic potentials, Mater. Sci. Eng., A, 531 (2012) 171-177.

[116] Y. Uematsu, T. Kakiuchi, M. Nakajima, Hydrogen Embrittlement Type Stress Corrosion Cracking Behavior of Wrought Magnesium Alloy AZ31, Procedia Engineering, 10 (2011) 578-582.

[117] M.B. Kannan, R.K.S. Raman, Evaluating the stress corrosion cracking susceptibility of Mg-Al-Zn alloy in modified-simulated body fluid for orthopaedic

implant application, Scripta Materialia, 59 (2008) 175-178.

[118] L. Choudhary, J. Szmerling, R. Goldwasser, R.K.S. Raman, Investigations into stress corrosion cracking behaviour of AZ91D magnesium alloy in physiological environment, Procedia Engineering, 10 (2011) 518-523.

Appendices

Appendix A: Sample as Received

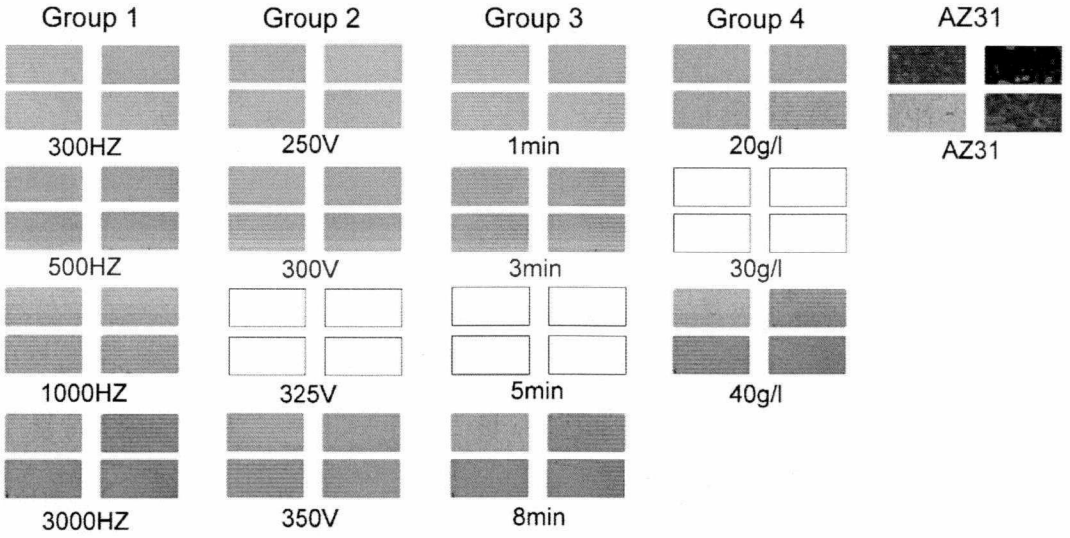

Appendix B: Raw Data for Regression of Residual Stress

x_1 Pulse frequency (Hz)	x_2 Applied voltage (V)	x_3 Oxidation time (sec)	x_4 Electrolyte concentration (g/L)	Y Residual stress (MPa)
300	325	300	30	-1272
500	325	300	30	-1178
1000	325	300	30	-1032
3000	325	300	30	-611
3000	250	300	30	-1254
3000	300	300	30	-728
3000	325	300	30	-611
3000	350	300	30	-789
3000	325	300	20	-1206
3000	325	300	30	-611
3000	325	300	40	-837
3000	325	60	30	-1152
3000	325	180	30	-834
3000	325	300	30	-611
3000	325	480	30	-996

Appendix C: Raw Data for Regression of Corrosion Current Density

x_1 Pulse frequency (Hz)	x_2 Applied voltage (V)	x_3 Oxidation time (sec)	x_4 Electrolyte concentration (g/L)	x_5 Immersion time (h)	Y Corrosion current density ($\mu A/cm^2$)
300	325	300	30	24	4.82
300	325	300	30	48	5.30
300	325	300	30	72	5.92
300	325	300	30	96	6.46
300	325	300	30	120	7.00
300	325	300	30	144	11.02
300	325	300	30	168	15.87
300	325	300	30	336	20.57
300	325	300	30	504	16.05
300	325	300	30	672	13.50
500	325	300	30	24	3.13
500	325	300	30	48	3.45
500	325	300	30	72	3.91
500	325	300	30	96	4.32
500	325	300	30	120	4.97
500	325	300	30	144	7.46
500	325	300	30	168	9.87
500	325	300	30	336	18.19
500	325	300	30	504	13.85
500	325	300	30	672	11.30
1000	325	300	30	24	2.50
1000	325	300	30	48	2.57
1000	325	300	30	72	2.65
1000	325	300	30	96	2.83
1000	325	300	30	120	2.89
1000	325	300	30	144	3.59
1000	325	300	30	168	4.74
1000	325	300	30	336	15.76
1000	325	300	30	504	11.02
1000	325	300	30	672	9.14
3000	325	300	30	24	1.64
3000	325	300	30	48	1.71
3000	325	300	30	72	1.80
3000	325	300	30	96	2.07
3000	325	300	30	120	2.15

3000	325	300	30	144	2.49
3000	325	300	30	168	3.88
3000	325	300	30	336	10.6
3000	325	300	30	504	9.15
3000	325	300	30	672	4.55
3000	250	300	30	24	2.92
3000	250	300	30	48	3.31
3000	250	300	30	72	3.81
3000	250	300	30	96	3.99
3000	250	300	30	120	4.45
3000	250	300	30	144	5.36
3000	250	300	30	168	7.57
3000	250	300	30	336	17.46
3000	250	300	30	504	14.29
3000	250	300	30	672	8.96
3000	300	300	30	24	1.90
3000	300	300	30	48	2.05
3000	300	300	30	72	2.32
3000	300	300	30	96	2.71
3000	300	300	30	120	2.88
3000	300	300	30	144	4.03
3000	300	300	30	168	5.01
3000	300	300	30	336	13.90
3000	300	300	30	504	11.35
3000	300	300	30	672	5.65
3000	350	300	30	24	2.23
3000	350	300	30	48	2.45
3000	350	300	30	72	2.94
3000	350	300	30	96	3.20
3000	350	300	30	120	3.54
3000	350	300	30	144	4.58
3000	350	300	30	168	6.31
3000	350	300	30	336	14.95
3000	350	300	30	504	12.69
3000	350	300	30	672	7.99
3000	325	60	30	24	4.23
3000	325	60	30	48	4.80
3000	325	60	30	72	5.32
3000	325	60	30	96	5.85
3000	325	60	30	120	6.41

3000	325	60	30	144	10.70
3000	325	60	30	168	15.33
3000	325	60	30	336	20.44
3000	325	60	30	504	18.60
3000	325	60	30	672	15.44
3000	325	180	30	24	3.15
3000	325	180	30	48	3.94
3000	325	180	30	72	4.46
3000	325	180	30	96	5.08
3000	325	180	30	120	5.36
3000	325	180	30	144	6.96
3000	325	180	30	168	9.08
3000	325	180	30	336	17.43
3000	325	180	30	504	12.65
3000	325	180	30	672	9.53
3000	325	480	30	24	2.03
3000	325	480	30	48	2.29
3000	325	480	30	72	2.79
3000	325	480	30	96	3.15
3000	325	480	30	120	3.39
3000	325	480	30	144	4.39
3000	325	480	30	168	5.35
3000	325	480	30	336	14.89
3000	325	480	30	504	11.29
3000	325	480	30	672	7.69
3000	325	300	20	24	4.25
3000	325	300	20	48	4.48
3000	325	300	20	72	4.69
3000	325	300	20	96	4.92
3000	325	300	20	120	5.17
3000	325	300	20	144	6.88
3000	325	300	20	168	9.84
3000	325	300	20	336	27.99
3000	325	300	20	504	21.52
3000	325	300	20	672	18.2
3000	325	300	40	24	2.13
3000	325	300	40	48	2.84
3000	325	300	40	72	2.98
3000	325	300	40	96	3.38
3000	325	300	40	120	3.62

3000	325	300	40	144	4.93
3000	325	300	40	168	6.75
3000	325	300	40	336	18.31
3000	325	300	40	504	15.69
3000	325	300	40	672	11.94

Appendix D: Program Code for Predictive Model

D.1 Program Code for Predictive Model of Residual Stress

```
Public Class Form1

    Private Sub TextBox1_TextChanged(ByVal sender As System.Object,
ByVal e As System.EventArgs) Handles TxtResult.TextChanged
        TxtResult.BackColor = Color.White
    End Sub

    Private Sub Button1_Click(ByVal sender As System.Object, ByVal e
As System.EventArgs) Handles Button1.Click
        Dim Num2 As Integer
        Dim Num3 As Integer
        Dim Num4 As Integer
        Dim Num5 As Integer
        Dim Result As Integer

        If Val(TxtVal2.Text) > 3000 Or Val(TxtVal2.Text) < 300 Then
TxtVal2.Text = ""
        If Val(TxtVal3.Text) > 350 Or Val(TxtVal3.Text) < 250 Then
TxtVal3.Text = ""
        If Val(TxtVal4.Text) > 480 Or Val(TxtVal4.Text) < 60 Then
TxtVal4.Text = ""
        If Val(TxtVal5.Text) > 40 Or Val(TxtVal5.Text) < 20 Then
TxtVal5.Text = ""
        Num2 = Val(TxtVal2.Text)
        Num3 = Val(TxtVal3.Text)
        Num4 = Val(TxtVal4.Text)
        Num5 = Val(TxtVal5.Text)

        Result = (0.223713083000059 * Num2) + ((-0.127459298146685) *
Num3 ^ 2 + 81.7467648567764 * Num3) + ((-0.00876794835611272) * Num4
^ 2 + 5.3667913208703 * Num4) + ((-3.93795482708983) * Num5 ^ 2 +
254.727289625187 * Num5) - 19322.2353665573
        TxtResult.Text = CStr(Result)
        If TxtVal2.Text = "" Or TxtVal3.Text = "" Or TxtVal4.Text =
"" Or TxtVal5.Text = "" Then
            TxtResult.Text = ""
            MsgBox("Please enter a valid number!")

        End If
    End Sub

    Private Sub Button2_Click(ByVal sender As System.Object, ByVal e
As System.EventArgs) Handles Button2.Click
        TxtVal2.Text = ""
        TxtVal3.Text = ""
        TxtVal4.Text = ""
```

```
        TxtVal5.Text = ""
        TxtResult.Text = ""
    End Sub

    Private Sub TxtVal2_KeyPress(ByVal sender As Object, ByVal e As
System.Windows.Forms.KeyPressEventArgs) Handles TxtVal2.KeyPress
        If Char.IsDigit(e.KeyChar) Or e.KeyChar = Chr(8) Or e.KeyChar
= "." Then
            If e.KeyChar = "." And InStr(TxtVal2.Text, ".") > 0 Then
                e.Handled = True
            Else
                e.Handled = False
            End If
        Else
            e.Handled = True
        End If
    End Sub

    Private Sub TxtVal2_LostFocus(ByVal sender As Object, ByVal e As
System.EventArgs) Handles TxtVal2.LostFocus
        If TxtVal2.Text <> "" Then
            If Val(TxtVal2.Text) > 3000 Or Val(TxtVal2.Text) < 300
Then MsgBox("Please input a valid number of 300-3000!")
        End If
    End Sub

    Private Sub TxtVal3_KeyPress(ByVal sender As Object, ByVal e As
System.Windows.Forms.KeyPressEventArgs) Handles TxtVal3.KeyPress
        If Char.IsDigit(e.KeyChar) Or e.KeyChar = Chr(8) Or e.KeyChar
= "." Then
            If e.KeyChar = "." And InStr(TxtVal4.Text, ".") > 0 Then
                e.Handled = True
            Else
                e.Handled = False
            End If
        Else
            e.Handled = True
        End If
    End Sub

    Private Sub TxtVal3_LostFocus(ByVal sender As Object, ByVal e As
System.EventArgs) Handles TxtVal3.LostFocus
        If TxtVal3.Text <> "" Then
            If Val(TxtVal3.Text) > 350 Or Val(TxtVal3.Text) < 250
Then MsgBox("Please input a valid number of 250-350!")
        End If
    End Sub

    Private Sub TxtVal4_KeyPress(ByVal sender As Object, ByVal e As
System.Windows.Forms.KeyPressEventArgs) Handles TxtVal4.KeyPress
        If Char.IsDigit(e.KeyChar) Or e.KeyChar = Chr(8) Or e.KeyChar
= "." Then
            If e.KeyChar = "." And InStr(TxtVal4.Text, ".") > 0 Then
                e.Handled = True
            Else
                e.Handled = False
            End If
        Else
```

```
            e.Handled = True
        End If
    End Sub

    Private Sub TxtVal4_LostFocus(ByVal sender As Object, ByVal e As
System.EventArgs) Handles TxtVal4.LostFocus
        If TxtVal4.Text <> "" Then
            If Val(TxtVal4.Text) > 480 Or Val(TxtVal4.Text) < 60 Then
MsgBox("Please input a valid number of 60-480!")
        End If
    End Sub

    Private Sub TxtVal5_KeyPress(ByVal sender As Object, ByVal e As
System.Windows.Forms.KeyPressEventArgs) Handles TxtVal5.KeyPress
        If Char.IsDigit(e.KeyChar) Or e.KeyChar = Chr(8) Or e.KeyChar
= "." Then
            If e.KeyChar = "." And InStr(TxtVal5.Text, ".") > 0 Then
                e.Handled = True
            Else
                e.Handled = False
            End If
        Else
            e.Handled = True
        End If
    End Sub

    Private Sub TxtVal5_LostFocus(ByVal sender As Object, ByVal e As
System.EventArgs) Handles TxtVal5.LostFocus
        If TxtVal5.Text <> "" Then
            If Val(TxtVal5.Text) > 40 Or Val(TxtVal5.Text) < 20 Then
MsgBox("Please input a valid number of 20-40!")
            End If
    End Sub

   Private Sub Button3_Click(ByVal sender As System.Object, ByVal e
As System.EventArgs) Handles Button3.Click
        End
    End Sub
End Class
```

D.2 Program Code for Predictive Model of Corrosion Current Density

```
    Private Sub TextBox10_TextChanged(ByVal sender As System.Object,
ByVal e As System.EventArgs) Handles TxtResult2.TextChanged
        TxtResult.BackColor = Color.White
    End Sub

    Private Sub Button5_Click(ByVal sender As System.Object, ByVal e
As System.EventArgs) Handles Button5.Click
        TxtVal12.Text = ""
        TxtVal13.Text = ""
        TxtVal14.Text = ""
        TxtVal15.Text = ""
        TxtVal16.Text = ""
        TxtResult2.Text = ""
    End Sub
```

```
    Private Sub Button4_Click(ByVal sender As System.Object, ByVal e
As System.EventArgs) Handles Button4.Click
        End
    End Sub

    Private Sub Button6_Click(ByVal sender As System.Object, ByVal e
As System.EventArgs) Handles Button6.Click
        Dim x1 As Integer
        Dim x2 As Integer
        Dim x3 As Integer
        Dim x4 As Integer
        Dim x5 As Integer
        Dim Y As Double

        If Val(TxtVal12.Text) > 3000 Or Val(TxtVal12.Text) < 300 Then
TxtVal12.Text = ""
        If Val(TxtVal13.Text) > 350 Or Val(TxtVal13.Text) < 250 Then
TxtVal13.Text = ""
        If Val(TxtVal14.Text) > 480 Or Val(TxtVal14.Text) < 60 Then
TxtVal14.Text = ""
        If Val(TxtVal15.Text) > 40 Or Val(TxtVal15.Text) < 20 Then
TxtVal15.Text = ""
        If Val(TxtVal16.Text) > 168 Or Val(TxtVal16.Text) < 24 Then
TxtVal16.Text = ""

        x1 = Val(TxtVal12.Text)
        x2 = Val(TxtVal13.Text)
        x3 = Val(TxtVal14.Text)
        x4 = Val(TxtVal15.Text)
        x5 = Val(TxtVal16.Text)
        Dim a, b, c, d, e1, f, g, h, i, j, k, l, m, n As Double
        a = (-0.000000000035191043083 0875)
        b = (0.000000173489593204487)
        c = (-0.00023997806417669)
        d = (0.0000619140972111928)
        e1 = (-0.00383397802602733)
        f = (0.000006094009782 10822)
        g = (-0.000445646075466281)
        h = (0.000365940028407194)
        i = (-0.023562151704438)
        j = (0.000000000014629723322 8531)
        k = (-0.000000207111621261083)
        l = (0.00000852765619785504)
        m = (-0.000743817299583257)
        n = (1.17923366924893)

        Y = 1.8/5/0.00327*(a * x1 ^ 3 + b * x1 ^ 2 + c * x1) + (d *
x2 ^ 2 + e1 * x2) + (f * x3 ^ 2 + g * x3) + (h * x4 ^ 2 + i * x4) +
(j * x5 ^ 4 + k * x5 ^ 3 + l * x5 ^ 2 + m * x5) + n
        TxtResult2.Text = Math.Round(Y, 4)
        If TxtVal12.Text = "" Or TxtVal13.Text = "" Or TxtVal14.Text
= "" Or TxtVal15.Text = "" Or TxtVal16.Text = "" Then
            TxtResult2.Text = ""
            MsgBox("Please enter a valid number!")
        End If
    End Sub
```

```
    Private Sub TxtVal12_KeyPress(ByVal sender As Object, ByVal e As
System.Windows.Forms.KeyPressEventArgs) Handles TxtVal12.KeyPress
        If Char.IsDigit(e.KeyChar) Or e.KeyChar = Chr(8) Or e.KeyChar
= "." Then
            If e.KeyChar = "." And InStr(TxtVal12.Text, ".") > 0 Then
                e.Handled = True
            Else
                e.Handled = False
            End If
        Else
            e.Handled = True
        End If
    End Sub

    Private Sub TxtVal12_LostFocus(ByVal sender As Object, ByVal e As
System.EventArgs) Handles TxtVal12.LostFocus
        If TxtVal12.Text <> "" Then
            If Val(TxtVal12.Text) > 3000 Or Val(TxtVal12.Text) < 300
Then MsgBox("Please input a valid number of 300-3000!")
        End If
    End Sub

    Private Sub TxtVal13_KeyPress(ByVal sender As Object, ByVal e As
System.Windows.Forms.KeyPressEventArgs) Handles TxtVal13.KeyPress
        If Char.IsDigit(e.KeyChar) Or e.KeyChar = Chr(8) Or e.KeyChar
= "." Then
            If e.KeyChar = "." And InStr(TxtVal13.Text, ".") > 0 Then
                e.Handled = True
            Else
                e.Handled = False
            End If
        Else
            e.Handled = True
        End If
    End Sub

    Private Sub TxtVal13_LostFocus(ByVal sender As Object, ByVal e As
System.EventArgs) Handles TxtVal13.LostFocus
        If TxtVal13.Text <> "" Then
            If Val(TxtVal13.Text) > 350 Or Val(TxtVal13.Text) < 250
Then MsgBox("Please input a valid number of 250-350!")
        End If
    End Sub

    Private Sub TxtVal14_KeyPress(ByVal sender As Object, ByVal e As
System.Windows.Forms.KeyPressEventArgs) Handles TxtVal14.KeyPress
        If Char.IsDigit(e.KeyChar) Or e.KeyChar = Chr(8) Or e.KeyChar
= "." Then
            If e.KeyChar = "." And InStr(TxtVal4.Text, ".") > 0 Then
                e.Handled = True
            Else
                e.Handled = False
            End If
        Else
            e.Handled = True
        End If
    End Sub
```

```
    Private Sub TxtVal14_LostFocus(ByVal sender As Object, ByVal e As
System.EventArgs) Handles TxtVal14.LostFocus
        If TxtVal14.Text <> "" Then
            If Val(TxtVal14.Text) > 480 Or Val(TxtVal14.Text) < 60
Then MsgBox("Please input a valid number of 60-480!")
        End If
    End Sub

    Private Sub TxtVal15_KeyPress(ByVal sender As Object, ByVal e As
System.Windows.Forms.KeyPressEventArgs) Handles TxtVal15.KeyPress
        If Char.IsDigit(e.KeyChar) Or e.KeyChar = Chr(8) Or e.KeyChar
= "." Then
            If e.KeyChar = "." And InStr(TxtVal15.Text, ".") > 0 Then
                e.Handled = True
            Else
                e.Handled = False
            End If
        Else
            e.Handled = True
        End If
    End Sub

    Private Sub TxtVal15_LostFocus(ByVal sender As Object, ByVal e As
System.EventArgs) Handles TxtVal15.LostFocus
        If TxtVal15.Text <> "" Then
            If Val(TxtVal15.Text) > 40 Or Val(TxtVal15.Text) < 20
Then MsgBox("Please input a valid number of 20-40!")
        End If
    End Sub

    Private Sub TxtVal16_KeyPress(ByVal sender As Object, ByVal e As
System.Windows.Forms.KeyPressEventArgs) Handles TxtVal16.KeyPress
        If Char.IsDigit(e.KeyChar) Or e.KeyChar = Chr(8) Or e.KeyChar
= "." Then
            If e.KeyChar = "." And InStr(TxtVal16.Text, ".") > 0 Then
                e.Handled = True
            Else
                e.Handled = False
            End If
        Else
            e.Handled = True
        End If
    End Sub

    Private Sub TxtVal16_LostFocus(ByVal sender As Object, ByVal e As
System.EventArgs) Handles TxtVal16.LostFocus
        If TxtVal16.Text <> "" Then
            If Val(TxtVal16.Text) > 168 Or Val(TxtVal16.Text) < 24
Then MsgBox("Please input a valid number of 24-168!")
        End If
    End Sub

    Private Sub Form1_Load(ByVal sender As System.Object, ByVal e As
System.EventArgs) Handles MyBase.Load
        MyBase.MaximizeBox = False
        MyBase.MinimizeBox = False
    End Sub
End Class
```